Segment Model of Seismic Behaviors of Circular CFT Bridge Piers

円型コンクリート充填鋼製橋脚の地震挙動のセグメントモデル

by

Lyu Fei

Supervised by

Prof. Makoto Obata

Department of Architecture, Civil Engineering and Industrial Management engineering, Nagoya Institute of Technology

June, 2019

Table of contents

Abstract

Thin-walled partially concrete-filled tubular steel columns hereinafter referred to as thin-walled PCFT columns have been used as the piers of elevated-girder bridges widely in Japan because of their excellent seismic performance: strength, ductility, and energy dissipation capacity.

In the bridge structures, a loading condition of piers can be idealized as cantilever columns subjected to axial force and lateral load. Therefore, to have a better understanding of seismic performance of CFT piers, a comprehensive review study of experimental behaviors of CFT columns was conducted. A database of experiments for CFT columns subjected to related load condition was built, including a wide range of design parameters, materials, dimensions and cross-section types. Behaviors of CFT columns such as strength, ductility and collapse mode were summarized.

To consider the excellent seismic performance of CFT columns in design, it is essential to provide some analytical methods to assess ultimate behaviors of the thin-walled PCFT columns by considering local buckling of the steel tube under cyclic loadings, the behavior of the confined in-filled concrete with cracks and the interaction between the steel tube and in-filled concrete.

Hence, an evaluation of current analytical models available in the literature of CFT columns was conducted. The existing fiber-based models of CFT columns are not so accurate especially for the performance-based design. Up to the present, the shell-solid

element model analysis has been the only numerical method that can be used to consider these complicated behaviors of the PCFT columns in a direct manner. However, the use of this model requires unrealistically large computational resource and often encounters numerical difficulties to obtain convergent solutions, when applied to large structural systems such as an elevated-girder bridge system with the multiple thin-walled PCFT piers.

The objective of the present research is to propose a practical 3D fiber-based model with the failure segment that is computationally efficient, yet accurate enough to assess the ultimate behavior of the PCFT columns. This model is calibrated by an optimization technique, only referring to the in-plane hysteretic behavior of each single PCFT column calculated by the shell-solid element model analysis. The calibrated model is applicable to the seismic analysis of the large structural systems with the multiple PCFT piers under arbitrary multi-directional seismic accelerations. The accuracy and numerical efficiency of the proposed fiber-based model in the analysis of the PCFT columns were confirmed extensively by the comparison between results of the shell-solid element model analysis and those of tests, such as cyclic loading tests and shake table tests.

Notations

Chapter 2 and Chapter 3

H_0 : Initial yield force of steel tube;

h : Height of the column specimen;

E_s : Young’s modulus of steel;

I_s : Second moments of area of steel section;

δ : Horizontal displacement of column top;

σ_y or f_y : Yield stress of steel;

P : Applied axial force;

A_s : Area of steel section;

Z_s : Section modulus of hollow steel tube;

D : Diameter of circular CFT column;

t : Thickness of steel tube;

ϑ : steel contribution ratio;

N_p : Plastic compressive strength;

R_t : Radius to thickness ratio;

μ : Poison’s ratio of steel;

r : Radius of circular steel columns;

B : Width of rectangular CFT column;

$\bar{\lambda}$: Slenderness ratio parameter;

π : Mathematical constant pi;

r_s : Radius of gyration;

σ_c or f_{cp} : Compressive strength of concrete;

A_c : Area of concrete section;

α : Axial force ratio;

h_c : Height of infilled concrete;

M_{ys} : Yield bending moment;

M_a : Allowable bending moment of composite cross section;

σ_N : Steel stress due to axial force;

Z_g : Section modules of the hollow steel section;

Δ_y : Initial Yield displacement;

T : Natural period;

M : Mass;

L_b : Length of plastic hinge region;

n_j : parameter consider the effect of axial force;

K : Stiffness;

D_a : Length of anchor bolts:

D_e : Length of embedment;

γ_u : Reduction factor due to section size;

f_{cc} : Confined compressive strength of concrete;

ε_{c0} : Initial yield strain of concrete;

f_{rp} : Maximum average lateral pressure on the infilled concrete;

E_c : Young' modulus of concrete;

β_c : Reduction factor of confined strength of concrete;

Y, V, X, W : Parameters to define the stress-strain relation of infilled concrete;

R_1, R_2 : Slenderness dependent reduction factor;

f_{sy} : Local buckling strength of steel tube;

ε_{sy} : Yield strain of steel;

φ : Slenderness parameter of steel tube;

E_{d1}, E_{d2} : Descending modulus of steel after peak point;

ε_{lbf} : Critical strain to consider the local buckling in the steel tube;

- ***Chapter 4 and Chapter 5***

R_t : Radius to thickness parameter;

$\bar{\lambda}$: Slenderness ratio parameter;

D_s : Diameter of steel tube;

t_s : Thickness of steel tube;

r_s : Radius of gyration;

A_s : Cross-sectional area of steel tube;

σ_y : Yield stress of steel;

E_s : Young's modulus of steel;

v_s : Poison's ratio of steel;

h_p : Height of the column;

P : Axial force applied at column top;

L_f : Length of the failure segment;

L_{se} : Length of the single beam element represent the local buckling behavior;

f_t : Tensile stress of steel;

f_c : Compressive stress of steel;

σ_{yt} : Initial yield stress on the tension side;

σ_{yc} : Initial yield stress on the compression side;

χ : Factor to calculate the maximum stress on the compression side;

σ_{pl}^{U} : Maximum stress on the compression side;

ε_{pl}^{U} : Plastic strain at maximum stress;

m : A power index to determine the shape of softening curve;

ξ : A constant to specify the lower bound of the compression stress;

ε_{pl}^{cr} : Plastic strain at lower bound;

ε_{pl}^{max} : Maximum tensile plastic strain;

$\varepsilon_{pl}^{ut}, \varepsilon_{pl}^{uc}$: Plastic strain corresponds to the specified point on the stress-strain relation;

σ^{min} : Minimum value of compressive stress after softening;

ε_{pl}^{x} : Tensile plastic strain corresponds to limiting stress;

r : Constant to define ε_{pl}^{x};

E_{st} : Modulus after yielding;

a', χ : Parameters to define shape the stress-strain curve;

κ : Reduction factor of tensile yield stress;

E'_{el} : Modified elastic modulus

E_{el} : Elastic modulus;

η : Reduction factor of elastic modulus;

E_{c0} : Initial elastic modulus of concrete;

n : A constant in Ramberg and Osgood's model;

K : Parameter to define concrete constitutive relation;

σ_{cm} : Compression stress of concrete;

E_{dc} : Softening stiffness of concrete;

σ_{c} : Stress of concrete;

d_{c} : Damage parameter of concrete;

$\omega_{d}, k_{cl}, \varepsilon_{0}, n'$: Parameters to define damage parameter of concrete;

E_{c} : Young's modulus of concrete;

ε_{cpl} : plastic strain of concrete;

Δ : Tolerance of calibration;

δ_{0} : Initial yield displacement of steel column;

H_{0} : Initial yield horizontal force of steel column;

$E_{s}I_{s}$: Bending rigidity of Steel tube;

Z_{s} : Cross-section modulus;

r_{p} : Radial coordinates;

θ : Angular coordinates;

h_{c} : Height of infilled concrete;

E_{c00} : Compressive strength of concrete obtained by cylinder test;

Chapter 1. Introduction

Concrete-infilled steel tubular columns hereinafter refer to as CFT columns, have been experimentally and theoretically verified to have far superior strength, ductility and energy absorption capacity to those of hollow thin-walled steel columns over the past two decades. In view of their merits, the application prospect of CFT columns in tall buildings have long been recognized and had been applied to many high-rise buildings such as the Taipei 101 tower, the Two Union Square in Seattle, USA, Shimizu High Rise Building in Tokyo (Samarakkody et al. (2017)) and more recently, KK100 in Shenzhen, China, Alipay Headquarters Building in Hangzhou, China. However, the application status of the CFT columns served as bridge piers is relatively non-ubiquitous around the world, that is, much more preferred in Asia and very limited application in the United States (Stephens et al. (2016a)). Compared to the existence of numerous specialized researches in the field of architecture engineering, studies focus on the CFT bridge piers are relatively insufficient. Different from CFT columns used in building structures, CFT bridge piers usually have larger cross-section, lower axial force ratio and partially infilled concrete at the lower part of the column (Kitada 1998). These characteristics make the mechanical performance of CFT bridge piers differ from those of building structures and should be investigated specifically.

- ***Application of CFT columns in bridge structure***

The earliest bridge construction employing CFT piers available in the literature is the Severn Railway bridge in Gloucestershire England (Huxley 1984), constructed in 1872 (Fig. 1-1). However, the purpose of infilling the concrete into hollow steel tube is to prevent the inner surface of steel tube from corrosion. In China, CFT bridge piers are primarily applied in some super high continuous bridges (Ou 2013). In these bridges, piers usually have more than 100-meters height, for example, Labajin bridge (182.6m) and Heishigou bridge (155m) in Sichuan China. These super high piers are consisting of four CFT columns located at each corner of the rectangular pier cross-section and are connected by steel-concrete composite wall (Fig. 1-2). Although this type of CFT provides a solution of high-seismic-resistance bridge piers in the mountain area, as an economical and conveniently constructional alternatives of conventional reinforced concrete and hollow steel tubular piers, more attention should be placed on the application of CFT piers in the urban highways.

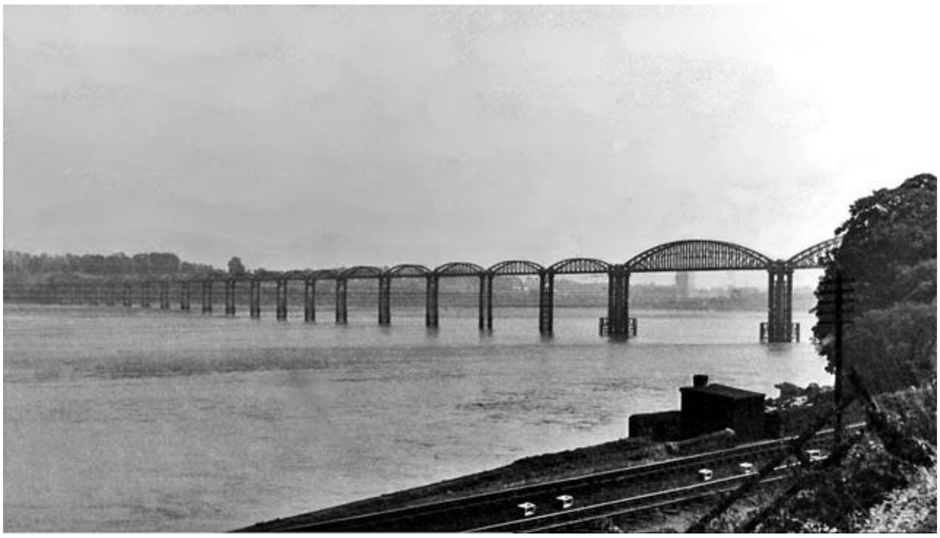

Fig. 1-1. Severn Railway bridge (Wikipedia)

The first urban highway CFT bridge pier in Japan is constructed in 1982 by Hanshin Expressway Public Corporation (HEPC), to ensure the pier stiffness and reduce the girder transverse deflection (Kitada 1998). After that, about thirty CFT bridge piers were constructed, including the access bridges to the Kansai International Airport. Meanwhile, no CFT bridge pier with circular cross-section were constructed before 1995. Since the Hyogoken-Nanbu earthquake, on the 17th of January, 1995, CFT bridge piers are introduced to reconstruct and repair the damaged reinforced concrete and steel piers in Japan. An application of CFT bridge piers in the urban highway is shown in Fig. 1-3.

Fig. 1-2. Heishigou Bridge (Wikipedia)

Fig. 1-3. CFT bridge piers in the urban highway

● *Overview of current studies on the upgraded performance of CFT columns*

The main target of employing CFT columns as a substitute of conventional hollow steel columns is to prevent unbearable damage of the structures during earthquakes. From the past experiences, hollow steel piers and reinforced concrete piers may collapse due to the unpredicted seismic load. Figs. 1-4 show the typical damage forms of steel hollow piers and reinforced RC piers under the past earthquakes.

(a) steel hollow piers (b) reinforced concrete piers

Fig. 1-4. Damage of (a) steel hollow piers and (b) reinforced concrete piers under the earthquake

The related researches on CFT columns are thus focused on their ductility and earthquake resistance. For instance, based on the study of the strength of CFT box columns (Ge and Usami 1992), Ge and Usami (1996) conducted a series of cyclic loading tests to investigate the ductility of CFT box columns applied as bridge piers. In their studies, the energy absorption capacity of a column, effect of additional stiffeners and collapse model of column were investigated. Moreover, to evaluate the seismic performance of CFT box columns, a pseudo dynamic test (Usami et al. (1997)) was conducted. A reduction of residual displacement by infilled-concrete and a significant influence of natural period on the seismic response of the column were observed in the experiment. Nakai and Kitada (1995) conducted a cyclic loading test; Nakanishi et al. (1999) carried out a pseudo dynamic test of CFT columns with box section and obtained similar results with Ge and Usami's. A test of CFT columns with a circular section subjected to bending and torsion (Nakai et al. (1999)) was also conducted and the experimental behavior and theoretical moment resistance of circular CFT column were compared. Marson and Bruneau (2004) conducted a cyclic loading test with four circular column specimens. These specimens were designed based on real bridge piers with fixed base and have relatively larger diameter to thickness ratio. The experiment results revealed that: the ductility of circular CFT columns is sufficient; the energy absorption capacity which reflected in the experimental hysteretic curves is remarkable; no significant bond effect was observed after the completion of experiments. Based on the test, new design equations were proposed (Bruneau and Marson 2004), and, some related researches about the dynamic behaviors of CFT column under blast loading (Fujikura and Bruneau 2012; Fujikura et al. (2008)) were conducted. To ensure the strength of column-to-precast cap beam and column-to-base connection of bridge structures under cyclic loading, Stephens et al. (2016a, 2016b) conducted a cyclic loading test and proposed three types of connections that can sustain large deformation demands. Other experimental studies (Fam et al. (2004); Gajalakshmi and Helena 2012) are focusing on the cyclic loading behaviors of circular columns elsewhere.

The aforementioned experimental studies are conducted under unidirectional loading condition. However, lessons learned from the seismic behaviors of steel bridge piers under the earthquake (Bruneau et al. (1996)) and studies on the bidirectional seismic behavior of steel piers (Goto et al. (2009); Kulkarni et al. (2009); Watanabe et al. (2000)) revealed that multidirectional components of earthquake ground motions may act simultaneously on the bridge pier and have a large influence on their ultimate behaviors. Some studies focusing on the bidirectional seismic behaviors are therefore conducted (Goto et al. (2014, 2017); Yuan et al. (2013, 2014)). Yuan conducted a bidirectional pseudo dynamic tests of rectangular (Yuan et al. (2014)) and circular (Yuan et al. (2013)) CFT bridge piers respectively. The maximum displacement in the bidirectional loading test was much larger than that of unidirectional loading test. CFT piers which can withstand unidirectional loading, can fail to satisfy the safety and reparability demands during bi-directional earthquake. Goto et al. (2014) conducted bidirectional cyclic loading and shake table test of circular CFT columns. The local buckling restraining behaviors caused by the interaction between steel and concrete under uni- and bidirectional loading conditions were clearly explained. Moreover, a comparative study (Goto et al. (2017)) of large-scale shake table tests of continuous elevated girder bridge supported by steel hollow piers and CFT piers was conducted. The CFT supported bridges was examined to have excellent seismic performance under a real earthquake scenario, i.e., small local buckling deformations of the bridge pier and negligibly small residual sway displacement of bridge system.

- ***Research needs***

The efforts of trying to figure out the seismic behaviors and the mechanism behind that have been continuing over the past decades. However, conducting large scale experiment, especially a shake table test is costly and time-consuming. Analytical modeling is therefore important for the full understanding of the performance and mechanism of CFT bridge piers under different loading conditions, as an alternative of experiment studies. According to the experiment review study (Chapter 2), the existing tests of seismic behaviors of CFT bridge piers are still insufficient to cover different design parameters i.e., dimensions, materials in a comprehensive way. Hence, many analytical models of CFT columns were proposed during the past two decades. These models are a concentrated plasticity model, a distributed plasticity model and a Shell-Solid based finite element model. In these models, different constitutive relation of material, element type and modeling method were adopted. However, no research was reported to present a comprehensive review evaluation on their respective advantages, disadvantages and applicability limits. Therefore, to address this knowledge gap and give a reference for researchers who concentrate on the seismic performance of CFT bridge piers to select appropriate modeling method, a review study is presented in Chapter 3.

With demands of performance-based design, precise simulation of dynamic response of members under strong ground motions predicted by scenario earthquakes is necessary. To achieve a balance of efficiency and accuracy, fiber-based model is a prior approach to investigate the structure behaviors, however, the accuracy cannot satisfy the requirements of innovative seismic design concept. To overcome this shortage of current numerical analytical methods, a simple, yet accurate segment model based on beam elements is proposed for the CFT columns. The material parameters of the segment model are identified by the hysteretic load-displacement relation obtained by the in-plane shell-solid FE analysis on single CFT columns. The accuracy of the segment model is further verified by experimental results, such as shake table tests on single CFT columns and elevated-girder bridge models supported by three CFT columns. The use of the segment model dramatically reduces the computing time without sacrificing the accuracy of the solutions.

Chapter 2. Review of experimental study

2.1 CFT column subjected to axial force and lateral cyclic load

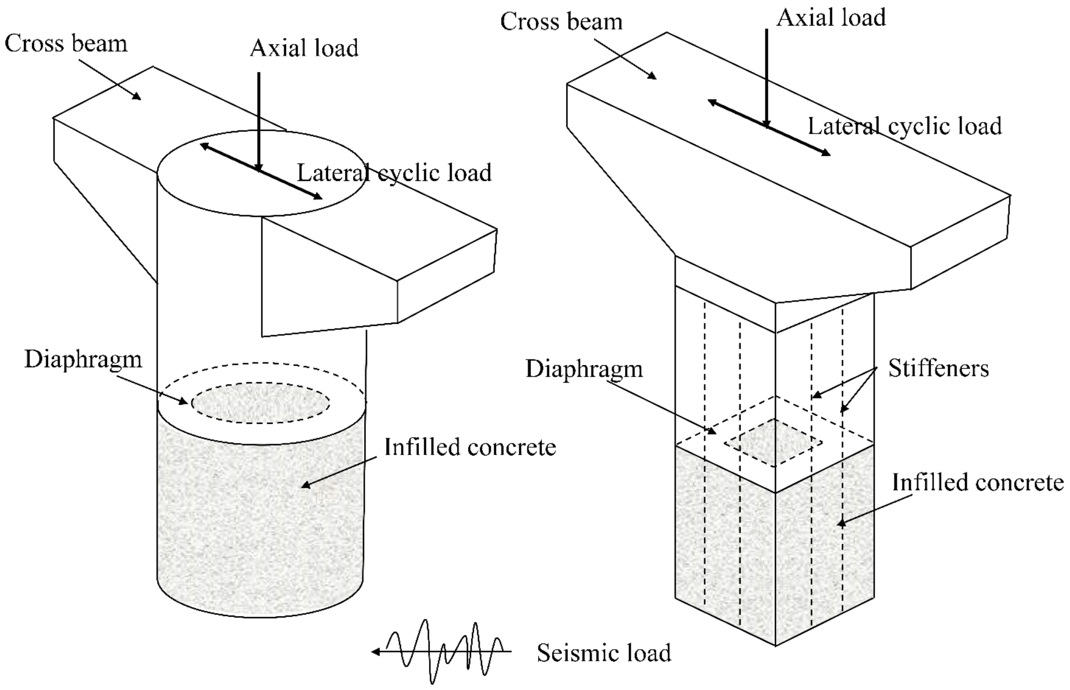

(a) Bridge piers (Goto)

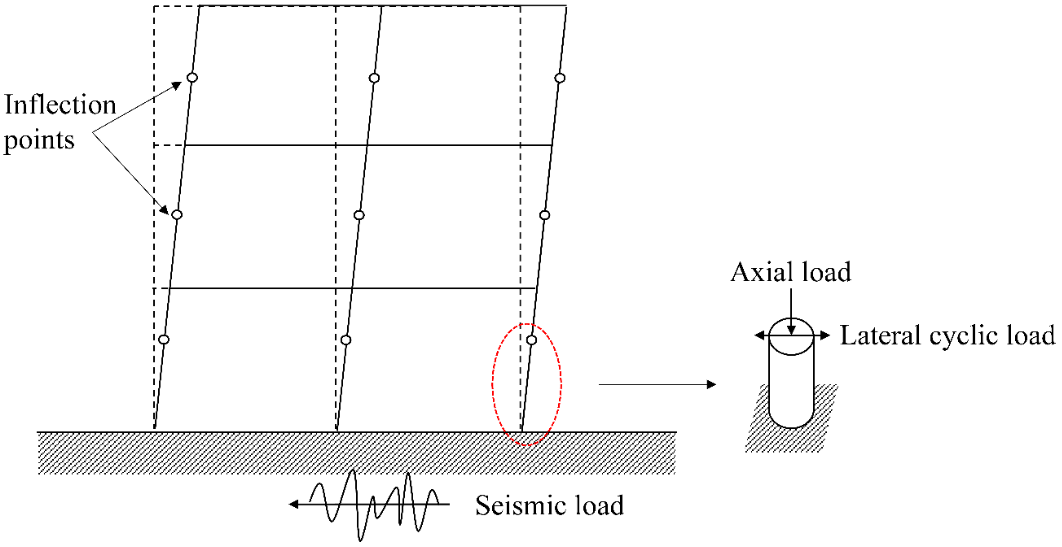

(b) Building columns (Chen et al. (2019))

Fig. 2-1. Applications of CFT columns in structural systems may be subjected to axial force and lateral cyclic load during the earthquake

As shown in Fig. 2-1, structural members such as bridge piers and building columns may be subjected to the combination of axial force and lateral cyclic load during the earthquake. Cyclic loading test on the cantilever CFT columns can be an idealized representation of the behaviors of CFT bridge piers (Fig. 2-1 (a)) and bottom CFT column segment between the inflection point and ground floor of buildings (Fig. 2-1 (b)) under the horizontal seismic load. Carrying out this kind of experimental study is of great use to get a better understanding of the upgraded seismic performance of the CFT columns compared with conventional reinforced concrete and hollow steel columns and to promote the application of CFT structure members. During the past several decades, experimental research on the cyclic behaviors of cantilever CFT columns is one of the most active research areas in structural engineering. A large number of experiments have been conducted with different focus on the design parameters including different section types, dimensions and materials etc. To make full use of existing test results and enhance our knowledge on the performance of CFT columns subjected to horizontal cyclic load, it is necessary to summarize past research results and achievements. Hence, a comprehensive review of experimental researches in this form available in literature was conducted.

2.1.1 Outline of experiments

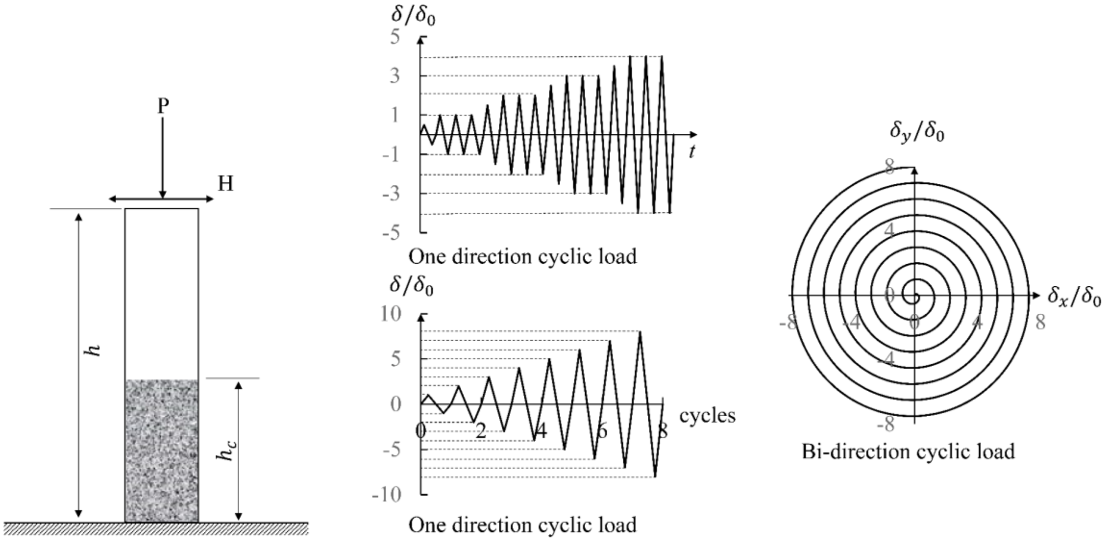

Fig. 2-2. Loading diagram of CFT columns subjected to axial force and lateral cyclic load

A typical loading diagram of CFT columns subjected to the axial force and a lateral cyclic load are shown in Fig. 2-2. In the experiment, the bottom of the specimens is usually fixed to a rigid foundation/reaction beam. In this type of experiment, the column-to-base connections were assumed to be not damaged during the test. The experimental studies focused on the column-to-base/beam connections will be discussed in the following sections. Axial force *P* is applied at the top of the column specimen by an axial hydraulic jack. In most of the summarized experiments, the axial force *P* held constant for the duration of the test. A load cell is usually inserted between the upper loading plate of the specimen and the hydraulic jack to measure and adjust the applied axial force. Lateral force is applied to the column top through one or several horizontal actuators (usually connected by steel connectors) and measured by load cells. During the test, strain gauges were usually installed at the surface of the steel tube along the column height direction to measure the steel strain as well as the column top displacement was usually measured by some linear variable displacement transducers (LVDTs) at the height of horizontal actuators.

The load patterns of lateral cyclic load, for example, are shown in Fig. 2-2. For most of the summarized experiments, the cyclic load was applied in a manner of displacement control in terms of the rotation angle θ or initial yield displacement of hollow steel tube δ_0 (as shown in Fig. 2). θ and δ_0 are defined as follow:

$$\theta = \delta / h \tag{2-1}$$

$$\delta_0 = H_0 h^3 / 3E_s I_s \tag{2-2}$$

$$H_0 = \left(\sigma_y - \frac{P}{A_s} \right) Z_s / h \tag{2-3}$$

Where the H_0, h, E_s, I_s and δ represents the initial yield force of steel tube, height of the column specimen, Young's modulus of steel, second moments of cross section of steel section and horizontal displacement of column top, respectively. σ_y, P, A_s and Z_s stands for the yield stress of steel, applied axial force, area of steel section and section modulus of hollow steel tube, respectively.

It should be noted that in the summarized experiment database, many different types of load protocol were applied by different researchers, as shown in Fig. 2-2. In some experiments, the horizontal displacement of column top increased by each cycle, while in some experiments the amplitude of horizontal displacement of column top remained constant for numbers of load cycles. This is to study on the effects of amplitude and number of cycles on the damage accumulation. Furthermore, a rare type of experimental study of CFT columns subjected to bi-directional spiral load (Goto et al. (2014)) is also included in the database, since past studies (Bruneau et al. (1996); Goto et al. (2009)) reveal that bidirectional load may have a great influence on the performance of structural columns under the earthquake.

2.1.2 summary of available experiment studies from literature

A database of experimental studies of CFT cantilever columns subjected to axial force and lateral cyclic load was established. The summarized experiment studies are summarized and listed in the Appendix. A. A total of 202 specimens from 23 research articles were reviewed in this study. In the Appendix. A, D stands for the dimension of the specimen according to the cross-section types which is shown in Fig. 2-3. Meanwhile t is thickness of the steel tube. σ_y is the yield strength of steel and σ_c is the compressive strength of the infilled-concrete. In the experiment database, four types of cross section of CFT columns are included, as schematically shown in Fig. 2-3, which are circular, rectangular, L-shape and Octagonal sections.

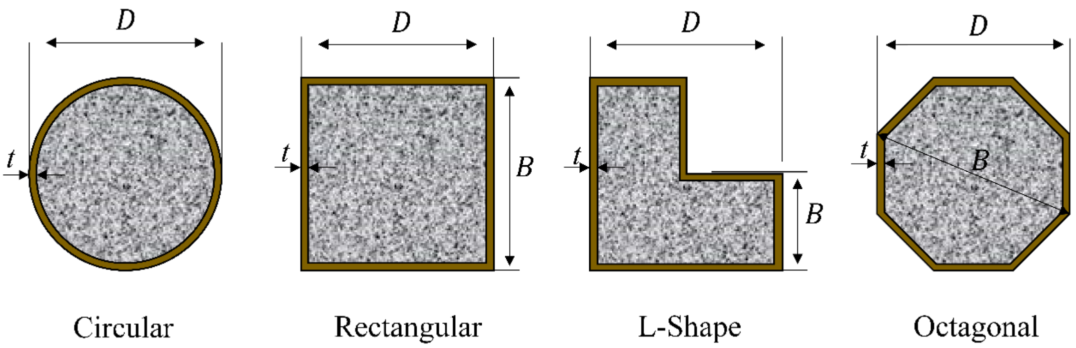

Fig. 2-3. Cross section types of experiment specimens

For the circular section, some limits of design parameters were adopted by some design specification codes to prevent the unreasonable designing including the instability and the metal brittle fracture caused by local buckling. These limits are summarized in the following equations (Japan Road Association 2012; Bruneau and Marson 2004; Roeder et al. (2010)):

ACI:

The steel pipe cross section must be at least 4% of the gross total column cross section area; and the thickness of steel tube should satisfy:

$$t \geq D\sqrt{\sigma_y / 8E_s} \tag{2-4}$$

AISC:

$$D / t \leq 0.15E_s / \sigma_y \tag{2-5}$$

AASHTO LRFD:

$$D / t \leq 2\sqrt{E_s / \sigma_y} \tag{2-6}$$

CAN/CSA-S16.1-M94:

$$D / t \leq 28000 / \sigma_y \tag{2-7}$$

(Unit of σ_y : MPa)

Eurocode 4:

The steel contribution ratio ϑ, must be:

$$0.2 < \vartheta < 0.9 \tag{2-8}$$

Where:

$$\vartheta = \frac{A_s \sigma_y / 1.10}{N_p} \tag{2-9}$$

N_p is the plastic compressive strength of the CFT columns;

And diameter to thickness ratio should be:

$$D/t \le 90\left(\frac{235}{\sigma_y}\right) \tag{2-10}$$

(Unit of σ_y: MPa)

Japan road association:

$$R_t = \left(\frac{r}{t}\right)\left(\frac{\sigma_y}{E_s}\right)\sqrt{3\left(1-\mu^2\right)} \le 0.12 \tag{2-11}$$

Where μ is the passion ratio of steel.

For the rectangular cross section, in the bridge construction, steel plates of CFT columns are usually installed with stiffeners to enhance the strength and ductility while the building columns are not. As shown in Fig. 2-4, with the presence of stiffeners, the buckling mode of steel plates under compressive force and bending moment is changed. A theoretical study (Lee and Yoo 2012) has been conducted and proved the stiffeners to ensure the plate-buckling behaviors and maximize the load-carrying capacity of the CFT columns.

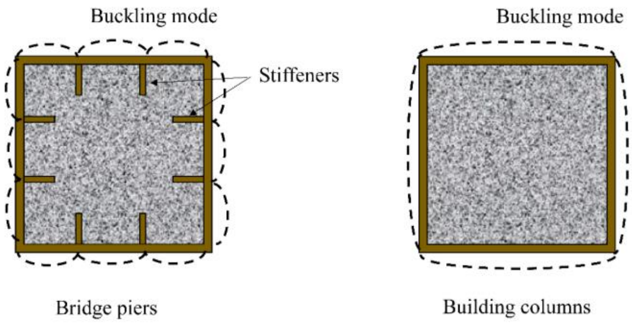

Fig. 2-4. Cross section of rectangular CFT columns used in bridge and building construction

Some limits of geometric parameters of rectangular CFT columns according to the design specification codes are summarized here (Han et al. (2014)):

AISC:

$$B/t \leq 5.00\sqrt{E_s/\sigma_y} \tag{2-12}$$

DBJ/T 13-51-2010:

$$B/t \leq 60\sqrt{235/\sigma_y} \tag{2-13}$$

Eurocode 4:

$$B/t \leq 52\sqrt{235/\sigma_y} \tag{2-14}$$

(unit: N/mm^2)

Compared to the conventional cross section CFT columns, the study and application of special shaped CFT columns are relatively limited. However, for example, protrusions of columns at corners in rooms in traditional frame structures may reduce the utilization ratio of area and disturb the aesthetic environment indoors. For saving architectural space and convenient arrangement for furniture, research interest to concrete-filled steel tubes columns with special shapes also increased. Hence, some experimental studies of special shaped CFT columns were included to the experiment database.

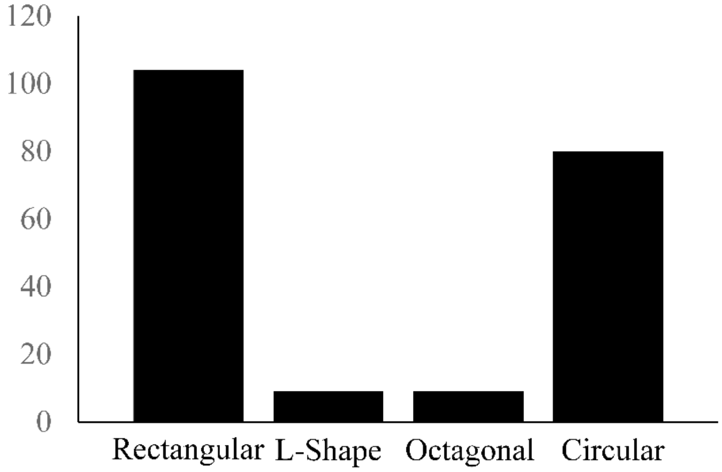

Fig. 2-5. Composition of experiment database

The composition of summarized experiment database is shown in Fig. 2-5 in terms of the cross-section type of specimens. 104 rectangular specimens, 80 circular specimens, 9 L-shape specimens and 9 octagonal specimens are contained in the database.

To figure out the coverage of past experimental studies on the CFT columns subjected to axial force and lateral cyclic load, the composition of experiment database was analyzed in the following figures.

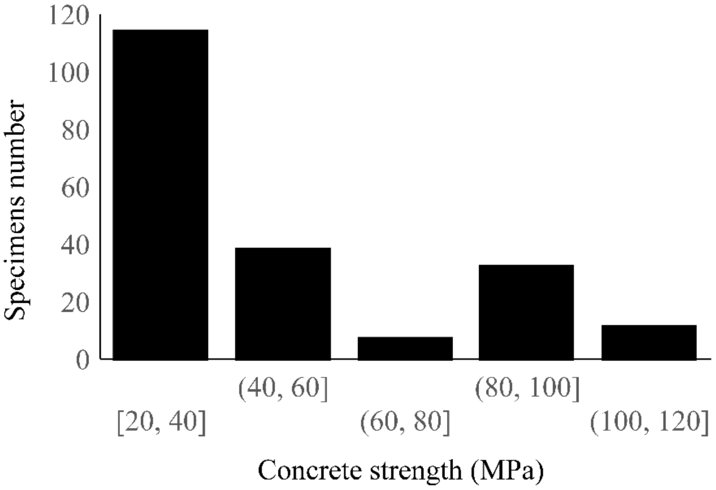

Fig. 2-6. Distribution of experimental specimens according to concrete strength

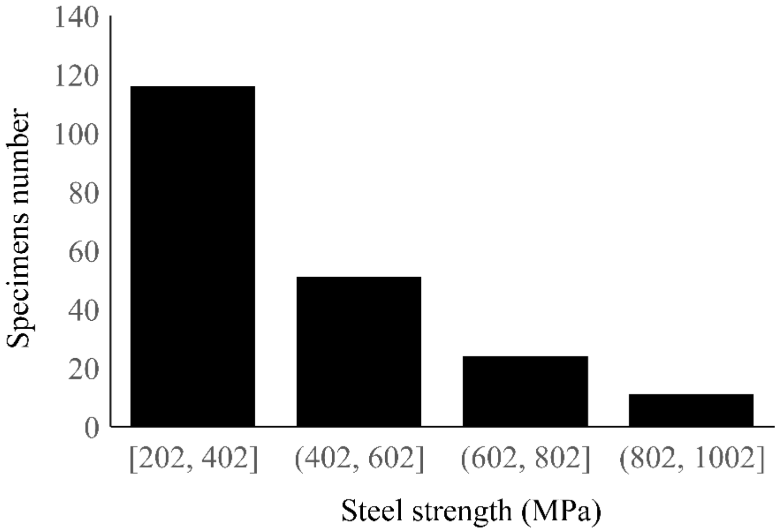

Fig. 2-7. Distribution of experimental specimens according to steel strength

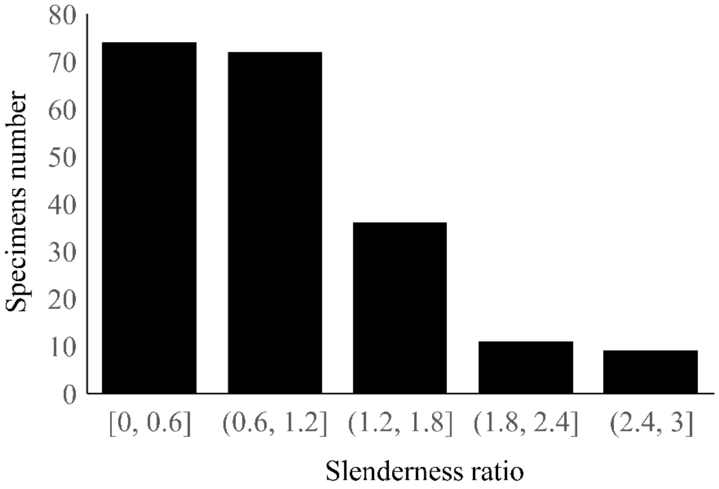

Fig. 2-8. Composition of experiment database according to slenderness ratio

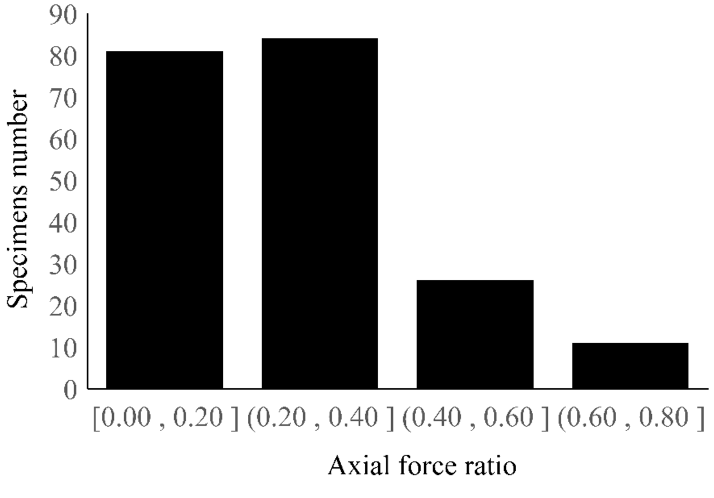

Fig. 2-9. Composition of experiment database according to axial force ratio

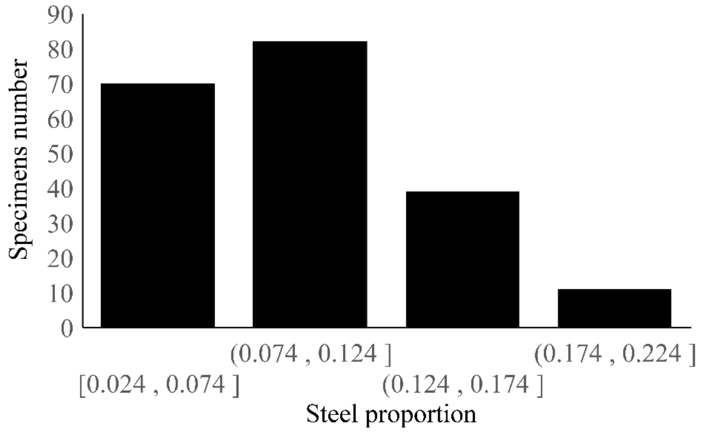

Fig. 2-10. Composition of experiment database according to steel proportion

From Fig. 2-6, the in-filled concrete used in the past experimental studies centralized under 40 MPa, while there are quite a few studies focus on the high strength in-filled concrete. Similar to the concrete, it can be seen from Fig. 2-7 that majority of research employed normal strength steel.

Fig. 2-8 shows the composition of the experiment database according to the slenderness ratio of column specimens. The slenderness ratio parameter of CFT column specimens is defined as follow:

$$\bar{\lambda} = \frac{1}{\pi}\sqrt{\frac{\sigma_y}{E_s}}\left(2h / r_s\right) \tag{2-15}$$

Where h denotes the height of the column specimen and the r_s is the radius of gyration of the column cross section. According to the Eq. (2-15), slenderness ratio is a parameter that could reflect the stability of column according to its geometric and material properties. From Fig. 2-8, most of the summarized specimens have a relatively low slenderness ratio below 1.2.

The axial force applied to the column specimens during the test were summarized in Fig. 2-9. However, there are several ways of expression of axial force ratio, for the convenience of comparison, axial force ratio of all the summarized experimental specimens were recalculated by the following equation:

$$\alpha = P / \left(\sigma_y A_s + \sigma_c A_c \right) \tag{2-16}$$

Where P is the applied axial force, σ_y and σ_c are the yield strength of steel and compressive strength of in-filled concrete respectively. A_s and A_c are the sectional area of steel and in-filled concrete respectively. It can be seen from Fig. 2-9 that most of the specimens are subjected to the axial force ratio under 0.4.

In Fig. 2-10, distribution of experimental specimens was discussed according to their steel proportion, which is defined as:

$$\delta = A_s / \left(A_s + A_c \right) \tag{2-17}$$

From the figure, experimental studies related to thin-walled CFT columns are much more than research focusing on the thick-walled CFT columns.

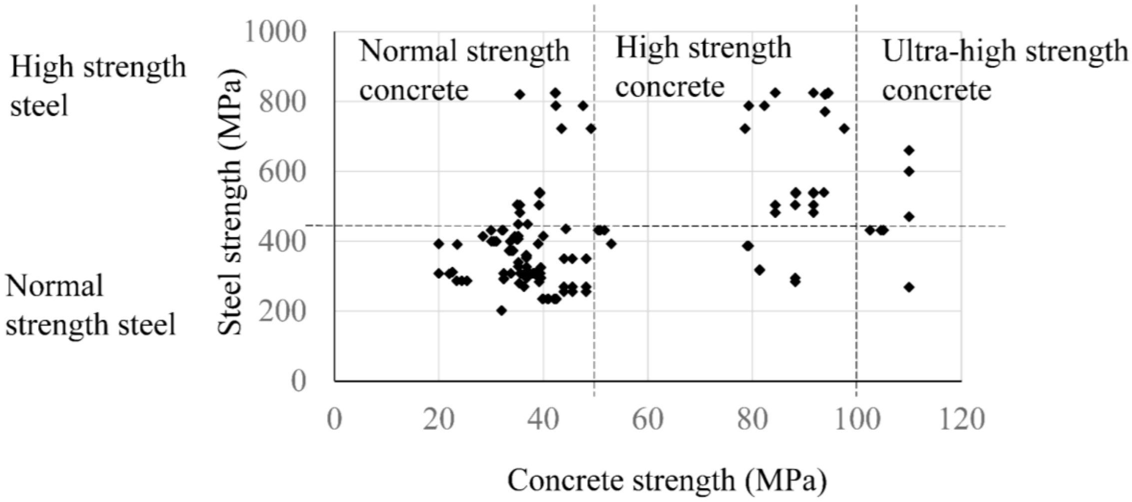

Fig. 2-11. Summary of material properties of CFT column specimens used in the past experimental studies

A scatter plot of summary of material properties of specimens in the experiment database is presented in Fig. 2-11. A general definition of steel and concrete is adopted to define the material according to their strength. Normal strength steel is the steel with the yield strength under 425 MPa. If the compressive strength of concrete is under 50 MPa, it can be defined as normal strength concrete, while the high strength concrete has the compressive strength between 50 and 100 MPa. Ultra-high strength concrete is defined as the compressive strength larger than 100MPa. Form the Fig. 2-11, studies focus on CFT columns using normal concrete and normal steel is the most common. Studies related to CFT columns using high strength concrete and high strength steel is the second most common. Studies focus on the application of ultra-high strength concrete is relatively limited.

2.1.3 Experiment behaviors of CFT columns subjected to axial force and lateral cyclic loading

- ***Fully concrete-infilled circular CFT columns***

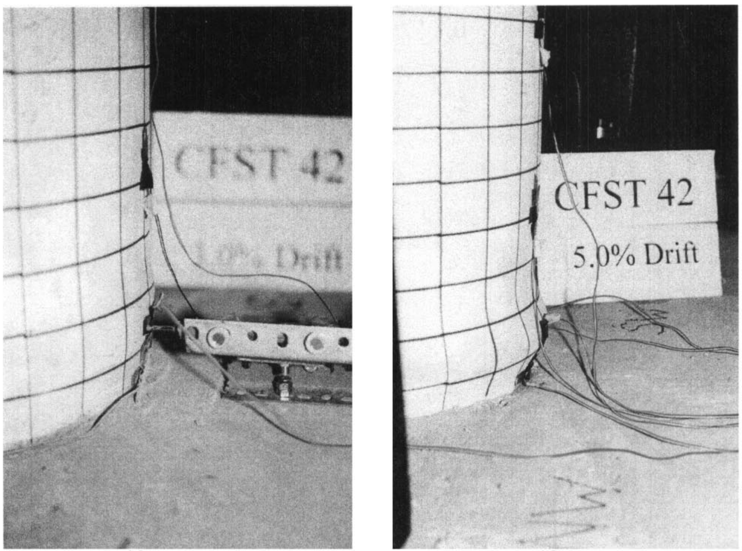

Drift 1.0% Drift 5.0%

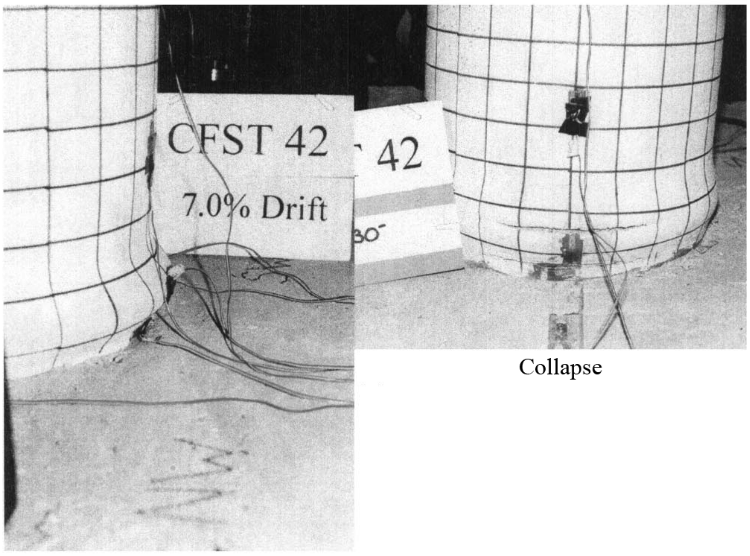

Collapse

Drift 7.0%

Fig. 2-12. Failure mode of fully concrete-infilled CFT columns subjected to axial force and lateral cyclic load (Marson and Bruneau 2004)

The experimental results obtained by Marson and Bruneau (2004) is used herein to illustrate the failure mode of fully infilled CFT columns. Shown in Fig. 2-12 is the specimen CFST 42 with 406.4 mm diameters, 9.53 mm wall thickness and 2200 mm height. During the test, with the increasing of the column top lateral displacement, the moment-drift curve of the specimen firstly grown elastically within the 1% drift, as shown in Fig. 2-13. Initial yielding of the steel at the steel tube was observed at 22 mm lateral displacement, which coincides with 1% drift. A very slight buckle of steel tube was observed at 2% drift.

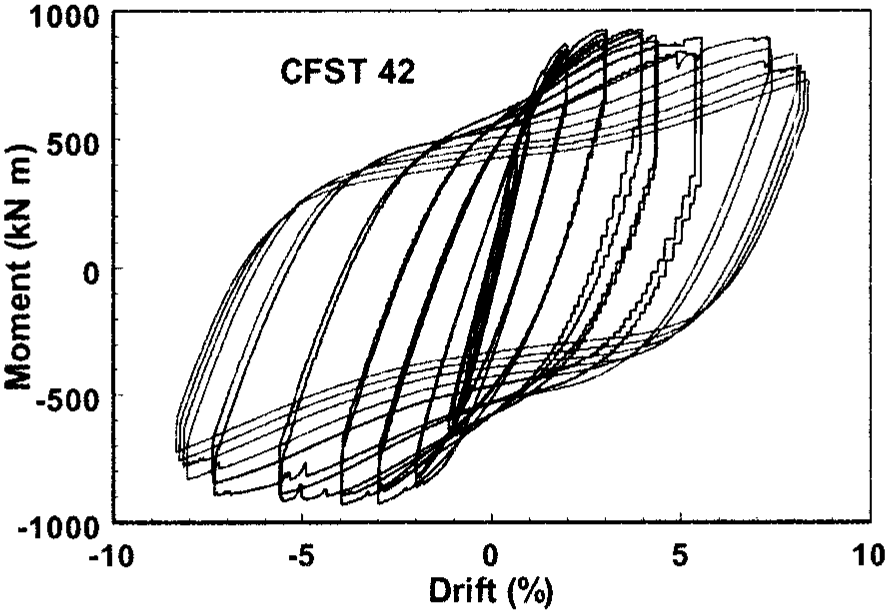

Fig. 2-13. Failure mode of partially concrete-infilled CFT columns subjected to axial force and lateral cyclic load (Marson and Bruneau 2004)

The maximum horizontal force resistance of the CFT column specimen was 400 KN and was reached at 3% drift. The specimen continuous to resist this horizontal force until the end of 5% drift cycle. In this process, the buckle of steel tube firstly occurred at one side at 3% drift and continued grown at both side at 4% drift. At 5% drift, the buckle of steel tube had grown to encompass the entire diameters of column, while no cracks of steel were observed at this stage. Furthermore, the column became slight leaning to the side where local buckling was more severe.

At around 7% drift, some small hairline cracks were seen around the buckle. Simultaneously, necking of the steel shell was observed at the forth cycle of 7%. The crack developed to both sides with the progress of the test. Finally, with a bang (sound), the crack propagated to a length of 260 mm, as shown in Fig. 2-12 (d). Moreover, another crack on the other side with the length of 233 mm was observed. Correspondingly, the load resistance was gradually decreased from 400 KN to 60 KN at the end of the test. In this specimen, the cracks of steel tube on the both sides were not penetrated the steel column. However, it was observed in other tests that a penetrated crack was developed with the collapse of the specimen.

- ***Partially concrete-infilled circular CFT columns***

CCFT4.0-2

(a) Experimental study of Goto et al. (2014)

S-25 S-50

(b) Experimental study of Yuan et al. (2014)

Fig. 2-14. Failure mode of partially concrete-infilled CFT columns subjected to axial force and lateral cyclic load

Fig. 2-14 shows the status of partially infilled circular CFT column specimens after the test. Fig. 2-14 (a) is the specimen subjected to axial force and bi-directional cyclic load, obtained by Goto et al. (2014), while Fig. 2-14 (b) is the specimens subjected to axial force and uni-directional cyclic load, obtained by Yuan et al. (2014). The difference between specimen S-25 and S-50 is that the height of infilled concrete, which are 25% and 50% of the height of the column, respectively. According to those figures, the failure mode of partially infilled circular CFT columns subjected to axial force and lateral cyclic load can be summarized as the outward local buckling of steel tube at the column base or the so called ‘elephant foot buckling’.

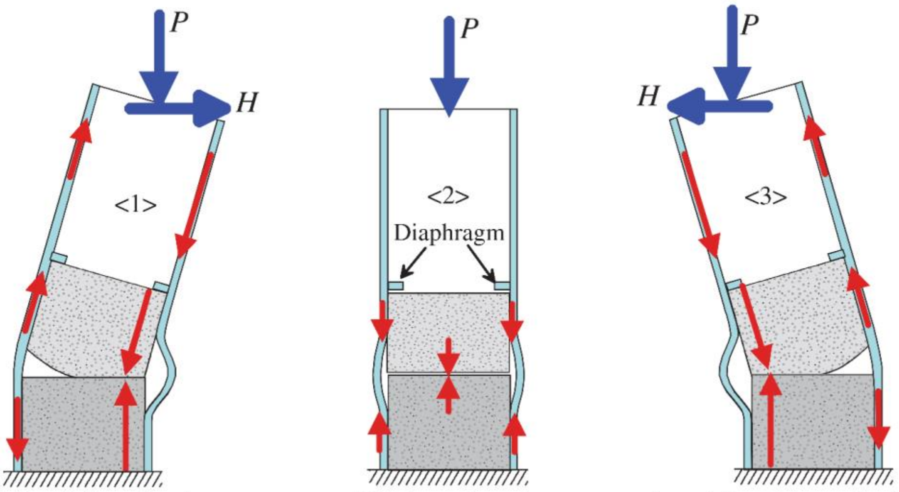

* Buckling deformation is streched by tensile force.
*Compressive force is carried by in-filled concrete.

* Horizontal crack in in-filled concrete is opened.

* Buckling deformation is streched by tensile force.
*Compressive force is carried by in-filled concrete.

Fig. 2-15. Buckling restraining mechanism of partially infilled CFT columns under axial force and lateral cyclic load (Goto et al. (2014))

Meanwhile, a local buckling restraining mechanism of partially infilled CFT columns with diaphragm under this loading condition were explained by Goto et al. (2014) in detail. Before local buckling deformation occurs in the outer steel tube, the compressive axial force is carried by the steel tube and in-filled concrete. Under the alternate horizontal load, the axial force of the steel tube oscillates according to the cycles of the applied alternate horizontal load. However, the center of this oscillating axial force remains at almost the same location before the local buckling deformation occurs in the steel tubes. When the local buckling deformation develops in the steel tube, the center of the oscillating axial force in the steel tube gradually changes from compression to tension with the increase in the loading cycles of the alternate horizontal load. At the same time, the amplitude of the oscillating axial force in the steel tube increases, which implies that the tension value of the oscillating axial force in the steel tube becomes larger than its compression value after local buckling deformation occurs. Finally, the predominant tension value of this oscillating axial force restrains or restores the local buckling deformations of the outer steel tube by stretching the local bulges repeatedly.

The above behavior of axial force distribution during the loading process is graphically shown in Fig. 2-16. The causes of this axial force distribution in the composite columns is attributed to the mechanism shown in Fig. 2-15. The local buckling deformation of PCFT columns results in a compressive deformation of the outer steel tube. This compressive deformation increases the contact pressure between the in-filled concrete and diaphragm installed on the steel tube at the location of the upper surface of the in-filled concrete. As a result, more of the compressive axial force is transferred from the steel tube to the in-filled concrete, and the magnitude of the compressive axial force acting on the buckled portion of the steel tube section is reduced. However, the tensile axial force produced by the bending moment acts primarily on the steel tube section at the buckled part of the PCFT columns because the tensile axial force cannot be resisted by the in-filled concrete section after a penetrated horizontal crack occurs. In addition, the dilation of the in-filled concrete under alternating load lifts the diaphragm of the steel tube and further increases the tensile axial force at the buckled portion of the steel tube.

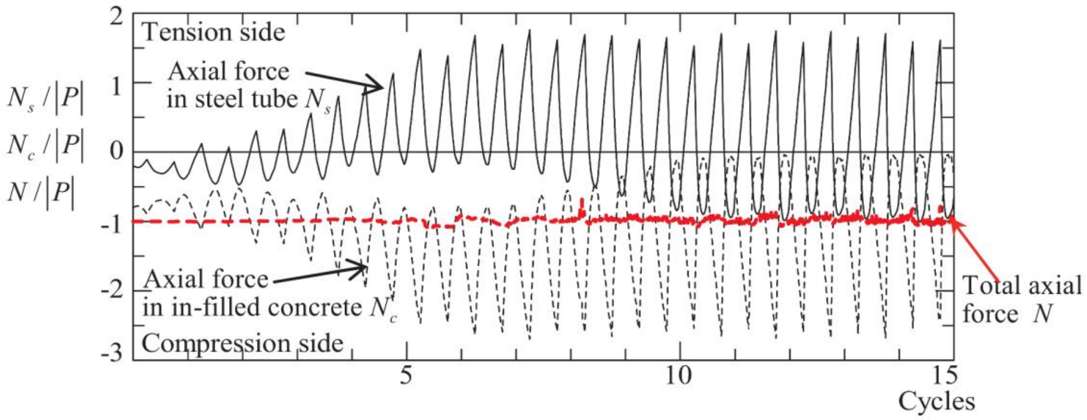

Fig. 2-16. Buckling restraining mechanism of partially infilled CFT columns under axial force and lateral cyclic load (Goto et al. (2010))

- ***Fully concrete-infilled rectangular CFT columns***

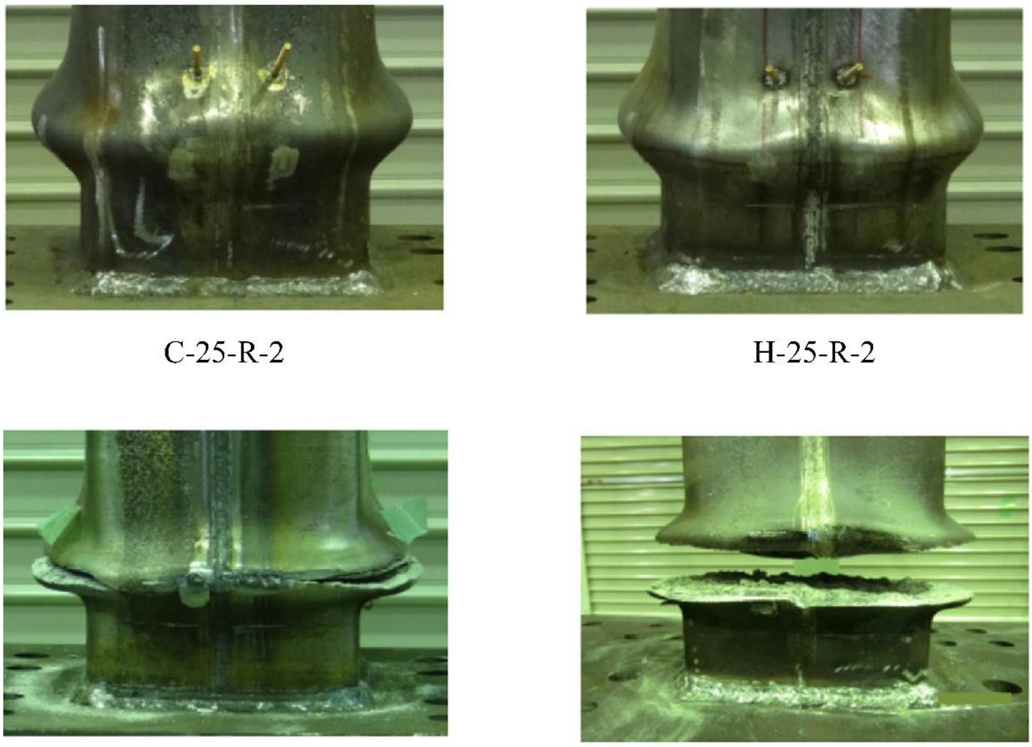
C-25-R-2 H-25-R-2

C-25-R-20 H-25-R-20

Fig. 2-17. Failure mode of fully concrete infilled rectangular CFT specimens (Skalomenos et al. 2016)

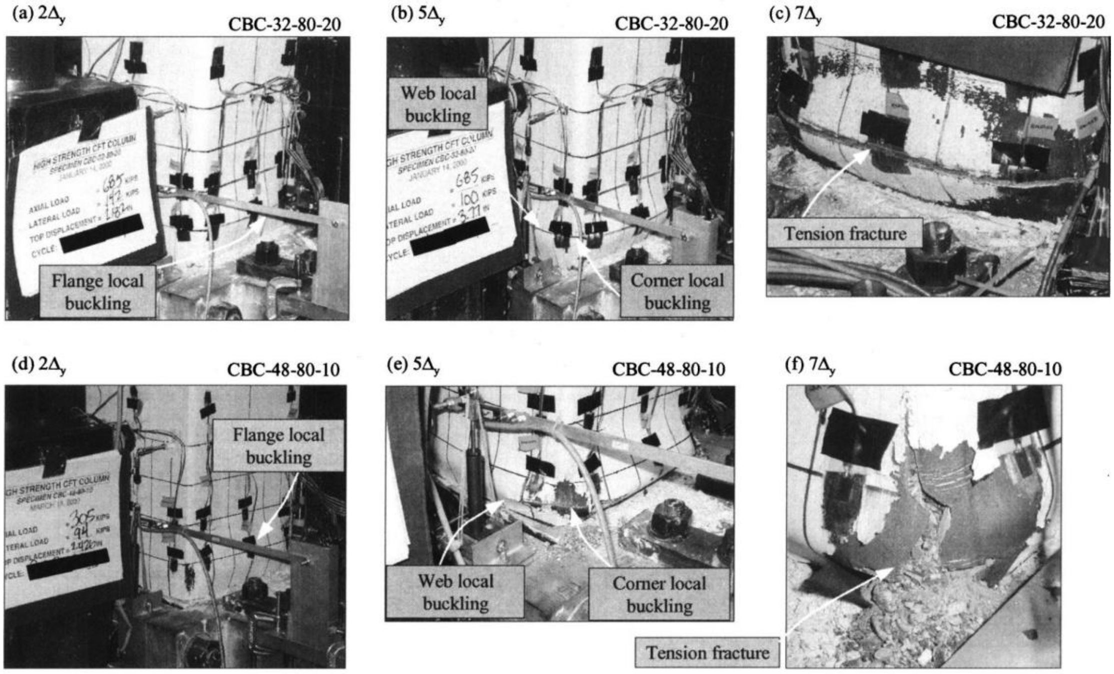

Fig. 2-18. Failure mode of fully concrete infilled rectangular CFT specimens (Varma et al. (2004))

The experimental results of Skalomenos et al. (2016) is summarized here. The specimens adopted in the test have the width of 150 mm and 6mm wall thickness. As shown in Fig. 2-17, for specimens with the loading pattern that 2 cycles at each drift, C-25-R-2 and H-25-R-2, the failure mode of the fully concrete infilled rectangular CFT columns is the outward local buckling of the steel plate slightly above the column base. For specimens with the loading pattern that 20 cycles at each drift, a penetrated crack was developed both in the steel tube and infilled concrete.

The experiment conducted by Varma et al. (2004) is shown in Fig. 2-18. The experimental behaviors of CFT column specimens are summarized in terms of a series of important events occurred during the process of the test. This series of significant events are: tensile stress in concrete; yielding of steel tube flange in compression; extreme concrete compression fiber reaches cylinder failure strain; yielding of steel tube flanges in tension; initial crushing of concrete; local buckling of steel tube flange; local buckling of steel tube webs; local buckling of steel tube corners; tension cracking or fracture of steel tube corners. As shown in Fig. 2-18, the ultimate state of rectangular CFT column specimens are the tensile cracks of the steel flanges and steel tube corner caused by the outward local buckling just above the column base.

- Partially concrete-infilled rectangular CFT columns

Specimen S-20 Specimen S-40

Fig. 2-19. Failure mode of partially concrete infilled rectangular CFT specimens (Yuan et al. (2013))

The experiment results of partially concrete infilled rectangular CFT columns obtained by Yuan et al. (2013) are shown in Fig. 2-19. The specimen S-20 has the infilled concrete with the height of $0.2H$ while the S-40 has the infilled concrete height of $0.4H$. As illustrated in above, the partially concrete infilled rectangular CFT columns are usually installed with longitudinal stiffeners and diaphragm at the upper surface of the infilled concrete. Hence, the steel plate is divided into several sub panels and shows the buckling mode as predicted in Fig. 2-4. For the specimen with enough height of infilled concrete, the ultimate state of the column is that the outward local buckling of steel sub panels just above the column base and the cracks at the corners. However, if the infilled height is not enough, like the specimen S-20, the local buckling and fracture of steel tube occurred just above the cross section of the infilled concrete.

According to the experiment results, it is necessary to determine an appropriate infilled height of concrete to preclude the failure of hollow section. The following equation is recommended by the design specification (Japan Road Association, 2012) to decide the height of infilled concrete:

$$h_c > \left(1 - \frac{M_{ys}}{M_a}\right) h \tag{2-18}$$

Where the M_{ys} is the yield bending moment of hollow steel cross section immediately above the concrete-filled portion, and is defined as:

$$M_{ys} = \left(\sigma_y - \sigma_N\right) Z_g \tag{2-19}$$

σ_N is the steel stress due to the axial force; Z_g is the section modules of the hollow steel section. M_a is the allowable bending moment of the steel–concrete composite cross section at the base.

- ***Special shaped CFT columns***

Outward local buckling of the steel tube (specimen S1)

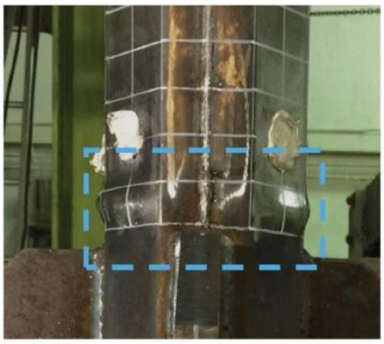

Outward local buckling as elephant foot (specimen S5)

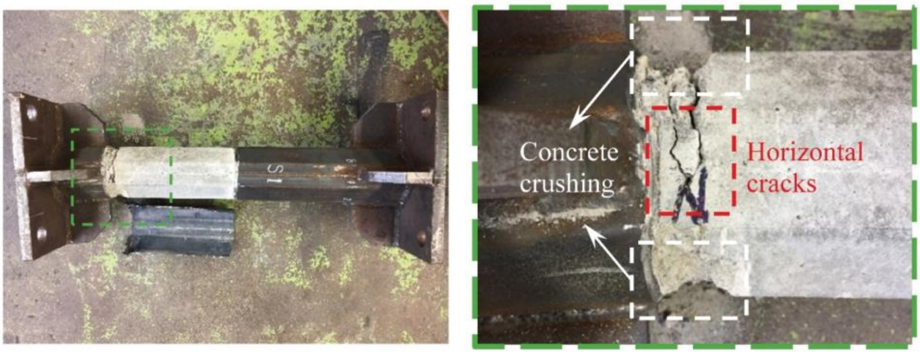

Concrete cracks and concrete crushing (specimen S1)

(a) Failure mode of octagonal CFT columns (Chen et al. (2019))

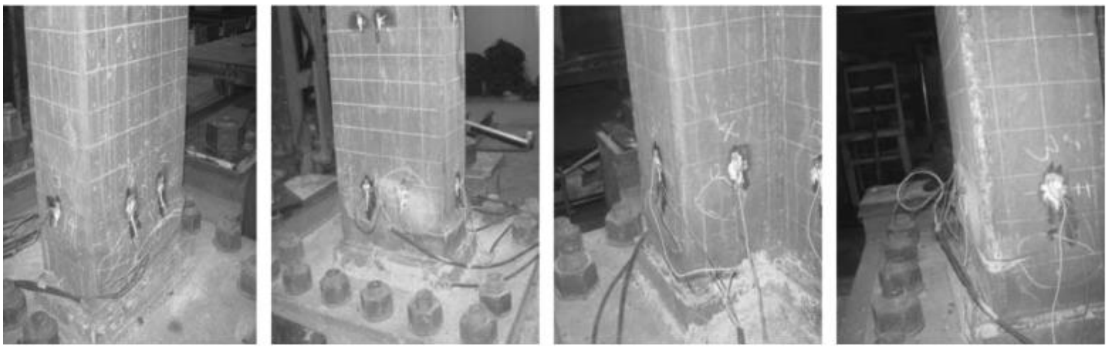

(b) Failure mode of L-shaped CFT columns (Shen et al. (2016))

Fig. 2-20. Failure mode of special shaped CFT specimens

The failure mode of octagonal CFT columns subjected to axial force and lateral cyclic load observed in the test conducted by Chen et al. (2019) is shown in Fig. 2-20 (a). In general, significant outward local buckling developed at the base of the column, just above the vertical stiffeners. Based on the measured data from the steel strain gauges, local buckling of the steel tube initially formed at the compression side following the steel yielding. Subsequently, when the cyclic load reversed, the local buckling occurred at the opposite side. With the process of the test, lateral displacement amplitude increased. The local buckling of the steel tube became more and more obvious and finally grew as an elephant foot buckling. Cracks of the steel tube developed at the drift ratio of 6%. Moreover, to investigate the damage of the infilled concrete, the specimens were cut at the location of the local buckling region. Several horizontal cracks were observed in the infilled concrete.

An experimental result obtained by Shen et al. (2016) is used herein to illustrate the failure mode of L-Shaped CFT columns subjected to axial force and lateral cyclic load. A failure in a ductile manner including the obvious outward bugles of the steel tube at the column base and tearing of the weld part were observed in all specimens. Under the lateral displacement of Δ_y, the specimens were in the elastic stage. outward local buckling developed when the lateral displacement reached 2 or $3\Delta_y$ at the compressive side. But the maximum horizontal load was not reached at this time. With the lateral load reversed, local buckling also occurred at the other side. There are six faces of L-shaped CFT columns. With the increasing of the lateral cyclic load, local buckling developed on all the surfaces of the steel tube and became more severe. Finally, in some specimens, weld of one of the bottom corners of the column was torn, and the lateral resistance dropped sharply. The buckling region of the steel tube of all the specimens is summarized at about 100-150 mm above the base. The infilled concrete was checked after test, and serious crushing were observed.

2.2 Experimental studies focusing on the lateral cyclic loading behavior of column to base/beam connections

The experimental behaviors of CFT columns subjected to the axial force and lateral cyclic load has been reviewed and discussed in detail in the previous section. Generally, the ultimate state of cantilever CFT columns under this load condition can be summarized as the severe outward local buckling of steel tube slightly higher than the column base accompanying tearing of the steel and penetrated cracks in the infilled concrete. However, in those experimental studies summarized in the previous section, the column to base connections were assumed to be rigid or strong enough up to the collapse of the column specimens. In the real structures, this kind of favorable seismic performance can be guaranteed only when the adequate design details of footing connections are employed. The loads such as gravity and seismic loads carried by the columns must be transferred down through the footing to the soil/rock. A robust column base connection is hence quite important for ensuring the structure to collapse in a ductile manner just like summarized in the previous section. Therefore, although this topic is not the focus of this study, some experimental studies focusing on this subject are briefly reviewed in this section.

- Han et al. (2019)

An experimental study focusing on the embedded type of the base connection was performed by Han et al. (2019). In their study, the relationship between design and column base performance were investigated. The details of the tested specimens are shown in the Fig .2-21 (a). Totally, 7 square CFT specimens with different embedded length were used in this study. As shown in the figure, the concrete of the foundation was cast in two pouring. A part with length of D_a is for the anchor bolts, and the other part with the length of D_e is for the embedment of the column. The setup of the experiment was shown in Fig. 2-21 (b). During the test, the specimens were subjected to the constant axial force load and lateral cyclic load. The magnitude of the axial force was 15% of the axial sectional strength of the CFT column, which can be calculated by the Eq. (2-16). The lateral force was applied with each increasing drift. At each drift, 2 cycles were employed. Strain gauges were installed at the surface of steel tube and the anchor bolts to evaluate the performance of the specimens.

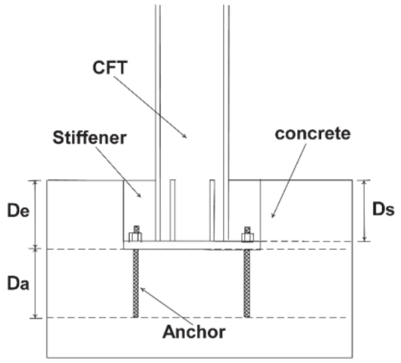

(a) Details of embedded based connection

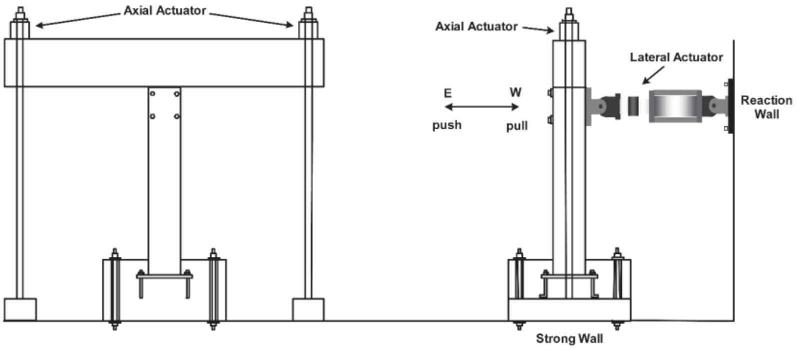

(b) Details of experimental setup

Fig. 2-21. Details of specimens and test setup of Han et al. (2019)

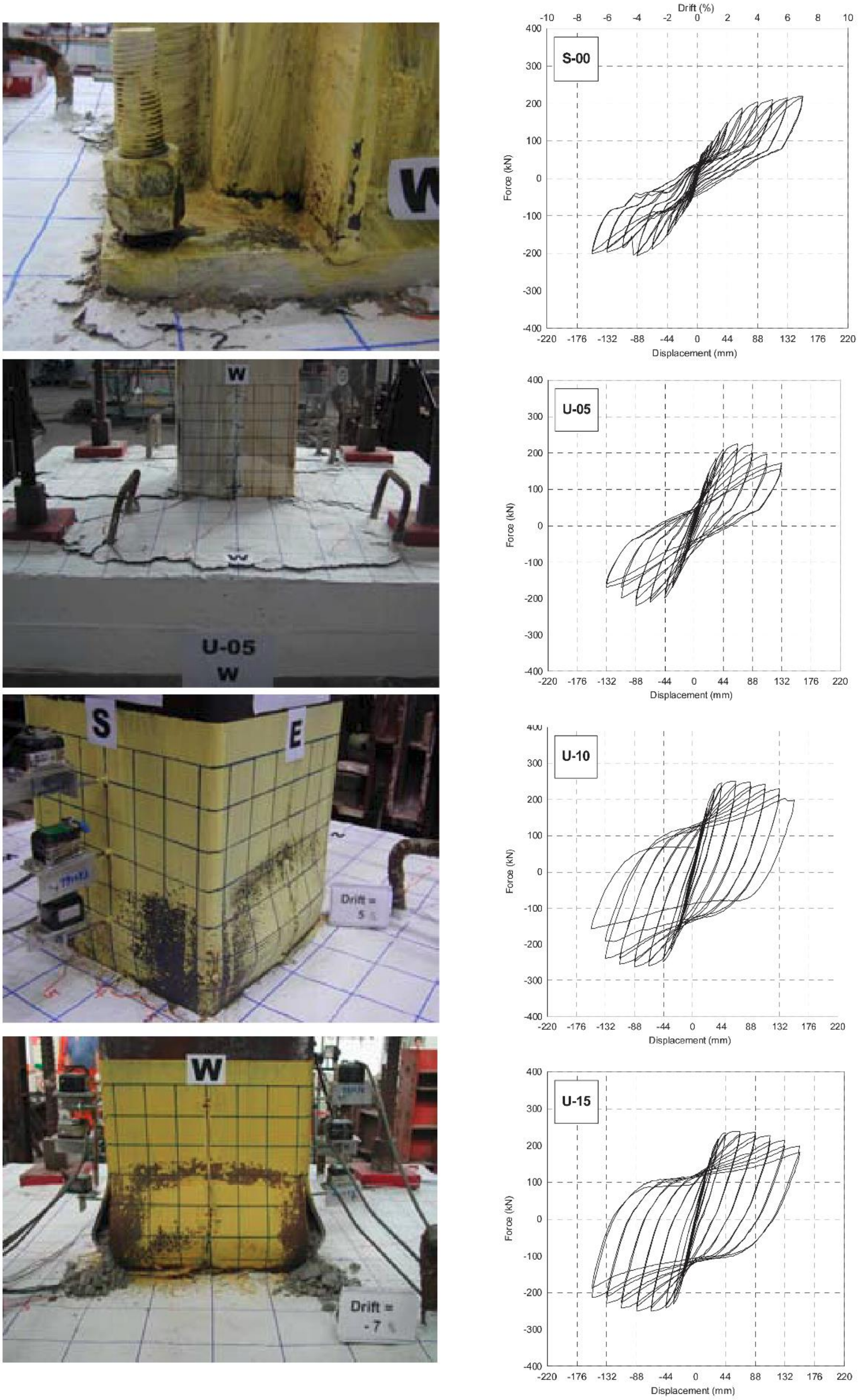

Fig. 2-22. Results obtained by Han et al. (2019)

Fig. 2-22 shows the results of Han's experiments (Han et al. (2019)). From the drift-horizontal force relationship corresponding to the failure modes of the specimens, the in adequate design of base connection may cause the failure of the foundation and the CFT columns cannot reach their ultimate capacity. If the premature cracks occurred, as shown in the figure, the energy dissipation capacity was far less than specimens failure in the ductile manner (outward local buckling and fracture of the steel tube of the column base).

- Lehman's study (Lehman et al. (2015); Lehman and Roeder 2012; Roeder et al. (2018); Stephens et al. (2016a, 2016b, 2018))

In the United States, the application of CFT columns in the building and bridge construction are not as common as in Asia, primarily due to the limit of research on the connections between column and base/ cap beam. Therefore, a series of studies on the seeking of a standard connection form that could provide reliable resistance under the earthquake were conducted by Lehman (Lehman et al. (2015); Lehman and Roeder (2012); Roeder et al. (2010, 2018); Stephens et al. (2016a, 2016b, 2018)).

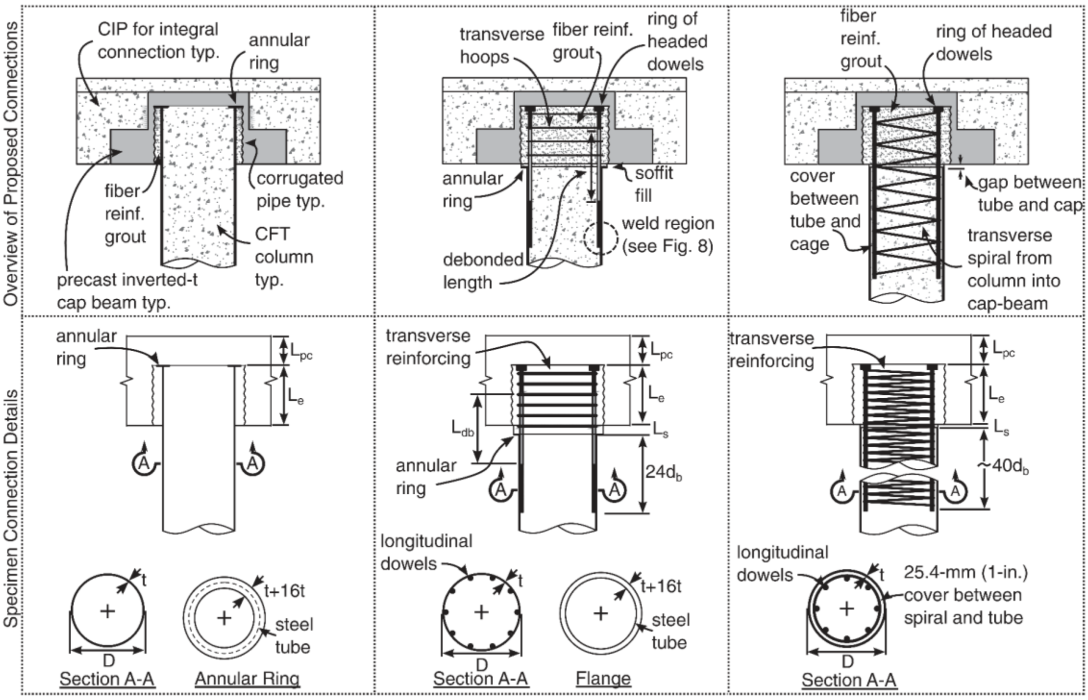

(a) Details of beam to column connection (Stephens et al. 2016a)

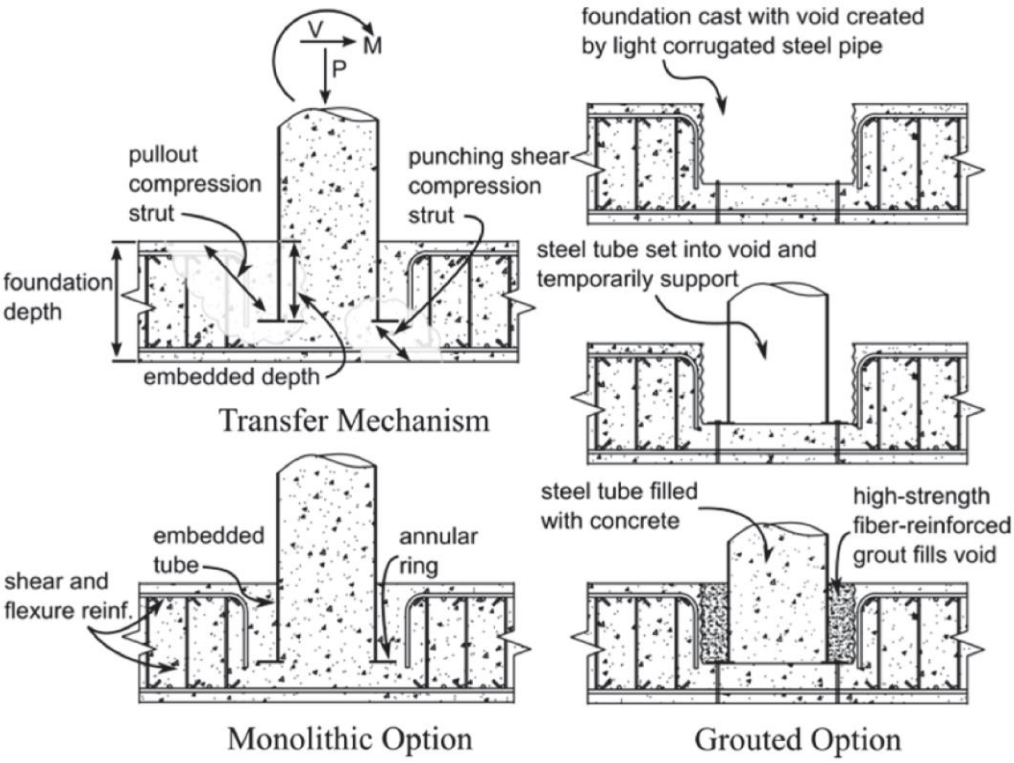

(b) Details of column to base connection (Stephens et al. (2018))

Fig. 2-23. Proposed column to base/ beam connections by Lehman.

As shown in Fig. 2-23 (a), are the three types of proposed column to cap beam connections. There are embedded CFT annular ring (ER) connections; welded dowel (WD) connections; RC connections.

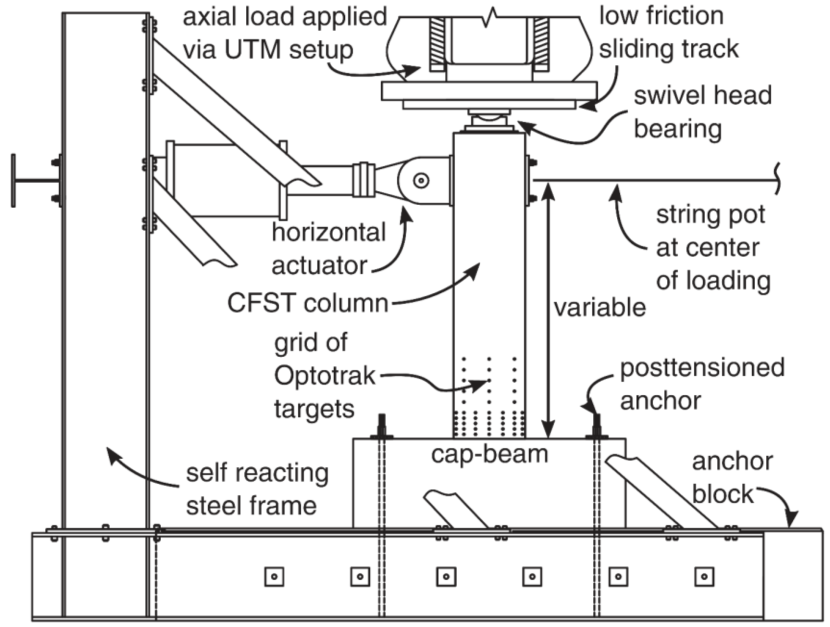

*Note: Test setup illustrated using a typical transverse specimen.

(a) test setup (Stephens et al. (2016a))

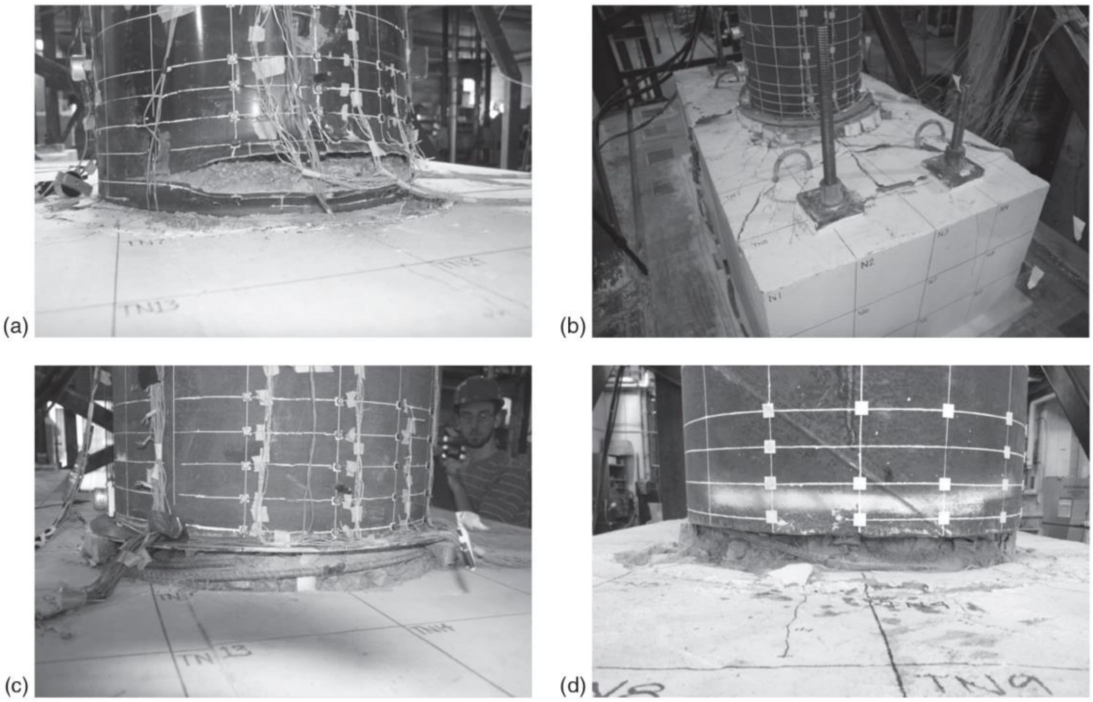

(b) experiment behavior (Stephens et al. (2016a)): (a) ER connection; (b) (c) WD connection; (d) RC connection.

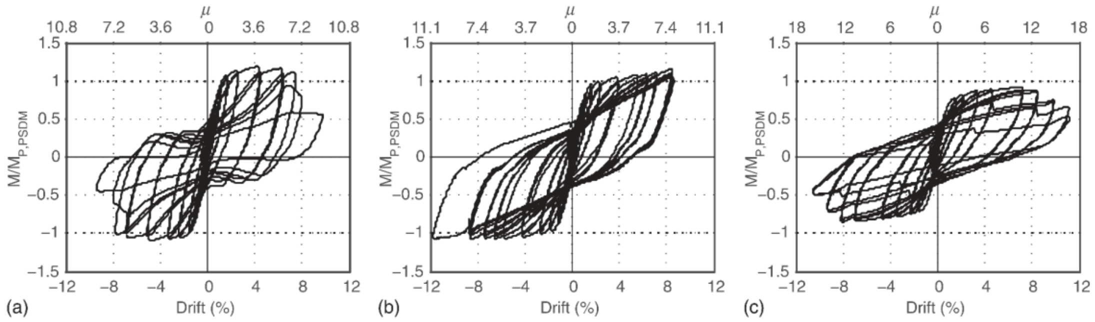

(c) load-drift curves (Stephens et al. (2016)): (a) ER connection; (b) WD connection; (c) RC connection

Fig. 2-24. Cyclic load test of column to cap beam connections (Stephens et al. (2016a))

The cyclic load test was conducted using a self-reacting frame that graphically shown in Fig. 2-24 (a). the specimens were subjected to the load protocol developed by the ATC-24. 5% or 10% constant axial force of the cross-sectional capacity of the composite column was applied to the specimen top. The typical moment-drift curves of each kind of connections were plotted in Fig. 2-24 (c) and the collapse mode of the different type of connections were shown in Fig. 2-24 (b).

According to the experimental results, ER connections provide large strength, stiffness, and deformation capacity. The failure mode of this type of connection was tearing of the steel tube near the column to cap bam interface which is the ideal type collapse. Based on the parametric study, the cap beam width should be at least 2 times of the diameters of the CFT column. For the WD connection, the strength is decided by the effective reinforcing ratio of the dowels. The failure mode of this type of connection varies from the cap beam failure to the yielding and fracture of the longitudinal dowels within the soffit fill region. The RC connection showed significantly lower stiffness and strength. The failure mode of this type of connections was characterized by yielding and fracture of the longitudinal reinforcing in the gap between the steel tube and the cap beam. In conclusion, the authors recommend the ER connection for reliable CFT bridge piers against earthquakes. The details of their studies on the column to base connection is not introduced in this thesis. The ER connection was better than other types of the connections (Lehman and Roeder 2012; Stephens et al. (2018)).

- Li et al. (2019)

Li et al. (2019) studied seismic performance of an encased CFT column base connections. In an encased column base connection, a base-plate of the CFT column is partially encased by a reinforced concrete of an outer component, as shown in Fig. 2-25 (a). The test method is explained in Fig. 2-25 (b). The cyclic load is given by a $500KN$ hydraulic actuator and the axial force is applied to the column top by two high-strength steel rods. The parameters studied based on the experimental observation were the height of the outer concrete component, steel tube wall thickness and the different types of steel rebars.

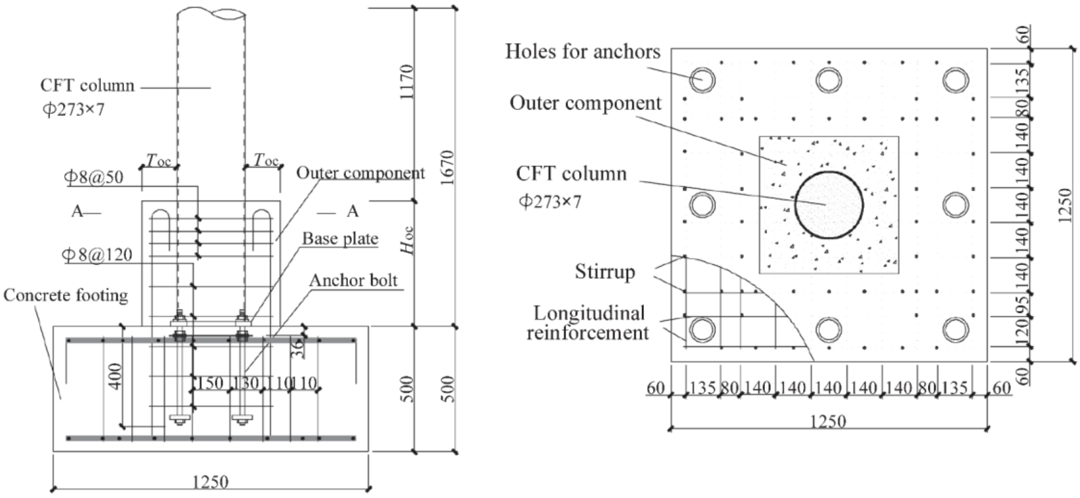

(a) Details test specimens

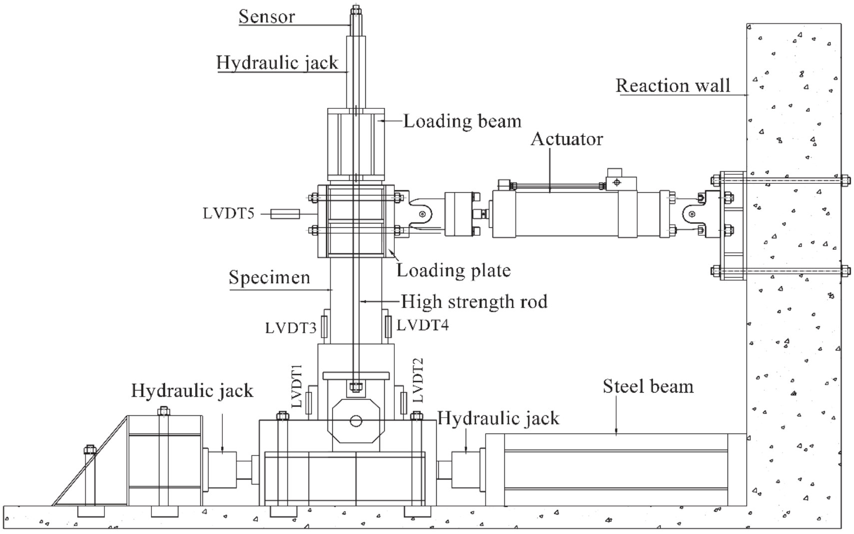

(b) Details of experiment setup

Fig. 2-25. Details of the test specimens and the test method of encased type of CFT columns (Li et al. (2019))

Two types of specimens were studied by the cyclic load test. The difference between each type is the existence of confinement to outer components given by steel warps. For the specimens with steel wraps, the failure mode was characterized by the plastic hinge failure of the steel tube above the outer components. For the specimens without steel wraps, the failure mode was dominated by the diagonal shear cracking and punching shear cracking of the concrete outer components. As shown in the experimental load-drift curves, the thicker is concrete component, the more obvious is the pinching behavior. The stiffness of the entire CFT column decreased with the reduction of the height of the outer concrete component. The conclusion obtained by this study was that the encased base connection with steel wraps and shear studs could provide desirable seismic resistance. The final failure mode, plastic hinge at the CFT column section, is an ideal type of failure mode of the piers.

2.3 CFT columns subjected to dynamic loading

To study seismic behaviors of CFT columns, the general way is conducting a cyclic load test of the single CFT columns. However, in the real earthquake, multi-directional components of the earthquake act simultaneously on structures. The cyclic load test in a simple form may not reflect a real response of structures under an earthquake. During the past two decades, the rapid progress in experimental systems makes it possible to carry out experimental study in a way of the consistent with the actual situation. To this end, some experimental studies conducted in the more advanced method are introduced herein.

2.3.1 Pseudo dynamic test

To study the dynamic behaviors of CFT columns in a more realistic way, a pseudo-dynamic method can be used. In the pseudo dynamic load test, a seismic response of a structure is numerically simulated by an online computer. In the test, although load is applied quasi-statically, the dynamic effects are simulated numerically to achieve the realism of a dynamic test. As shown in Fig. 2-26, the test system can be idealized as a single-DOF model. During the test, the external load is controlled in a step by step fashion according to the feedback from the measurement and calculation based on the dynamic equilibrium equation of the corresponding numerical model. The equation is usually solved by an explicit integration method.

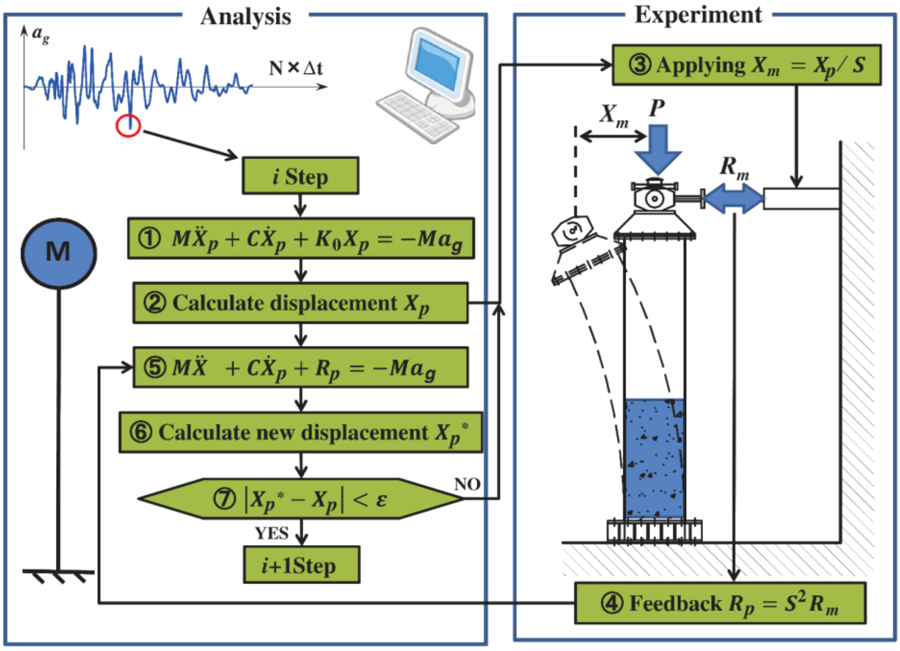

Fig. 2-26. Conceptual flow of a pseudo dynamic loading test (Yuan et al. (2014))

In the study of Usami et al. (1997), three rectangular partially concrete-infilled CFT column specimens and one steel hollow specimen were investigated by the pseudo dynamic loading test. The objective of their study was to discuss the effects of the infilled concrete and the natural period of the specimens. Hence, the natural periods of three CFT specimens were designed as 0.635, 0.929 and 1.365 respectively. A natural period of the specimen was calculated based on the following equation:

$$T = 2\pi\sqrt{M / K} \tag{2-20}$$

Where M is the mass and K is the stiffness of the specimen.

The input earthquake acceleration used in the study is the JMA wave of the Hyogoken Nanbu Earthquake on the 17th of January 1995, which was obtained from a hard ground type called Ground type I according to the specification of Japan (Japan Road Association, 2012).

Their study can be summarized as follows. From the comparison of the hysteretic curve of the steel hollow specimen and concrete infilled specimen, the maximum response displacement and the maximum reactional force were almost the same. From the comparison between the time history curves of two types of the specimens, infilled concrete can reduce the residual displacement of steel columns after earthquakes, therefore, the seismic performance of a hollow steel column is upgraded. Meanwhile, the experimental results showed that the natural period has a big influence on the seismic behavior of the CFT columns. To sum up, the specimen with lower natural period had larger response displacement, reaction force and residual displacement.

A series of more comprehensive pseudo dynamic loading studies were carried out by Yuan et al. (2013, 2014). In their studies, 9 circular and 27 rectangular partially concrete infilled CFT specimens were tested. Like Usami's study, the effect of the infilled concrete was firstly investigated. In addition, the influence of the bi-directional earthquake motion was considered. Moreover, in their study on the rectangular CFT columns, the effect of different ground types was examined. The employed earthquake acceleration was the JRT wave (Yuan et al. (2013). All specimens were classified into several subgroups. In each subgroup, three specimens were subjected to JRT-NS, JRT-EW and bi-directional earthquake acceleration respectively.

The results of their studies are summarized below. Firstly, the effect of infilled concrete on the residual displacement of CFT columns was again confirmed by the experimental results. Moreover, collapse of the columns was observed on those specimens subjected to the bi-directional earthquake acceleration, while the specimen under the uni-directional load did not fail. Since in real earthquakes, structures are subjected to multi-directional earthquake load, it is necessary to consider structural behaviors in a more realistic situation. The type of the ground will have large influence on the cumulative energy absorption.

2.3.2 shake table test

As the most practical type of experimental study to investigate dynamic behaviors of structures, a shake table test can simulate the multi-directional components of regional ground motion. However, the cost of this type of experimental study is relatively high compared with quasi-static load test and hybrid load test. Hence, there are only a small number of the shake table tests of the CFT columns available in the literature.

Based on the studies on the seismic behaviors of the steel hollow bridge piers (Goto et al. (2015)), Goto et al. (2014, 2017) studied the seismic performance of circular CFT bridge piers using a large-scale shake table. Firstly, shake table tests of single circular CFT columns were conducted to compare the seismic performance of steel hollow piers and CFT piers. The effect of bi-directional earthquake motion was investigated by the comparison of different input earthquake acceleration. Furthermore, these experimental results were used to examine the accuracy of their proposed advanced FEM analytical method of partially concrete infilled CFT columns.

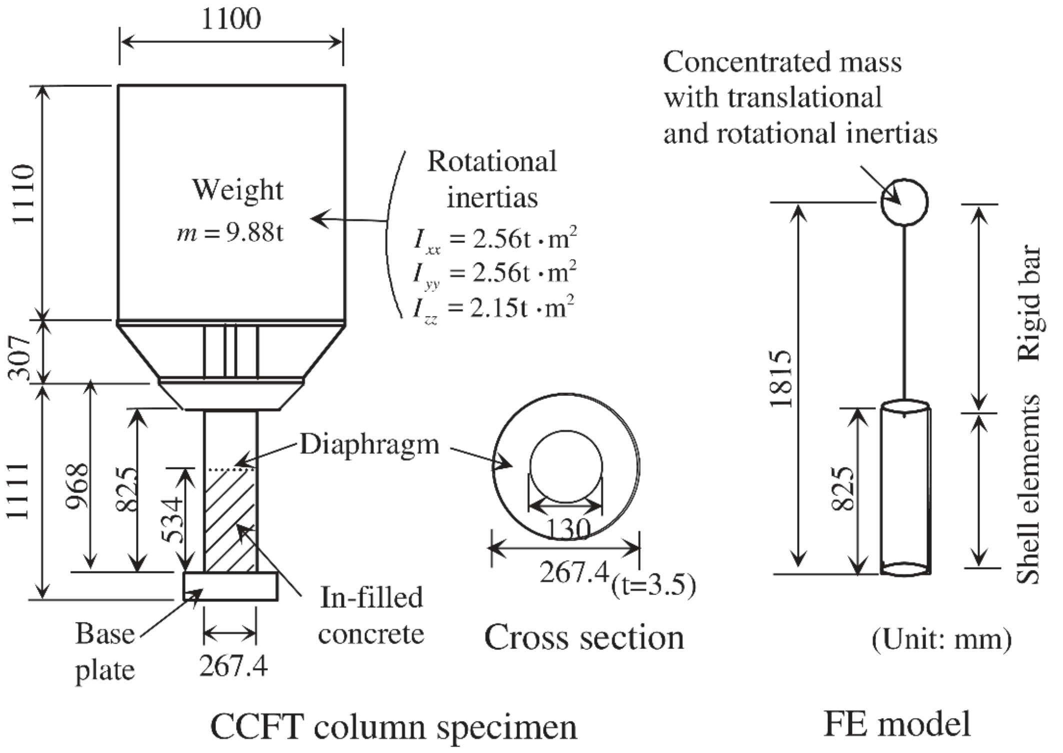

Fig. 2-27. Experimental specimen and FE model (Goto et al. (2014))

The details of their single column specimens are shown in Fig. 2-27. This specimen was designed with a scale factor of 1/8 by considering the capability of the shake table. A steel weight of 9.9 tons was installed at the top of the CFT column to simulate the gravity load of the superstructure of bridges. Concrete was infilled up to the height of the two times of the diameter of the column. The selected earthquake wave was the Tsugaru wave, which was observed at the Tsugaru bridge on the 1983 Nihonkai-Chubu earthquake (Goto et al. (2014)). For the comparison, the longitudinal and transverse components of Tsugaru waves were applied separately and simultaneously.

The experimental results of the time history curves of response displacement are shown in Fig. 2-28. Firstly, the comparison of the unidirectional shake table test shows that the hollow steel pier specimen collapsed during the test while the CFT pier specimen not. This gives a very persuasive proof of that the infilled concrete can upgrade the seismic performance of steel hollow piers to a great extent. Moreover, the experimental results of bi-directional shake table test show that the bridge piers may suffer from more severer damage due to the multidirectional seismic load. The observation from the direct experimental method shows a good consistency with those observed during the quasi-static cyclic load and the pseudo dynamic load test.

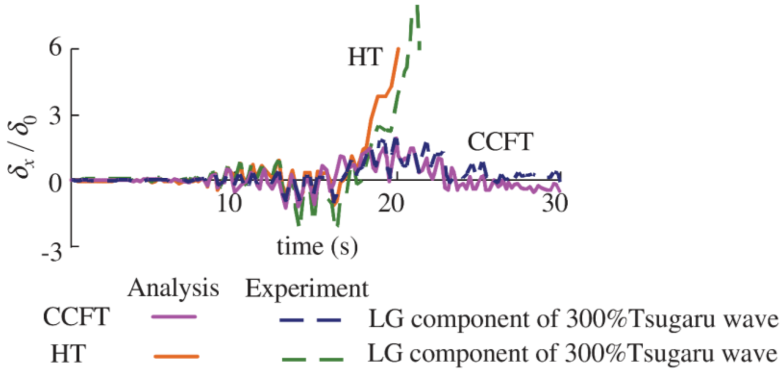

(a) uni-directional test results

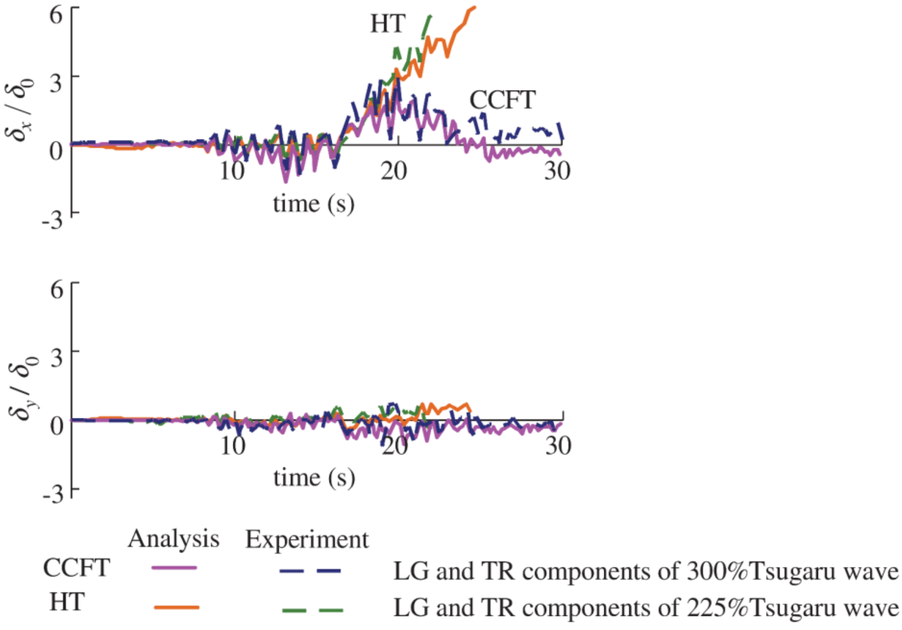

(b) bi-directional test results

Fig. 2-28. Time history curves of response displacement (Goto et al. (2014))

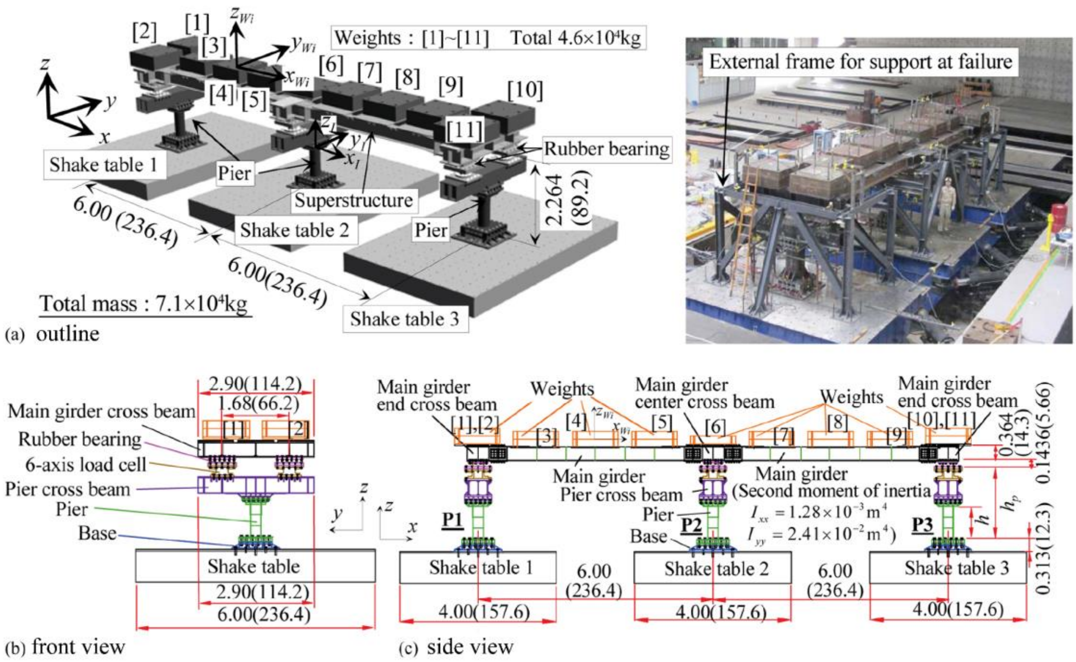

Fig. 2-29. Two span elevated girder bridge model used in the shake table test (Goto et al. (2017))

Up to the present, the seismic performance of independent CFT columns have been comprehensively investigated by many researchers with a simple or a complex experimental method. Some consensus has been reached by researchers on the failure mode, the upgraded strength and the ductility of CFT column severed as a cantilever column under earthquakes. However, how CFT columns behave in a structural system and if the interaction between different structural members change the seismic behavior of CFT columns or not is still not clear. Therefore, to observe the seismic behaviors of CFT members in an entire system, Goto et al. (2017) carried out by a large-scale shake table test of a two-span continuous elevated girder bridge supported by three CFT piers.

The bridge model used in the shake table test is shown in Fig. 2-29. The detail of this model and experimental results are explained in Chapter 5 and applied as a verification of the proposed numerical method. It should be mentioned here that up to the present, this is the only available large-scale shake test of bridge structure supported by CFT piers. To complete the seismic design system of the CFT structures, it is necessary to carry out more and more this type of experimental studies to verify and improve the existing seismic design method of CFT structures.

Chapter 3. Review of analytical modeling of the seismic behaviors of CFT columns

3.1 General

In the previous chapter, the experimental studies of seismic behaviors of cantilever CFT columns were categorized and discussed. Based on the experimental results, the collapse mode, strength, ductility and energy dissipation capacity of cantilever CFT columns have been comprehensively investigated and some empirical summary and design equations were proposed by many researchers. However, the detailed mechanism of CFT columns under the seismic load is still not clear. How the steel and concrete behave and their interaction on the contact surface under the alternating loads are yet to be studied. To understand the performance observed in the CFT columns experiments, building a rational and accurate analytical model is of great importance.

Moreover, to build a complete design method of CFT columns, with all the available materials, any possible cross-sectional types and dimensions, more and more experimental studies are required. However, experimental studies are costly and time consuming. Furthermore, real sized specimens can hardly be tested due to the limitation of the capacity of test apparatus. Thus, a reasonable analytical model is an ideal substitution for the supplement of the current experiment database for the design method. To develop a seismic theory, a more realistic earthquake scenario should be considered in the design of structures. But the practical earthquake motion is hard to be simulated in the experimental study including the multi-directional components. With an analytical model, it is possible to reproduce the realistic situation of structures under the earthquake and to investigate their performance.

Many researchers have proposed their own analytical model of CFT columns. These models have been applied to reproduce the results of accompanying experimental studies. In these works, the analytical model was used to reproduce some salient features of the experimental observation and the validity was proved by finding the correlation between test and computational results. This brings some problems in the application of the current analytical models. Firstly, since the purpose of developing those models is to illustrate the experimental behaviors with the certain test apparatus and specially designed specimens, consequently the applicability of those models is limited as such. Most of the simple models (fiber model) were designed with a certain failure mechanism according to the experimental observation. However the versatility of them could not be ensured due to lack of the validation against wide-range of experimental results. Secondly, the constitutive relations used for representing the materials in the structures is not applicable to a wide range of CFT columns.

Up to the present, most constitutive relations used in the analytical models of CFT columns were refer to those of hollow steel columns and reinforced concrete. By some material tests, for example, a tensile coupon test and a concrete compression test, the parameters of the material skeleton curves were calibrated. But this kind of calibration is insufficient, especially for the hysteretic behavior of materials. To overcome the limitation of those relatively simple models, complicated modeling method with shell and solid element is becoming popular among researchers. With the logic of geometry, it is time-consuming but not too hard to build this kind of solid models of CFT columns by the reasonable arrangement of nodes and elements. However, the presence of tens of thousands of elements makes the computational cost huge. Furthermore, a rational simulation of the gap relation between different materials is necessary and thus, led to a more unstable calculation condition due to the discontinuity in the modeling.

In this chapter, the current analytical models of CFT columns are discussed and introduced, by comparing their numerical effectiveness, applicability and accuracy. For easy understanding, the discussed models were categorized into two groups according to their modeling method. That is the ‘Fiber based model’ and ‘Shell-solid based model’.

3.2 Fiber based model

During the past three decades, many researchers have developed analytical models to investigate the mechanical behaviors of CFT columns using fiber elements. In general, the key features of employing this kind of models are: reasonable cross-sectional discretization according to the geometric characters, rational uni-axial stress-strain relations of fiber elements accounting for the material behaviors of steel and concrete, logical modeling technique of the collapse of the columns and the interaction between different materials based on the experimental observation. These features are discussed sequentially in the following sections. The application of those fiber based analytical models usually complies with some basic assumptions, including: a) plane section remain plane and perpendicular to the centroid axis before and after bending; b) slip between concrete and steel is not considered; c) inelastic shear deformation is not considered; d) creep and shrinkage of infilled concrete is not considered; e) residual stress formed in the steel is not considered; f) local buckling of steel is not considered. The existing fiber-based models of CFT columns complies with one or some above mentioned assumptions for the simplicity.

3.2.1 Cross-section discretization

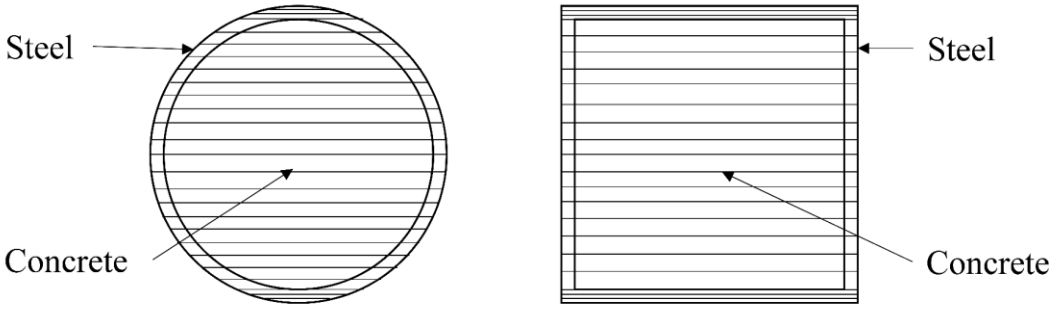

Fig. 3-1. Cross-section discretization of modeling of uniaxial behaviors

In the fiber-based modeling approach, the CFT columns is modeled by one or several beam-column elements connected at each end by nodes. In each element, a slice is set at the mid or the end of the element to account for the cross-sectional behaviors of the columns. For the uniaxial modeling, the slice is divided in to some discrete fibers (layers), as shown in Fig. 3-1. It should be noted here that at the displacement direction of steel tube section, the steel is usually divided into thinner layers to ensure the accuracy of the analysis. This kind of cross-section discretization was adopted by many researchers, including Chung (2010); Chung et al. (2007); Gayathri et al. (2004a, 2004b); Ishizawa and Iura (2006); Ge et al. (2003); Susantha et al. (2002); Varma et al. (2002, 2005); Aval et al. (2002) and Zubydan and ElSabbagh (2011). For each fiber of the cross section, three basic attributes are assigned. These are: the area of fiber; the distance from the fiber center to the centroid of cross-section; the uniaxial stress-strain relation of material (discussed in the following section). With these assumptions, firstly, by integrating the fiber stress-strain response over the cross -section, the slice force-deformation relation can be obtained. Then, according to the assumption of the slice response over the entire element (Varma et al. (2002, 2005)) remains constant over the element) the element force-displacement response can be calculated.

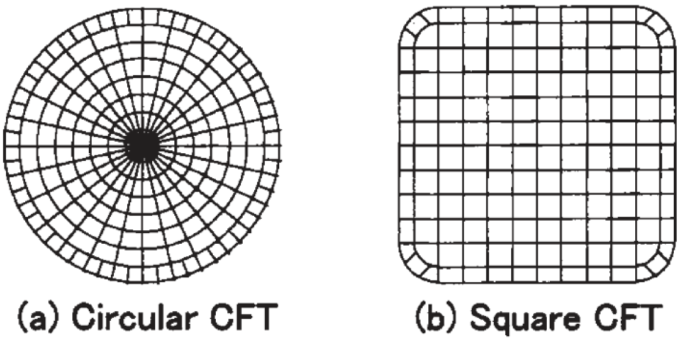

Fig. 3-2. Cross-section discretization of modeling of biaxial behaviors (Inai et al. (2004))

In another case, for simulating the biaxial load condition, another discretization method should be used, as shown in Fig. 3-2. Normally, the CFT columns with rectangular cross-section will be divided into uniform grids with the same area. A circular CFT cross-section will be discrete into a radial form of grids. This is similar to the application of the normal beam element with specific integration points. According to some related researches (Kostic and Filippou 2012), the precision of division of fibers will affects the effectiveness of calculation and accuracy to a large extent. Therefore, it is essential to decide a relatively coarse cross-section discretization for the balance of the cost and accuracy. In the literature, some researchers applied this kind of cross-section discretization, including: Inai et al. (2004); Hu et al. (2010); Valipour and Foster (2010); Wu et al. (2012); Patel et al. (2014); Wang et al. (2014); Yadav et al. (2017); Qiang et al. (2018); Stephens et al. (2018) and Wang et al. (2019).

A cross-section discretization method of fiber-based modeling approach of CFT columns is introduced in this section. In the fiber modeling approach, the nonlinear behaviors of materials are considered by the uniaxial constitutive relation of each fibers. The CFT cross-section behaviors is then calculated by integration over all the fibers. However, it is also important to employ the cross-section response to calculate the column behaviors, which associates with the arrangement of elements and nodes, as illustrated in the next section.

3.2.2 Modeling of the CFT columns

To simulate the load-deflection behaviors of a CFT member, one or several frame elements are usually used for the simplicity (e.g. (Valipour and Foster 2010; Zubydan and ElSabbagh 2011)). These elements are linearly connected by nodes and share the same material constitutive relations and cross-section discretization across the column length. The conventional application of this type of method is to analyze the performance of CFT members in a frame structure with CFT columns and steel beams.

However, although the accuracy and efficiency of this method is acceptable for the engineering application on the analysis of overall behaviors of system or the entire columns (e.g. the reactional force of the column base or the response displacement of column top), it cannot be used for the investigation of the detailed behaviors of column itself, such as the interaction between steel tube and infilled concrete and local buckling behavior of the specified location.

In this study, the cantilever partially or fully infilled CFT columns are investigated. Unlike frame analyses, relatively detailed modeling of the column performance under the loading condition is required, including the load-deflection along the height of the column. The following refined finite element mesh method shown in Fig.3-3 is thus applied by many researchers, (Gayathri et al. (2004b); Susantha et al. (2002); Varma et al. (2002)) among others.

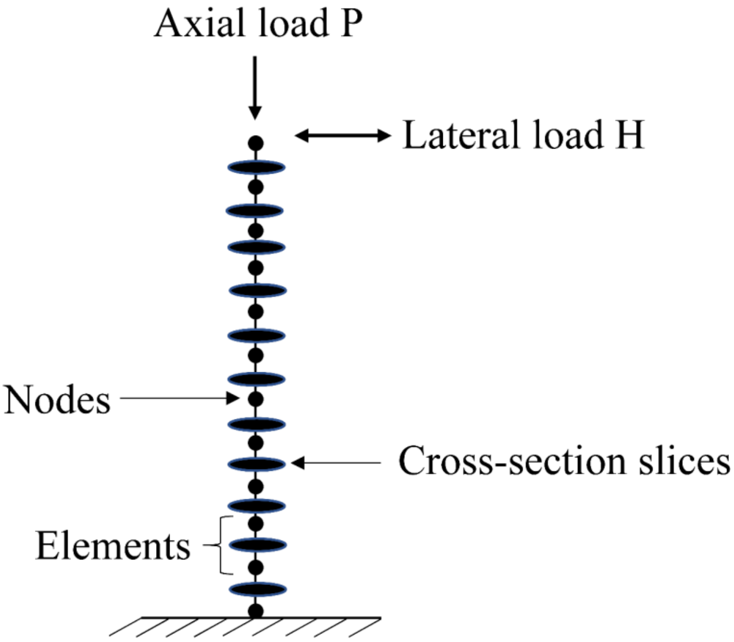

Fig. 3-3. Modeling of CFT columns

As shown in Fig. 3-3, a CFT column is divided into suitable numbers of elements along the column length, with a slice at the mid of each element. The load is assumed to be applied at the nodal points. During the computation, each element is characterized by some stiffness obtained from the cross-sectional analysis based on the cross-section discretization illustrated in the previous section. Material nonlinearity is expressed implicitly by the stress-strain relation of fibers. According to the stiffness obtained from cross-section analysis, the element stiffness matrices can be derived in terms of the nodal degree of freedom. Then, by transforming the local coordinates system of each element to the global coordinates system and imposing the condition of the compatibility at node points, the structural stiffness matrix can be formulated. The load path is usually divided into several equilibrium configurations. The structural behaviors of the CFT columns are usually calculated by the iteration of each load step. Shown in Fig. 3-4 is the procedure of fiber based CFT column analysis proposed by Gayathri et al. (2004b). This process can be applied in an in-house program, or general analytical software including Abaqus 6.14 (Simulia 2014) or OpenSees (OpenSees 2006) among others.

The aforementioned modeling method is so-called ‘distributed-plasticity’ models of the CFT columns. However, there are some problems in the application of this kind of modeling method. Firstly; the number of longitudinal elements will affect the solution. Therefore, before calculation, a convergence check of the solution should be conducted to find a suitable element mesh. If softening behaviors is considered in the stress-strain relation of materials, unstable moment may occur at the column base

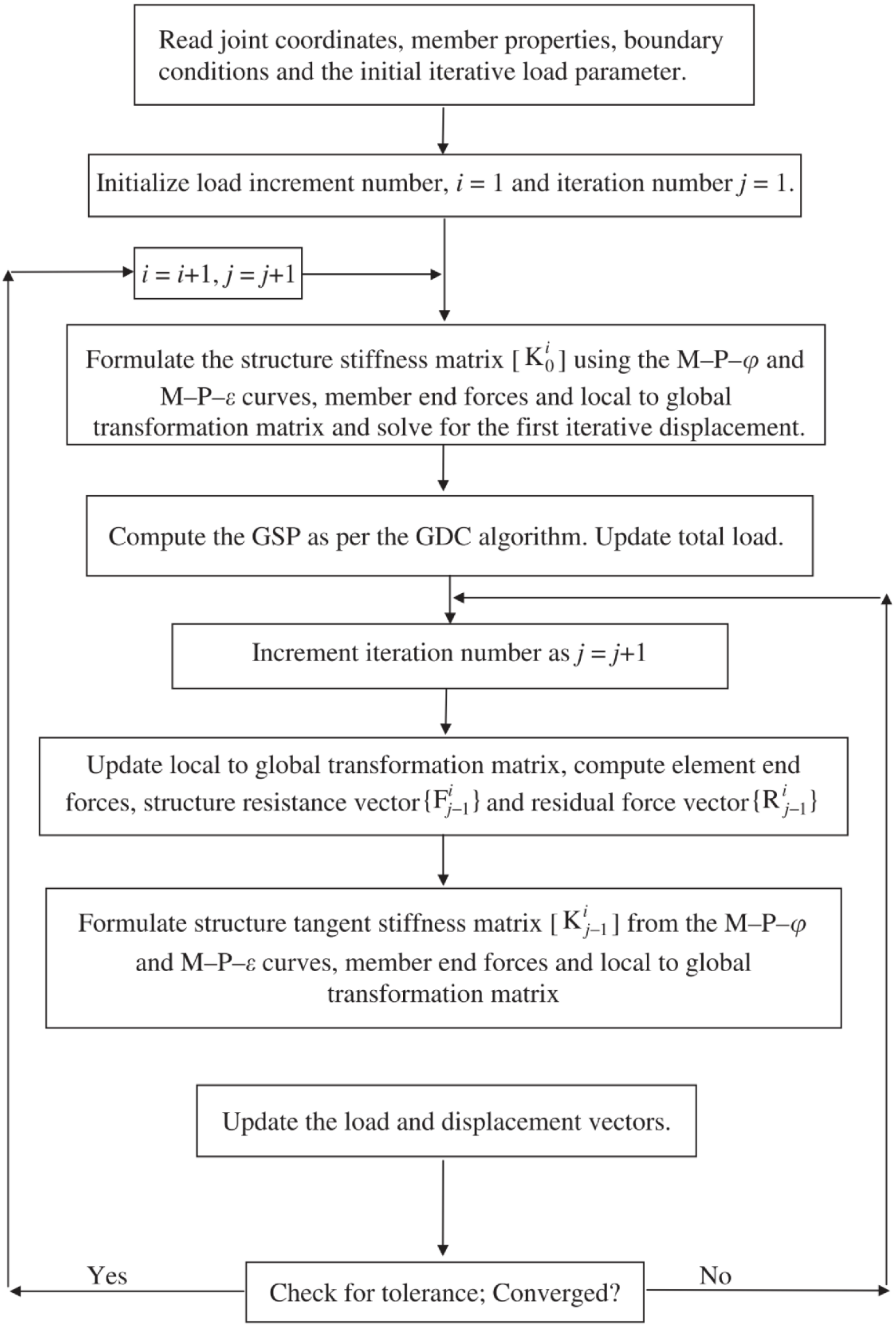

Fig. 3-4. Example of the flow chart of fiber-based analysis of CFT columns (Gayathri et al. (2004b))

element. This phenomenon has been checked by Susantha et al. (2002). According to their study, this problem will be more obvious in CFT columns with thin-walled steel tube and appropriate material constitutive relation should be adopted.

Based on the experimental behaviors of cantilever CFT columns discussed in the Chapter 2, the failure mode can be summarized as the local buckling of column base. The upper part of the local buckling region can be assumed to deform elastically. Thus, a concentrated plasticity modeling method can be used to fit the practical phenomenon in the test and prevent the local instability caused by the material softening in many elements.

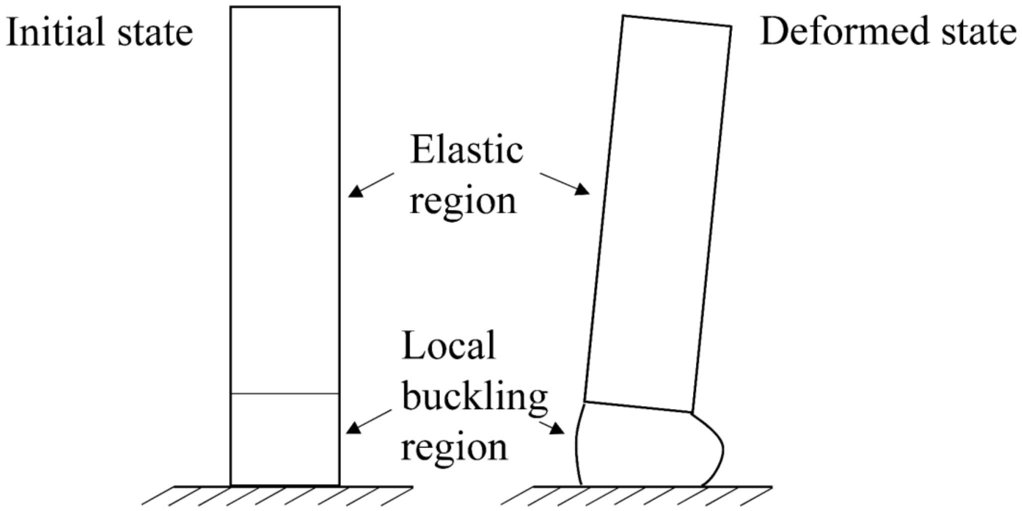

Fig. 3-5. Concentrated plasticity modeling of the CFT columns

The concentrated plasticity modeling of CFT columns are shown in Fig. 3-5. This kind of modeling method are adopted by Inai et al. (2004), Stephens et al. (2018) among others. There are several methods to simulate the local buckling region: using special material constitutive relation; a rotational spring element; a zero-length hinge element. However, whatever modeling method is adopted for a plastic region, it is important to determine an appropriate size of the local buckling range. Some recommended values are introduced here.

Susantha et al. (2002) proposed an effective length of the minimum value of 0.7 times b (b is the flange width of the cross section) and the span length between two internal diaphragms. This value was examined to coincide well with the experimental observation of the partially infilled rectangular CFT columns. Varma et al. (2005) suggested that to adopt the length of B (B is the width of square CFT cross section) to simulate the local buckling segment in the square CFT columns. It should be noted here that Varma's model is primarily applied for CFT columns with high-strength material. Inai et al. (2004) and Denavit (2015) also suggested that to use the column depth or diameter to divide the elastic and inelastic part of the CFT column models. Ishizawa and Iura (2006) proposed an equation to calculate the plastic hinge region based on the geometric and material parameters:

$$L_b = 0.275\sqrt{\frac{I_s}{A_s}}\left\{\frac{D}{t}\frac{D}{h}\left(\frac{f_y}{E_s}\right)^{0.5} n_j^{-0.5}\right\}^{-0.596} \tag{3-1}$$

$$n_j = 1 - \frac{P}{A_s f_y} \tag{3-2}$$

Where L_b is the length of the plastic hinge region; I_s and A_s are the moment of inertia and cross sectional area of hollow steel tube respectively; D, t and h are the diameter, steel tube thickness and length of column; f_y and E_s are the yield stress and Young's module of steel. n_j is the parameter considering the effect of axial force and P is axial force applied on the top of the column. This is an empirical equation to calculate the buckling region based on the experimental observation of tests on hollow steel columns.

Chung (2010) and Chung et al. (2007) adopted refined element mesh to simulate the local buckling region. In their analytical model, for rectangular CFT columns, an analytical wave length of plastic local buckling along the column length $0.8B$ is used (Yamada et al. (1993)). For circular CFT columns, the wave length is calculated by (Yasui 2001):

$$L_b = 1.25t\sqrt{\frac{D}{t}-1} \tag{3-3}$$

In the study of Stephens (Stephens et al. (2018)), the buckled region of steel tube is assumed to be constant of 51mm based on the experimental observation (Stephens et al. (2016a)) for CFT columns of $80 < D/t < 100$.

3.2.2 Constitutive relation of infilled concrete fibers

There are variety of constitutive relations available in the literatures for the modeling of the infilled concrete. The basic shape of initial backbone curve of different constitutive relation is similar, generally formulated by three sections including an ascending part; a descending region and a constant residual stress part, like shown in Fig. 3-6. The existing model proposed by researchers are generally based on the modification of those typical curve shapes. The difference between those models are their definition of the value of confined peak strength; strength reduction modules, residual strength etc. These values are affected by the confinement effect of steel tube, which is different according to cross section type and different $D/t\,(B/t)$ ratio. The cyclic rule is also important to consider the cyclic stiffness reduction caused by cracking and crushing. To take an overall understanding of these models, their basic formulation and their application are reviewed herein.

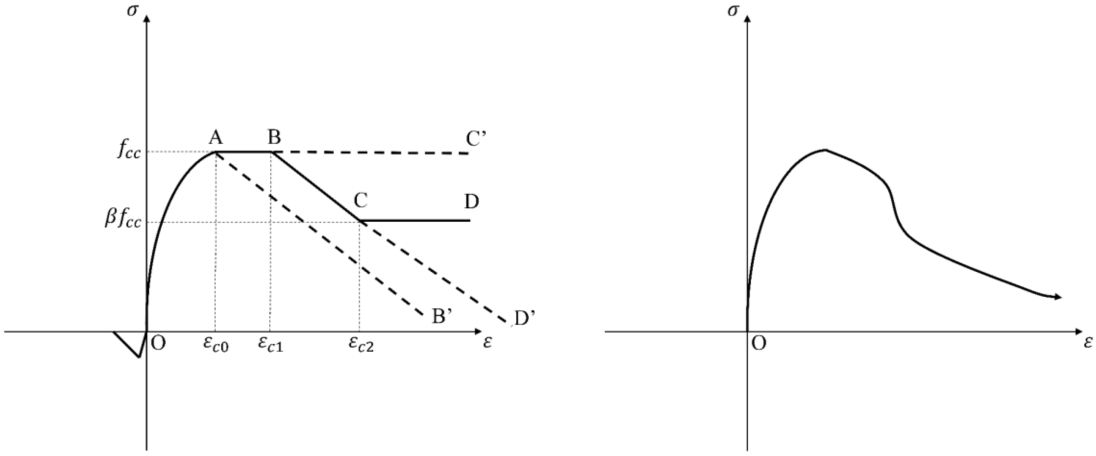

(a) type 1 (b) type 2

Fig. 3-6. Typical form of constitutive relation for the infilled concrete

- Shams and Saadeghvaziri' model of infilled concrete

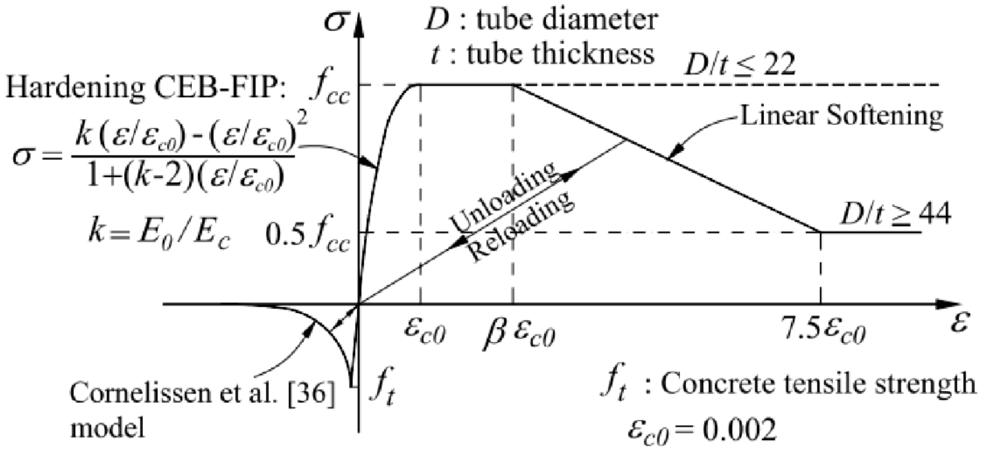

Fig. 3-7. Constitutive relation of infilled concrete proposed by Shams and Saadeghvaziri (1999)

The constitutive model proposed by Shams and Saadeghvaziri (1999) is shown in Fig. 3-7. The shape of this stress-strain relation corresponds to the O-A-B-C-D type curve shown in Fig. 3-6 (a). This model is applicable for the analysis of both circular and rectangular CFT columns. This is model are adopted by CFT models presented by Aval et al. (2002) and Valipour and Foster (2010). The confined compressive strength f_{cc} is defined as:

$$f_{cc} = f_{cp}(1+\frac{A}{1+\left(\frac{D/t}{B}\right)^{\alpha}}) \tag{3-4}$$

Where f_{cp} is the compressive strength of concrete; For circular section: $\alpha=1$; $A=1.831e^{-\left(\frac{f_{cp}}{24.4}\right)}$ and $B=-32.52+3520/f_{cp}$; For rectangular section: $\alpha=4$; $A=1.335e^{-\left(\frac{f_{cp}}{24.4}\right)}$ and $B=47.49+207/f_{cp}$. In the backbone curve shown in Fig. 3-6, ε_{c0} is assumed to be 0.002, β is assumed to be 2.5. The softening part is defined as linear connecting of the $2.5\varepsilon_{c0}$ to $7.5\varepsilon_{c0}$ for CFT columns with the D/t ratio greater than 44. While the residual strength is 0.5 f_{cc}. (Unit of concrete strength: MPa)

The governing rule of unloading and reloading curves is the total secant damage model for both compressive and tensile side, as shown in Fig. 3-7. To consider the effect of column size, a reduction factor is introduced as:

$$\gamma_u = 1.67D^{-0.112} \leq 1.0 \tag{3-5}$$

(unit of diameter: mm)

In this constitutive relation, the softening behaviors both in the compressive side and tensile side are taken into account so that numerical localization may occur during the calculation. To avoid this problem, the objectivity of the results should be restored by applying localization limiter (Valipour and Foster 2010).

- Mander's model of part O-A (Mander et al. (1988)) and its modifications

The most common used constitutive relations have the shape of backbone curve shown in Fig. 3-6 (a). Whatever the post-peak behaviors like in various models, the O-A part which represents the strength of confined concrete is similar. To simulate this ascending part, Mander's model is the most applied one, which has been adopted by Gayathri et al. (2004a); Patel et al. (2014); Qiang et al. (2018); Susantha et al. (2002); Ishizawa and Iura (2006); Tort and Hajjar (2010); Zubydan and ElSabbagh (2011); among others. The basic equations of Mander's model is explained here:

$$\sigma_c = \left[f_{cc} \lambda \left(\varepsilon_c / \varepsilon_{c0} \right) \right] / \left[\lambda - 1 + \left(\varepsilon_c / \varepsilon_{c0} \right)^{\lambda} \right] \tag{3-6}$$

$$\lambda = E_c / \left[E_c - \left(f_{cc} / \varepsilon_{c0} \right) \right] \tag{3-7}$$

where σ_c and ε_c is the stress and strain of infilled concrete. E_c is the Young's modules of the infilled concrete. The calculation of the compressive strength of confined concrete f_{cc} is usually by multiplying a reduction factor which associated to the size of the cross section. Eq. (3-5) is a method to take the reduction factor. This method also adopted by Zubydan and ElSabbagh (2011). Patel et al. (2014) suggested a reduction factor for a rectangular CFT column:

$$0.85 \le \gamma_u = 1.85D^{-0.135} \le 1.0 \tag{3-8}$$

(unit of diameter: mm)

Where D is the diameter of inner concrete cross section.

To consider the effect of the thickness and strength of the steel tube, Susantha et al. (2002) and Gayathri et al. (2004a) employed an equation to calculate f_{cc}:

$$f_{cc} = 0.85 f_c + 4.0 f_{rp} \tag{3-9}$$

$$f_{rp} = -6.5R\left(f_{cp}{}^{1.46} / f_y \right) + 0.12 f_{cp}{}^{1.03} \tag{3-10}$$

$$R = \left(b/t\right)\sqrt{\left[12\left(1-\nu^2\right)\right]/4\pi^2}\sqrt{f_y/E_s} \tag{3-11}$$

(Unit of strength: MPa)

R is the width to thickness ratio of rectangular CFT columns. f_y and E_s are the yield stress and Young's modules of steel. f_{rp} is the maximum average lateral pressure on the infilled concrete.

The definition of the strain corresponds to the compressive strength ε_{c0} can be defined as: (Unit of strength: MPa)

$$\varepsilon_{c0} = \begin{cases} 0.002 & \\ 0.002 - \left[\dfrac{f_{cc}-28}{5400}\right] & for \quad \begin{matrix} f_{cc} \le 28Mpa \\ 28Mpa \le f_{cc} \le 82Mpa \\ 82Mpa \le f_{cc} \end{matrix} \\ 0.003 & \end{cases} \tag{3-12}$$

For the part A-B-C-D, model proposed by Tomii and Sakino (1979) is usually applied, and can be described as:

$$\sigma_c = \begin{cases} f_{cc} & \varepsilon_{c0} \le \varepsilon_c \le \varepsilon_{c1} \\ f_{cc} - f_{cc}\left(1-\beta_c\right)\dfrac{\varepsilon_c - \varepsilon_{c1}}{\varepsilon_{c2} - \varepsilon_{c1}} \quad \text{for} & \varepsilon_{c1} \le \varepsilon_c \le \varepsilon_{c2} \\ \beta_c f_{cc} & \varepsilon_c \ge \varepsilon_{c2} \end{cases} \tag{3-13}$$

$$\beta_c = \begin{cases} 1.0 & \left(\dfrac{B}{t}\right) \le 24 \\ 1.5 - \left(\dfrac{1}{48}\right)\left(\dfrac{B}{t}\right) \quad \text{for} & 24 \le \left(\dfrac{B}{t}\right) \le 48 \\ 0.5 & \left(\dfrac{B}{t}\right) \ge 48 \end{cases} \tag{3-14}$$

The constitutive model following the locus of O-A-B-C-D introduced above was adopted by many researchers. The value of ε_{c1} can be assumed as 1.5 times of ε_{c0}. The value of ε_{c2} can be defined as 0.015.

Some other modification of Mander’s model follows the locus of O-A-B’ or O-A-B-D’ are shown in Fig. 3-8 and can be refer to (Susantha et al. (2002); Tort and Hajjar 2010).

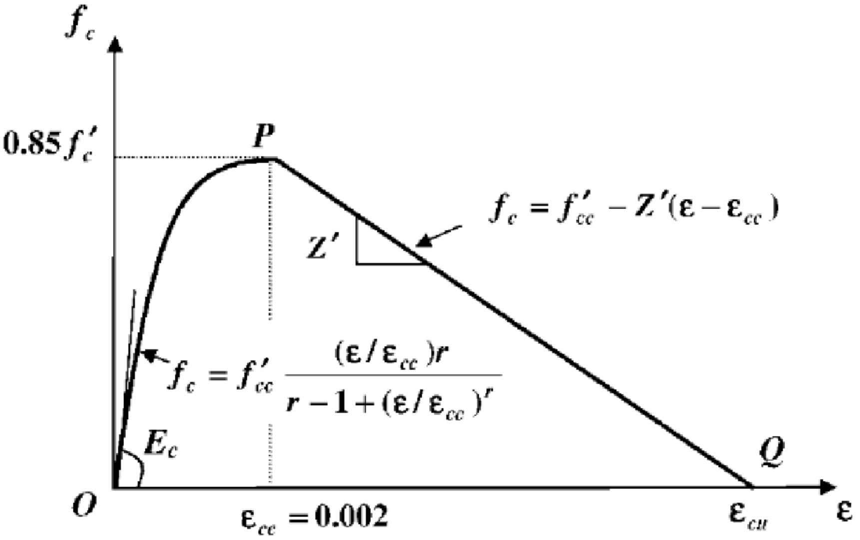

(a) Constitutive relation proposed by Susantha et al. (2002)

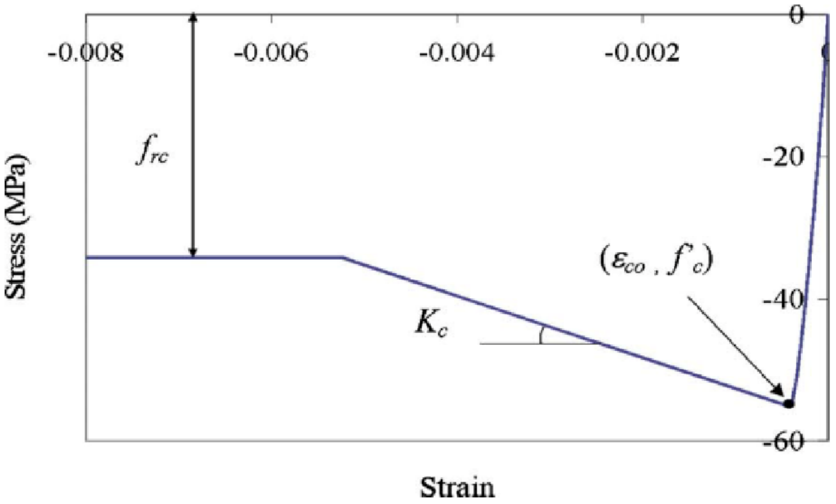

(b) Constitutive relation proposed by Tort and Hajjar (2010)

Fig. 3-8. Some application of Mander's model

- Nakahara's model of infilled concrete and its modifications

Another popular constitutive model of infilled concrete is a model proposed by Nakahara et al. (2003), follows with the locus shown in Fig. 3-6 (b). this model is adopted by Chung (2010); Chung et al. (2007); Inai et al. (2004); Wang et al. (2019); Wu et al. (2012); among others. The backbone curve of this model with the hysteretic rule takes the effect of crack opening and closing in an approximate manner is shown in Fig. 3-8. The basic equations of this model for the rectangular CFT columns are:

$$\mathrm{Y} = \frac{VX + (W-1)X^2}{1 + (V-2)X + WX^2} \tag{3-15}$$

$$\mathrm{Y} = \frac{\sigma_c}{f_{cp}} \tag{3-16}$$

$$\mathrm{X} = \frac{\varepsilon_c}{\varepsilon_{c0}} \tag{3-17}$$

$$\mathrm{V} = \frac{E_c \varepsilon_{c0}}{f_c} \tag{3-18}$$

$$\mathrm{W} = 1.50 - 17.1 \times 10^{-3} f_c + 2.39\sqrt{f_{cc}} \tag{3-19}$$

$$E_c = \left(6.90 + 3.32\sqrt{f_{cp}}\right) \times 10^3 \tag{3-20}$$

$$f_{cc} = \frac{2t^2 \left(B - t\right) f_{sy}}{\left(B - 2t\right)^3} \tag{3-21}$$

$$\varepsilon_{c0} = 0.94\left(f_c\right)^{1/4} \times 10^{-3} \tag{3-22}$$

Where f_{sy} is the yield stress of steel.

For the circular CFT columns, the Eq. (3-15) should be modified as:

$$\sigma_c = \frac{V + \left(W - 1\right)}{1 + \left(V - 2\right) + W} f_{cb} \tag{3-23}$$

$$\mathrm{V} = \frac{E_c \varepsilon_{c0}}{f_{cb}} \tag{3-24}$$

$$f_{cc} = \left(\frac{4.1}{23}\right) \times \frac{0.38 t f_{sy}}{\left(D - 2t\right)} \tag{3-25}$$

$$f_{cb} = \left(1 + 4.1 \frac{0.38 t f_{sy}}{\left(D - 2t\right) f_{cp}}\right) f_{cp} \tag{3-26}$$

(Unit of length: mm; Unit of strength: MPa)

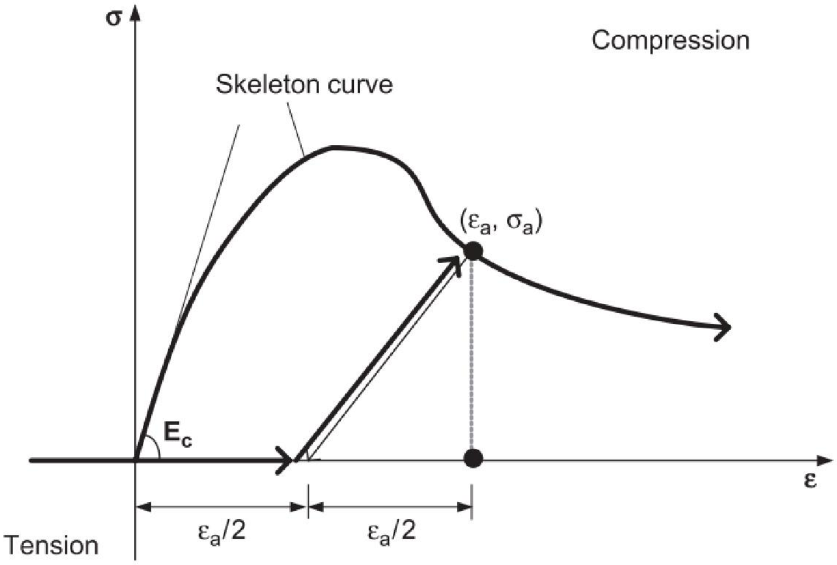

Fig. 3-9. Constitutive relation of infilled concrete proposed by Nakahara et al. (2003)

- Han’s model of infilled concrete and its modifications (Han et al. 2003)

The constitutive relation proposed by Han et al. (2003) is introduced herein, as shown in Fig.3-10. This model is adopted by Han et al. (2003) and Wang et al. (2014); among others.

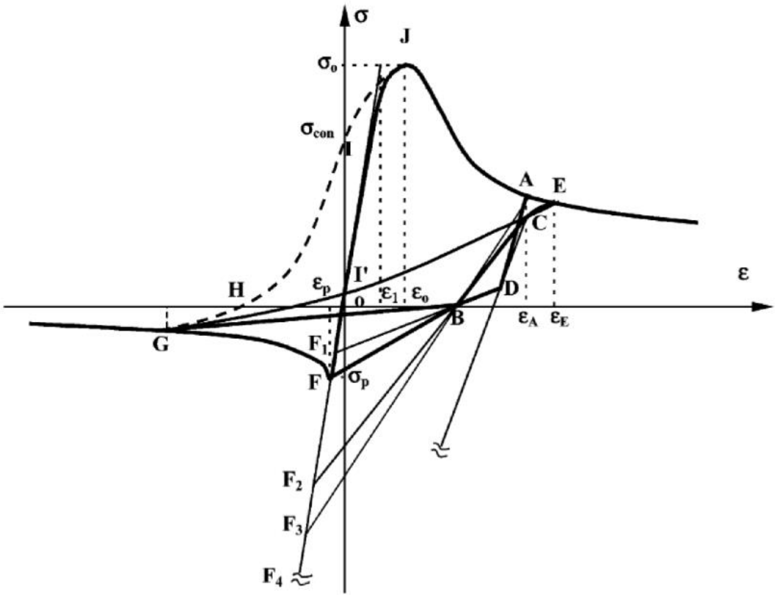

Fig. 3-10. Constitutive relation of infilled concrete proposed by Han et al. (2003)

The skeleton curve of stress-strain relation can be expressed as:

$$\mathrm{y} = \mathrm{Ax} - \mathrm{B}x^2 \qquad (x \le 1) \tag{3-27}$$

$$\mathrm{y} = \frac{\mathrm{x}}{\beta x^{\eta} + x} \qquad (x > 1) \tag{3-28}$$

In which $\mathrm{y} = \sigma_c / \sigma_{c0}$ and $\mathrm{x} = \varepsilon_c / \varepsilon_{c0}$.

$$\sigma_{c0} = f_{ck}\left[1.194 + 0.25(13/f_{ck})^{0.45}\left(-0.07845\xi^2 + 0.5789\xi\right)\right] \tag{3-29}$$

$$\varepsilon_{c0} = \varepsilon_{cc} + 0.95\left[1400 + 800\left(\frac{f_{ck} - 20}{20}\right)\right]\xi^{0.2} \tag{3-30}$$

(unit of concrete strength: N/mm^2)

Where $\varepsilon_{cc} = 1300 + 14.93 f_{ck}$; $\eta = 1.60 + 1.5\left(\frac{\varepsilon_{c0}}{\varepsilon}\right)$; $\mathrm{A} = 2.0 - \mathrm{k}$; $\mathrm{B} = 1.0 - \mathrm{k}$. and $\mathrm{k} = 0.1\xi^{0.745}$; $\beta = \left(0.75 f_{ck}{}^{0.1}\right) / \sqrt{1+\xi}$.

For the governing rule of the hysteretic behaviors, please refer to Han et al. (2003).

3.2.3 Constitutive relation of steel fibers

Many stress-strain relations have been proposed. To consider different effects of mechanical behaviors of steel, various characters will reflect in the skeleton curve. For example, to consider the effect of residual stress formed in the cold form procedure, the existence of yield plateau can be determined. According to the accuracy required by users, the softening behaviors caused by local buckling should be decided if it appears in the relation. The way of their modeling in elastic range, strain hardening range and hardening rule are also different. Some most common used stress-strain relation of steel tube available in the literatures are selected and introduced herein.

A widely accepted constitutive relation of structural steel among researchers is the one proposed by Menengotto (1973). With some modifications, this model was adopted in many analytical modeling of CFT columns (Valipour and Foster 2010; Zubydan and ElSabbagh 2011) among others. In Aval's analytical model (Aval et al. (2002)), the elastic and yield asymptotes are assumed to be straight lines. The position of the limiting asymptotes corresponding to the yield surface is assumed to be fixed at all times. The unloading slope remains constant and equal to the initial slope. The effect of the aspect ratio and length width ratio on the maximum stresses and stress decrease is considered. In Valipour' study (Valipour and Foster 2010), the effect of local buckling is taken into account in an implicit manner by multiplying the yield stress of steel with the slenderness dependent reduction factors, defined as:

$$R_1 = 1.08 - 0.045\ln\left(D/t\right) \tag{3-31}$$

$$R_2 = 0.60 + \frac{0.38}{1+\left(\frac{L/D}{22.2}\right)^{3.9}} \tag{3-32}$$

$$f_y = R_1 R_2 f_y \tag{3-33}$$

This formulation of adjusting the local buckling behaviors of steel based on the slenderness ratio of the plate is proposed by Shams and Saadeghvaziri (1999).

The constitutive relation with a hysteretic rule proposed by Chung et al. (2007) is shown in Fig.3-11. This model is adopted by Chung (2010); Chung et al. (2007); Wang et al. (2019); among others. In this model, the backbone curve of tensile side is assumed to be as same as the compressive side as shown in Fig. 3-11. As show in these figures, in the model, the yield plateau is considered. The point A corresponds to the threshold point of the softening behaviors due to the effect of local buckling. In the softening region, two stage of different slopes are adopted. This is because of the strength of steel tube is stabilized by the restraining effect of concrete.

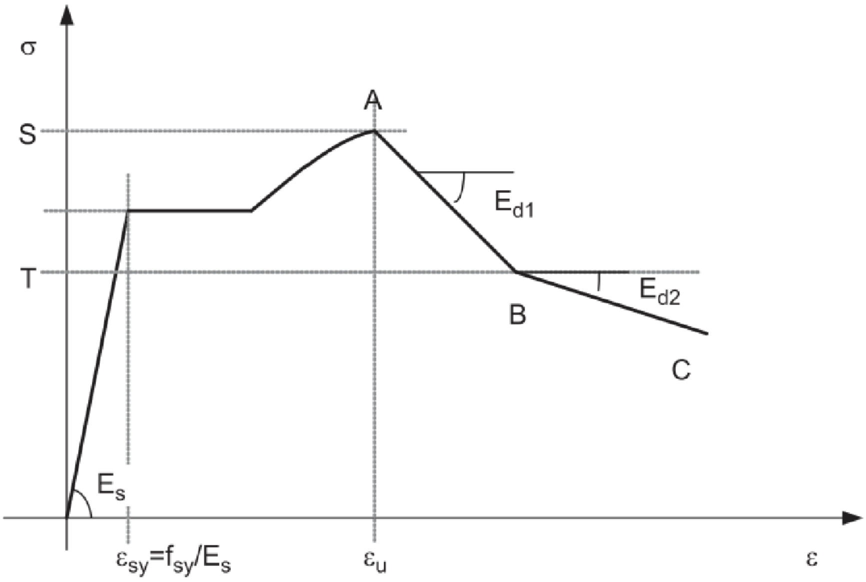

Fig. 3-11. Constitutive relation of steel tube proposed by Chung et al. (2007)

To consider the effect of elastic local buckling, a slenderness parameter is defined as:

$$\varphi = 0.6\varepsilon_{sy}\left(B/t\right)^2 \tag{3-34}$$

where the ε_{sy} is the yield strain of steel, B and t is the width and thickness of cross-section respectively. Then, the strain corresponds to the local buckling ε_u is defined as:

$$\varepsilon_u = \varepsilon_{sy}\left(\frac{8.7}{\varphi} - 1.20\right) \tag{3-35}$$

The stress of point B is calculated by:

$$\mathrm{T} = \mathrm{S}\left(-0.079\varphi + 0.81\right) \tag{3-36}$$

Where S is the peak stress of steel tube. The descending modulus after the peak point A is defined as:

$$E_{d1} = E_s\left(-0.014\varphi^2 - 0.005\right) \tag{3-37}$$

$$E_{d2} = \begin{cases} -0.005E_s & \sigma \geq 0.5S \\ 0.0 & \sigma < 0.5S \end{cases} \tag{3-38}$$

The hysteretic rule considers strain-hardening, stiffness-softening due to the Bauschinger effect, as well as resistance deterioration due to local buckling failure.

Similar to the Chung' model, many researchers use a critical parameter to trigger the local buckling in the steel tube. This threshold value can be stress or strain. Tort and Hajjar (2010) selected a parameter of critical strain as:

$$\frac{\varepsilon_{lbf}}{\varepsilon_y} = 3.14 \times \left(\left(\frac{D}{t}\right)\sqrt{\frac{f_y}{E_s}}\right)^{-1.48} \tag{3-39}$$

This is another form to consider the local buckling of the steel tube on the uniaxial stress-strain relation of steel fibers.

Varma's model (Varma et al. (2002)) of constitutive relation of steel fibers is shown in Fig. 3-12.

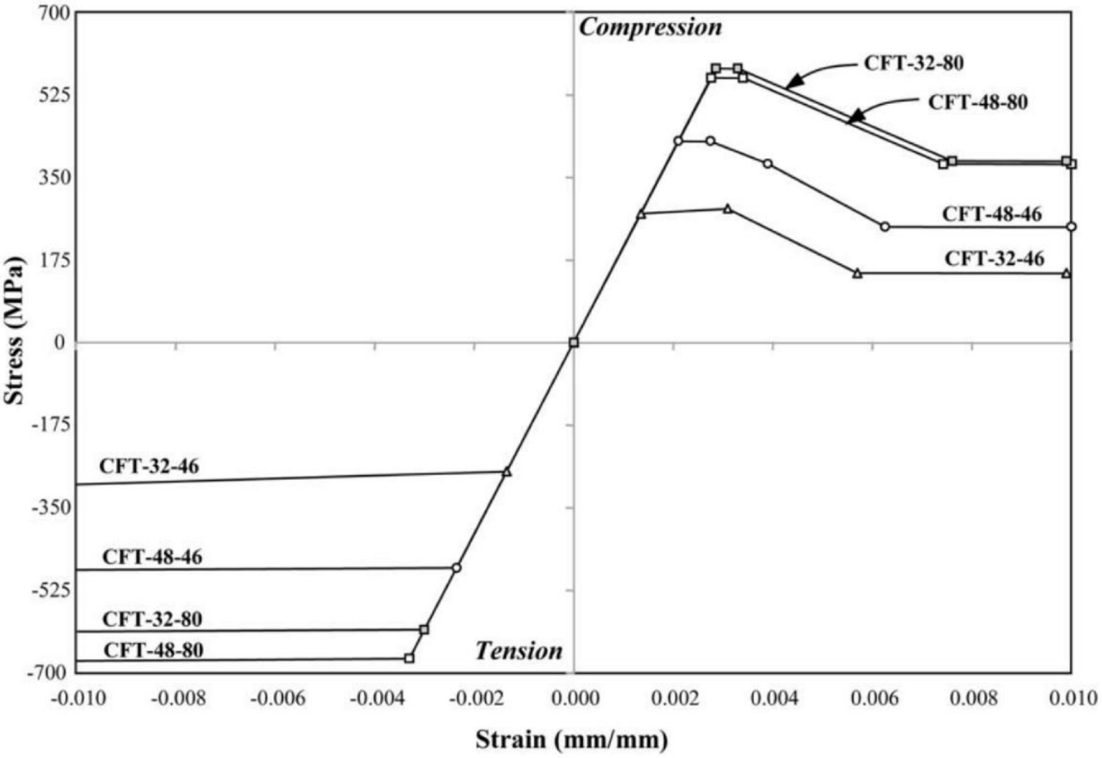

Fig. 3-12. Constitutive relation of steel tube proposed by Varma et al. (2002)

From the figure, the tensile side of the backbone curve is a bilinear model. On the compressive side, the effect of local buckling and the restraining of infilled concrete are considered. Unlike other models which are empirically calibrated by the experimental results, this model is calibrated based on an analytical method using 3D finite element model. This numerical calibrating method enables this model to cover a wide range of material and geometric parameters.

In many analytical models of CFT columns, relatively simple constitutive relations were adopted Han et al. (2003); Patel et al. (2014); Wang et al. (2014). Both in the compressive and tensile side, the backbone curve is bilinear and the strength reduction due to the local buckling are not considered.

This constitutive relation was examined to have an acceptable accuracy of simulating the CFT columns with relatively thick steel wall. The model proposed by Ishizawa and Iura (2006) is an effective constitutive relation for the modeling of steel tube. This model is adopted by the presented study and will be introduced in the following chapter.

3.3 Shell-solid element based model

The performance-based design of structure requires that the detailed behaviors of structure should be captured in the design and analysis. The conventional fiber-based modeling method cannot simulate the behaviors of CFT columns in a direct manner. Thus, analytical model established by the shell and solid elements has been applied by researchers. The model proposed by Goto et al. (2010) is selected as the reference of calibration of presented numerical model. The detailed information of this model will be introduced in the next chapter. Some numerical analysis conducted by other researchers with the application of shell-solid element based model is explained as follows.

Usami and Ge (1998) conducted an analytical study of partially infilled rectangular CFT bridge piers by employing shell-solid element model. As shown in Fig.3-12, the steel tube is modeled by shell elements S4R (Simulia 2014) and the infilled concrete is simulated by solid elements. The part between the column base and the lowest diaphragm is fine meshed. The part that is assumed to be elastic is modeled by the beam element for the simplicity. The stiffeners on the steel plate were modeled separately. Based on this model, some parameters of modeling were discussed. The mesh division in the location where local buckling occurs was found to have a great influence on the results. Meanwhile, the material model of 2SM (2 surface model) (Shen et al 1992) proposed by them was verified to have a good accuracy for the analysis of cyclic load condition. This model was performed on the software of ABAQUS (Simulia 2014).

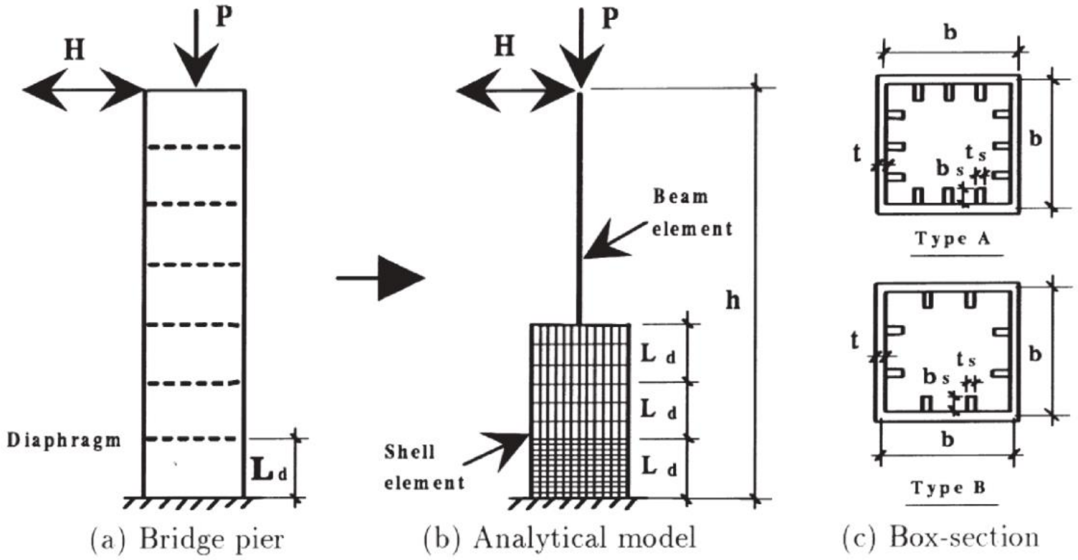

Fig. 3-13. Shell solid model of RCFT bridge piers proposed by Usami and Ge (1998)

Skalomenos et al. (2014) conducted an analytical study on the establishment of appropriate hysteretic model based on the shell-solid element analysis of CFT columns. This study was performed on the software of ATENA. In their model, 20 nodes shell element was adopted for the steel and 8 nodes solid element for the infilled concrete.

The interface action between concrete and steel was modeled, by the 8 nodes interface element. Three hysteretic models investigated in the study were: Bouc-wen model (Constantinou and Tadjbakhsh 1985); Ramberg-Osgood model (Ramberg and Osgood 1943) and AI-Bermani model (Ai-Bermani et al. (1994)). Based on the accurate shell-solid element analysis, the proposed concentrated plasticity hysteretic model was calibrated, and their accuracy were verified.

Serras et al. (2016, 2017) conducted numerical studies on the circular CFT columns by using the shell-solid based element model. This model was performed on the software of ATENA. The element selection of their study was similar to Skalomenos's. The analytical results show a good consistence with the experimental results reported by Inai et al. (2004).

Similar analytical studies were conducted by other researchers (Huang 2018; Stephens et al. (2016); Yang et al. (2018); Zenzai et al. (2018)). Generally speaking, the accuracy of a shell-solid element analysis greatly exceeded the conventional fiber-based models. As shown in Fig. 3-13, the buckling shape of CFT columns can be accurately simulated by this method. However, a problem of application of this kind of exquisite model is the cost and convergence. The number of studies applying shell solid element based model is very limited. Meanwhile, until the present, no numerical study of CFT columns under the dynamic load with this kind of model was reported. This is due to the efficiency. This also indicates that shell solid element analysis of large-scale structural system is still unrealistic.

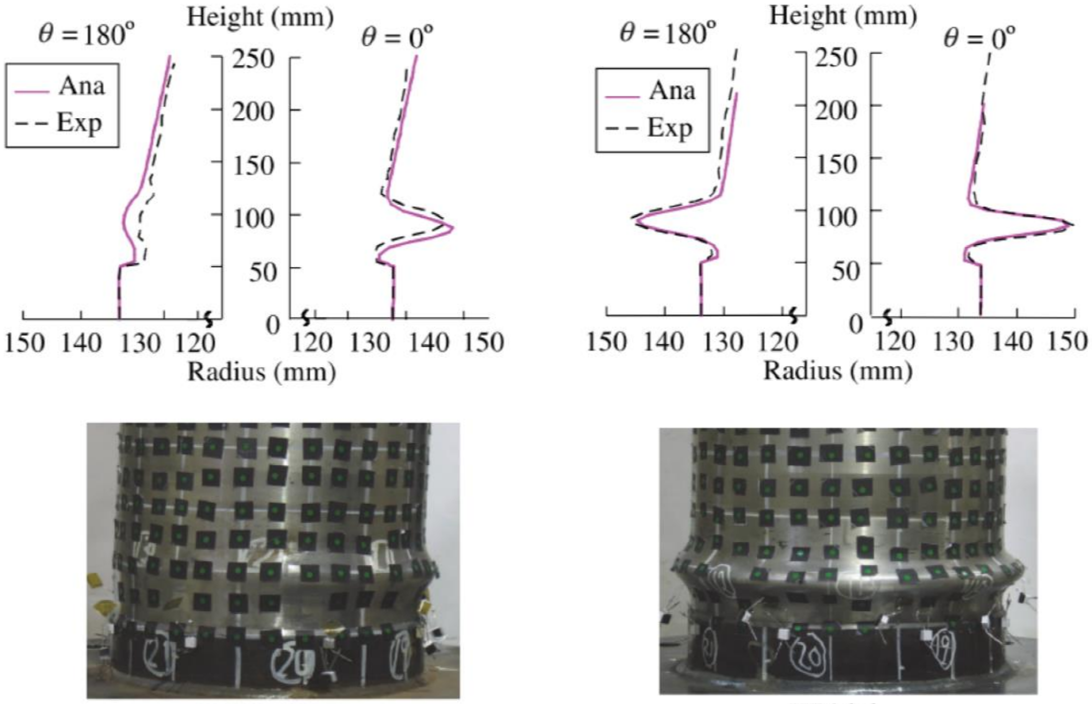

CCFT4.0-2
(CFT, $R_t = 0.09$, $\delta / \delta_0 = 7$)

HT4.0-2
(Hollow, $R_t = 0.09$, $\delta / \delta_0 = 5$)

Fig. 3-14. Comparison of analytical results and experimental results of shell solid element model.

Chapter 4. Segment model of circular CFT columns

4.1 General

Thin-walled concrete-filled tubular steel columns with fixed base illustrated in Fig.4-1 have been widely used in Japan as the piers of highway bridges. This is due to their enhanced seismic performance: strength, ductility and energy dissipation capacity, compared with that of hollow steel columns. As bridge piers, thin-walled partially concrete-filled tubular steel columns, herein referred to as thin-walled PCFT columns are more preferred because the reduced volume of the in-filled concrete is considered to mitigate the magnitude of seismic inertia forces. The steel tubes used for the thin-walled PCFT columns normally have a large diameter of 2~3 m. Their radius-to-thickness ratio parameter R_t , slenderness ratio parameter $\bar{\lambda}$ and axial force ratio $P/\left(\sigma_y A_s\right)$ are approximately in the ranges shown below

$$0.06 \le R_t = \frac{D_s}{2t_s}\frac{\sigma_y}{E_s}\sqrt{3(1-\nu_s^2)} \le 0.12 \qquad (4\text{-}1a)$$

$$0.25 \le \bar{\lambda} = \frac{1}{\pi}\sqrt{\frac{\sigma_y}{E_s}}\frac{2h_p}{r_s} \le 0.6 \qquad (4\text{-}1b)$$

$$0.05 \le P/\left(\sigma_y A_s\right) \le 0.2 \qquad (4\text{-}1c)$$

where D_s , t_s , r_s , A_s, σ_y , E_s and ν_s are diameter, thickness, radius of gyration, cross-sectional area, yield stress, Young's modulus, Poison's ratio, respectively, of the outer-steel tubes. h_p is the height of the columns. P is the compressive load acting at the top of the columns.

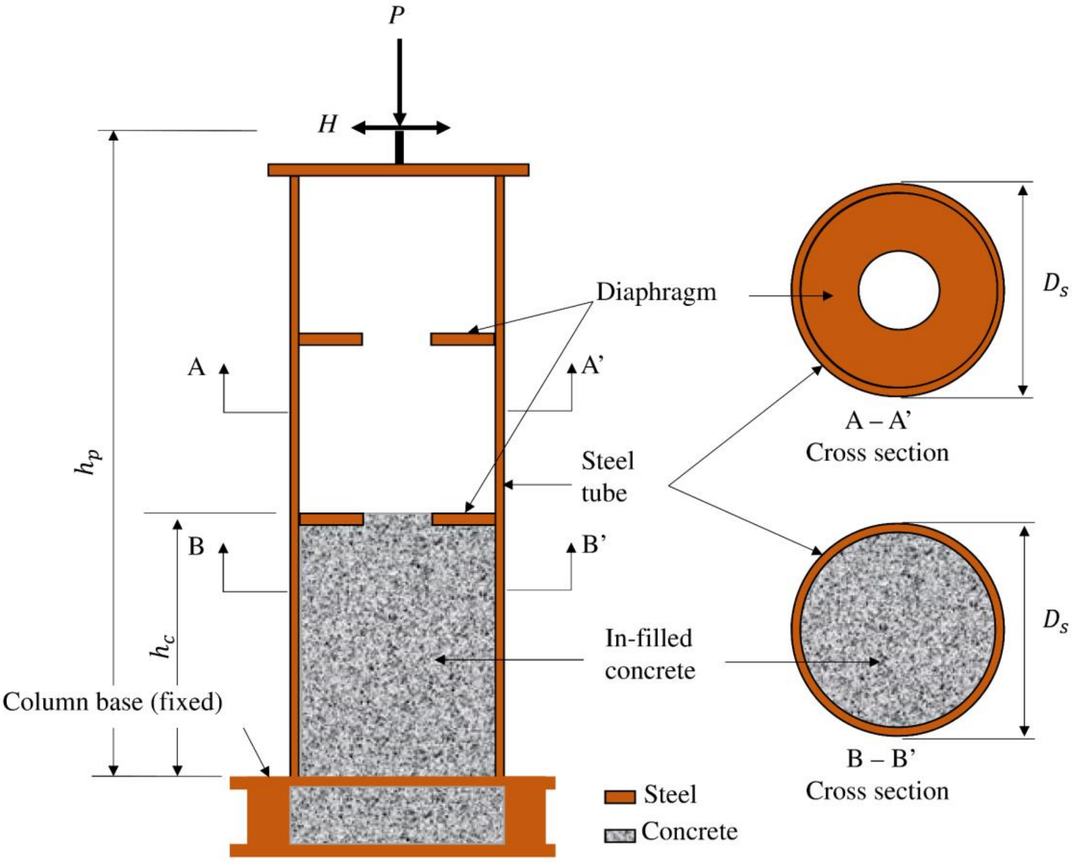

Fig. 4-1. Thin-walled PCFT column

The steel tubes of the PCFT columns are filled with concrete only in their lower part, that is, the range from the column base up to the first or the second diaphragm that is located at the height between D_s and $2.5\,D_s$. This range is determined such that the local buckling will not occur at the hollow section above the concrete-filled section until the columns reach their ultimate states. The diaphragms installed inside the steel tubes play an important role to confine the in-filled concrete as well as to transmit the compressive axial stress from the steel tube to the in-filled concrete. The above requirements are used in design to ensure the strength and ductility of the thin-walled PCFT columns (Japan Society of Civil Engineers 2018).

A series of researches have been done to assess the enhanced seismic performance of the PCFT columns (Goto ; Goto et al. (2010, 2012, 2014, 2017)). Experiments in these researches have shown that the local buckling restraining behavior of the PCFT columns considerably enhances their seismic performance. To assess the ultimate behavior of the thin-walled PCFT piers including the behavior in the post peak range, Goto et al. (2010, 2012) presented an advanced versatile FE analysis based on a considerably accurate model, herein, referred to as shell-solid element model. This model directly takes into account the cyclic local buckling of the steel tube, the nonlinear behavior of the confined in-filled concrete and the interface action between the steel tube and in-filled concrete. The most significant feature of the shell-solid element model is that this model can directly evaluate the local multi-axial strains and stresses in the outer-steel tube. The information about these quantities is important to prevent the ductile fracture and low cycle fatigue of the outer-steel tube that may cause a premature failure of the PCFT columns. The accuracy and versatility of the shell-solid element model were confirmed extensively by comparing to the results of cyclic loading tests and shake table tests on the single PCFT columns. However, this model requires unrealistically long computation time and often encounters numerical difficulty to obtain convergent solutions, when applied to large structural systems like the elevated-girder bridge systems with multiple thin-walled PCFT piers. Therefore, the objective of the present research is to propose a computationally efficient and accurate

3D numerical model that can be applied to assess the seismic performance of the bridge systems with multiple thin-walled PCFT piers.

As computationally efficient and practical models for the analysis of the conventional CFT columns under cyclic loading, various fiber-based beam models have been presented by numbers of researchers (Chung et al. (2007); Denavit and Hajjar 2012; Susantha et al. (2001); Valipour and Foster 2010; Varma et al. (2002)) among others). In these models, the effects of the local buckling of the steel tube and the confinement of the concrete core are approximately taken into account by modifying the uniaxial stress-strain relations of steel and concrete that are to be applied to the fibers of the beam models. For the parameter calibration of these modified stress-strain relations, some loading tests on real-sized specimens are necessary because of the scale effect on concrete behavior (Yamamoto et al. (2002)). These tests, even if they are stub column tests, are cumbersome specifically in the case of the large-sized bridge piers. For design applications, the tests on wider range of the CFT members will be further necessary to derive formulas to specify the parameter values for various cases in design analysis.

So far as the large-sized thin-walled PCFT columns used for the bridge piers are concerned, it is specifically hard for the conventional fiber-based beam models to predict their ultimate and subsequent post-peak hysteretic behavior with the accuracy comparable to the shell-solid element model. This is because the local buckling deformation of the outer-steel tube becomes large at the ultimate state of the thin-walled PCFT columns, resulting in a rather complicated contact with friction behavior at the interface between the steel tube and in-filled concrete. This behavior cannot be properly simulated by the conventional fiber-based composite beam models, because the restrictive composite beam assumptions: no deformation of cross-sectional shapes and the Bernoulli-Euler hypothesis, are introduced to express the behavior of the PCFT columns.

The numerical model proposed herein is intended for the application to an advanced seismic analysis to directly assess the 3D performance of large bridge systems with multiple thin-walled PCFT piers (Japan Society of Civil Engineers 2018). The proposed model is a fiber-based model with a failure segment applied to the damaged part of the thin-walled PCFT columns with local buckling deformations. However, being different from the conventional fiber-based beam models for the CFT columns, the failure segment composed of a single beam element and multiple truss elements is introduced to simulate the complicated interaction behavior between the locally buckled outer-steel tube and the in-filled concrete. In this way, the composite beam assumptions are not introduced into the proposed fiber-based model with the failure segment. Therefore, the proposed model is less restrictive. Another significant difference between the proposed model and the conventional fiber-based beam model is that all the parameter values of the failure segment in the proposed model are simultaneously calibrated by a systematic mathematical optimization technique, referring only to the in-plane hysteretic curve of each single thin-walled PCFT column. This in-plane hysteretic curve is calculated by the accurate shell-solid element model. In the proposed new model, a sufficient number of parameters are introduced to the failure segment to ensure its accuracy comparable to that of the shell-solid element model. Regarding the large-sized PCFT columns used for the bridge piers, it is very difficult to conduct loading tests on real-sized specimens. Therefore, the parameter calibration based on the shell-solid element model analysis is indispensable.

The accuracy and computational efficiency of the fiber-based model with the failure segment for the seismic analysis of the thin-walled PCFT columns were extensively examined by comparing to the results of the shell-solid element model analysis as well as experiments. The experiments consist of bi-directional cyclic loading tests and shake table tests on single PCFT column specimens and a multi-shake table test on a 2-span elevated girder bridge model supported by multiple PCFT piers.

4.2 Shell-solid element model for analysis of cyclic behavior of thin-walled PCFT columns

The shell-solid element model for the accurate analysis of the thin-walled PCFT columns played an important role in establishing the concept of the newly proposed fiber-based model with the failure segment. The shell-solid element model is also important in providing the in-plane hysteretic curve data for each PCFT column. This data is used as a reference to directly identify the parameter values of the failure segment used in the proposed fiber-based mode. Therefore, some details of the shell-solid element model are herein explained.

The shell-solid element model proposed for the seismic analysis of the thin-walled PCFT columns was constructed in ABAQUS 6.14 (Simulia 2014) by Goto et al. (2010, 2012, 2014). In the shell-solid element model, the steel tube and in-filled concrete are represented by geometrically and materially nonlinear thick shell elements (S4R) and solid elements (C3D8R), respectively, as shown in Fig. 2. To express the material behavior in these elements, the three-surface cyclic metal plasticity model (Goto et al. (1998, 2006, 2009)) implemented in ABAQUS by user subroutine feature is applied to the steel tube, while the concrete damaged plasticity model (Lee and Fenves 1998) is used for the in-filled concrete. The concrete damaged plasticity model, however, assumes isotropic plasticity both on the compression and tension sides. Therefore, this model is considerably approximate in nature, concerning the opening and closing behavior of cracks under cyclic load. To make up for the inaccuracy of the damaged plasticity model on the tension side, the discrete crack models (Chen 1982) expressed by the hard contact pairs are inserted horizontally in the in-filled concrete at the location of the major penetrating tension cracks (Fig. 4-2). The interface action between the steel tube and in-filled concrete, that is, the contact with friction behavior is simulated by the hard contact pairs with the Coulomb friction model.

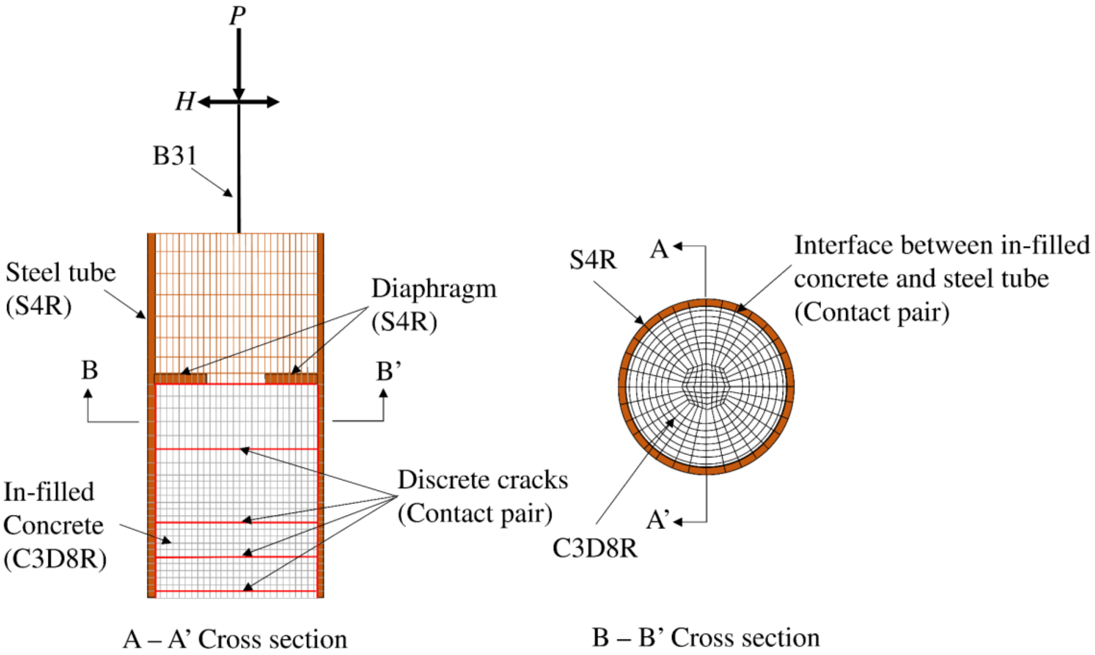

Fig. 4-2. Shell-solid element model of thin-walled PCFT column

The validity and accuracy of the shell-solid element model were confirmed by comparing to the test results obtained from numbers of cyclic loading tests and shake table tests (Goto et al. (2009, 2010, 2012, 2014)) on the PCFT column specimens with the structural parameters in the range of the bridge piers defined by Eqs. (4-1*a*) ~ (4-1*c*).

4.3 Proposed fiber-based model with failure segment

4.3.1 General

The computationally efficient, yet accurate numerical model proposed herein for the seismic analysis of the thin-walled PCFT columns is a fiber-based model with a failure segment. This segment is applied primarily to the concrete-filled part of the PCFT columns. The fiber-based model with the failure segment is intended for the analysis of the PCFT columns used for the bridge piers with the parameter range defined by Eqs.

(4-1*a*) ~ (4-1*c*). In these columns, the bending deformation is dominant and this deformation property is reflected in the proposed model illustrated in Fig. 4-3. The length L_f of the failure segment inserted at the bottom of the column usually coincides with the height h_c of the partially in-filled concrete ranging from the column base to the top of the first or the second diaphragm installed to the steel tube. However, the maximum value of L_f is limited to the fixed value of $0.35h_p$, where h_p is the height from the column base to the horizontal force point. This implies that the length of the damaged part of the PCFT columns is assumed not to spread beyond $0.35h_p$, even if the height of the in-filled concrete exceeds $0.35h_p$.

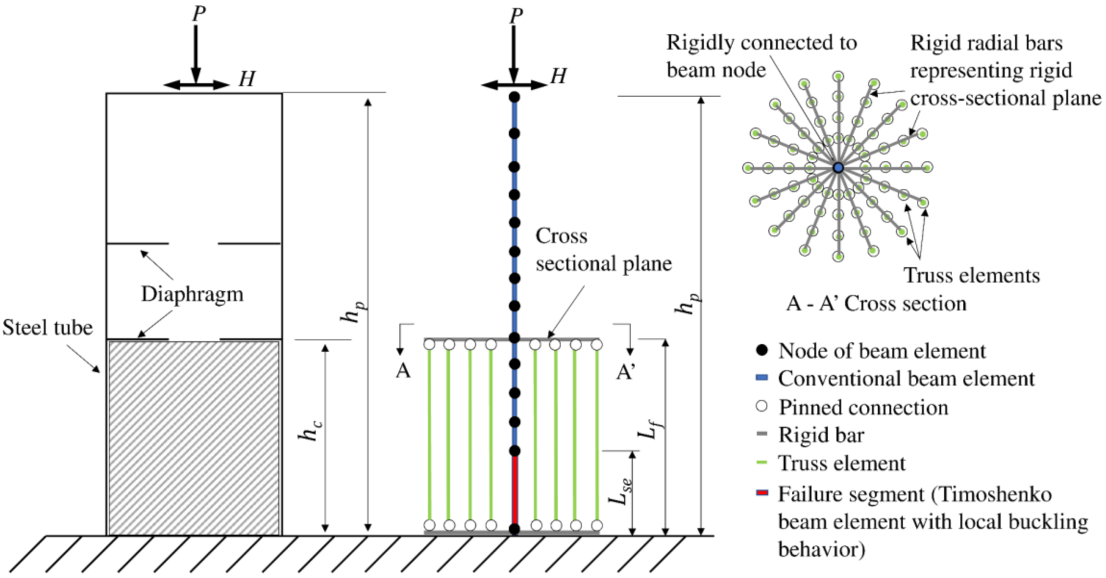

Fig. 4-3. Fiber-based model with failure segment for analysis of thin-walled PCFT columns

The failure segment is used to simulate the complicated interaction behavior between the locally buckled outer-steel tube and the in-filled concrete, since this behavior cannot be properly simulated by the conventional fiber-based beam model. This is because the conventional fiber-based beam model employs the restrictive composite beam assumptions: no change of cross-sectional shapes and the Bernoulli-Euler Hypothesis where the cross-sectional planes keep plane throughout the deformation.

The region of the PCFT columns above the failure segment is represented by the conventional Timoshenko beam elements B31 in ABAQUS (Simulia 2014). In case when the PCFT columns are hollow above the failure segment, the PCFT columns are normally designed such that the local buckling will not occur at the hollow section until the columns attain their ultimate state. Therefore, the application of the conventional beam elements to the hollow part is justified. On the other hand, when the steel tube is filled with concrete in the region above the failure segment, the conventional beam elements with the composite beam assumptions are applied to this region where local buckling will not occur in the outer-steel tube. Regarding the uniaxial constitutive relations applied to the fibers of the conventional beam elements, a bi-linear model with the kinematic hardening rule shown in Fig. 4-4 (a) is used for the outer-steel tube section, while the constitutive model shown in Fig. 4-4 (b) is used for the in-filled concrete section. The details of the constitutive models for the in-filled concrete in the failure segment will be explained later.

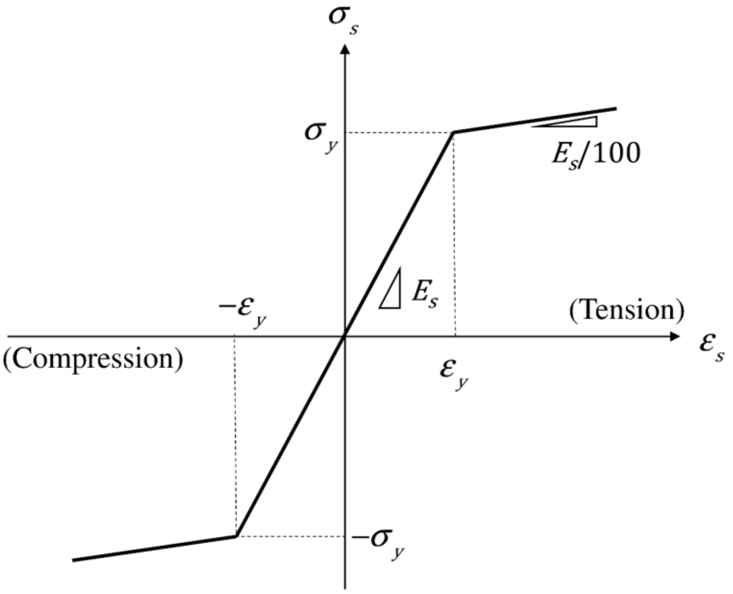

(a) Uniaxial constitutive model for outer-steel tube

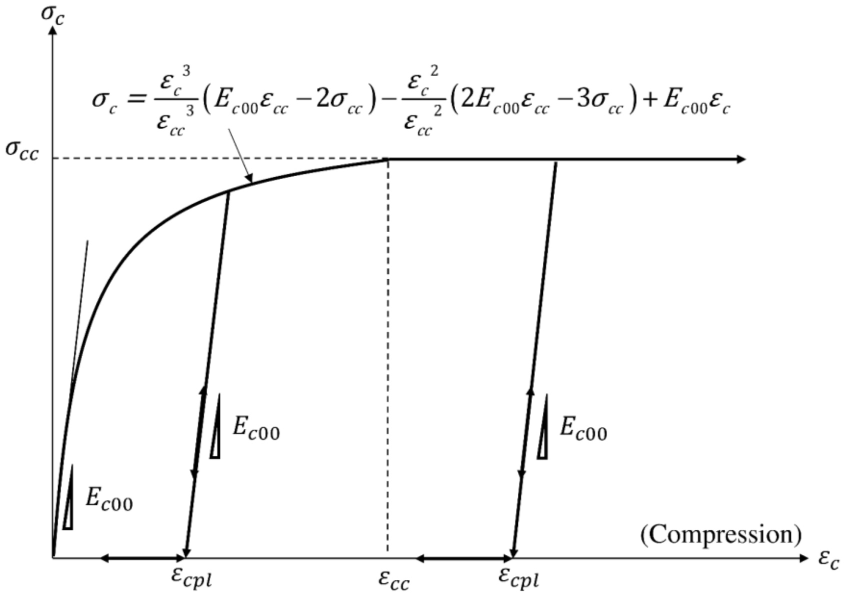

(b) Uniaxial constitutive model for in-filled concrete

Fig. 4-4. Material models applied to the region of PCFT columns without local buckling

In the proposed fiber-based model with the failure segment, the parameters for the failure segment are identified such that this model well reproduces the in-plane hysteretic horizontal force-horizontal displacement curves of the PCFT columns calculated by the shell-solid element model. Since the behavior of the confined in-filled concrete with cracks are reflected in the hysteretic curves of the columns computed by the shell-solid element model, the effect of the in-filled concrete is equally reflected in the hysteretic curves calculated by the proposed model.

4.3.2 Modeling of failure segment

The failure segment with the length of L_f is composed of the Timoshenko beam elements and multiple truss elements, as illustrated in Fig. 4-3. The Timoshenko beam elements model the outer-steel tube, while the multiple truss elements model the in-filled concrete. The shear deformation due to shear force is assumed to be elastic in the Timoshenko beam elements (B31). A single beam element with the length of L_{se} is located at the lower part of the failure segment to represent the local buckling behavior of the outer-steel tube. The use of the single beam element is to avoid the numerical difficulty caused by the localization that occurs in case when the locally buckled part of the steel tube is discretized by serially connected multiple elements with softening constitutive relations. L_{se}, herein referred to as effective local buckling length, is assumed to be smaller than the failure segment length L_f. The steel tube in the failure segment excluding the local buckling part with the length of L_{se} is discretized by the conventional Timoshenko beam elements with the constitutive relation shown in Fig. 4-4(a). The length of L_{se} is identified in a calibration process with an optimization technique explained later. The in-filled concrete is represented by the multiple truss elements (T3D2) with the length of L_f. Both ends of these truss elements are pinned to the rigid cross-sectional planes of the Timoshenko beam elements at the upper and lower ends of the failure segment. As shown in Fig. 4-3, these rigid cross-sectional planes of the Timoshenko beam element are expressed herein by the radial rigid cross-sectional bars with one end fixed to the nodes of the beam elements at the heights of 0 and L_f. The total cross-sectional area of the multiple truss elements is equal to that of the in-filled concrete. The above modeling of the in-filled concrete by the multiple truss elements implies that the shear stiffness of the in-filled concrete in the failure segment is ignored. However, this modeling was numerically confirmed to be acceptable, because the shear deformation of the outer steel tube in the region of the failure segment with the length L_f less than $0.35h_p$ is so small that the shear stiffness of the in-filled concrete little affects the response displacement of the PCFT piers with the parameter range defined by Eqs. (4-1*a*) ~ (4-1*c*) .

4.3.3 Constitutive relation of steel tube in the locally buckled part of the failure segment

The uniaxial constitutive relation based on Fig. 4-5 is adopted for the fibers of the single Timoshenko beam element that is used to represent the locally buckled part of the outer-steel tube with the effective local buckling length of L_{se}. The tensile and compressive stresses for this part are assumed to be expressed by the functions f_t and f_c as

$$\sigma = f_t \quad (\sigma \geq 0), \quad \sigma = f_c \quad (\sigma < 0) \qquad \text{(4-2}a, b\text{)}$$

f_t and f_c are mathematically defined as the functions of the plastic strain ε_{pl}. In what follows, f_t and f_c are explicitly shown for the case under monotonic loading and that under cyclic loading.

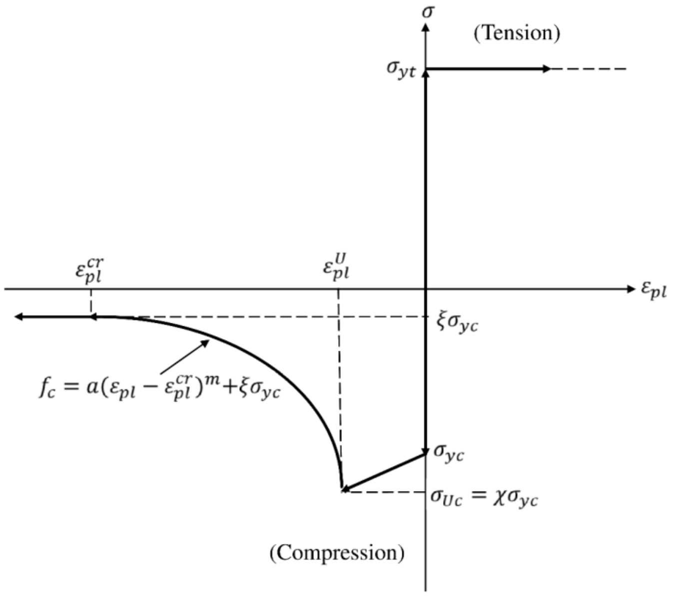

(a) Monotonic load

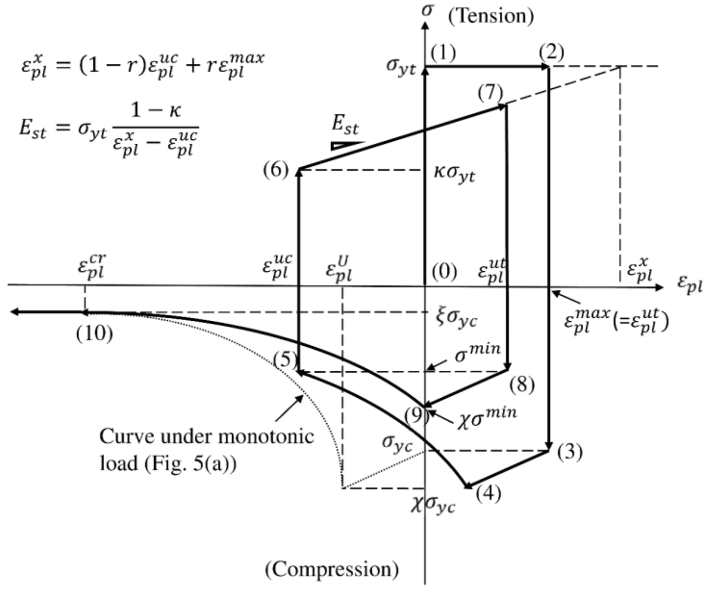

(b) Cyclic load

Fig. 4-5. Uniaxial constitutive model for locally buckled part of steel tube with length of L_{se}

Under monotonic loading, the constitutive relation is schematically shown in Fig. 4-5(a). In this case, f_t and f_c are expressed as

$$f_t = \sigma_{yt} \tag{4-3a}$$

$$f_c = \begin{cases} \xi\sigma_{yc} & \left(\varepsilon_{pl} \le \varepsilon_{pl}^{cr}\right) \\ a\left(\varepsilon_{pl} - \varepsilon_{pl}^{cr}\right)^m + \xi\sigma_{yc} & \left(\varepsilon_{pl}^{cr} < \varepsilon_{pl} \le \varepsilon_{pl}^{U}\right) \\ \dfrac{\chi - 1}{\varepsilon_{pl}^{U}}\sigma_{yc}\varepsilon_{pl} + \sigma_{yc} & \left(\varepsilon_{pl}^{U} < \varepsilon_{pl}\right) \end{cases} \tag{4-3b}$$

where

$$a = \left(\chi\sigma_{yc} - \xi\sigma_{yc}\right) / \left(\varepsilon_{pl}^{U} - \varepsilon_{pl}^{cr}\right)^m \tag{4-4}$$

σ_{yt} and σ_{yc} are the initial yield stresses on the tension and compression sides, respectively. χ is a factor multiplied by σ_{yc} to express the maximum stress σ_{pl}^{U} on the compression side. ε_{pl}^{U} is the plastic strain at σ_{pl}^{U}. m is a power index that determines the shape of the softening curve on the compression side. ξ is a constant to specify the lower bound of the compression stress f_c, and ε_{pl}^{cr} is the plastic strain at this lower bound.

Under cyclic loading, the hysteretic rule of the constitutive relation applied to the locally buckled part of the steel tube is schematically shown in Fig. 4-5(b). This rule was determined herein by simplifying the model proposed by Ishizawa and Iura (2006) in terms of the hardening behavior both on the tension and compression sides. In Fig. 4-5(b), ε_{pl}^{max} is the maximum tensile plastic strain that occurs throughout the loading history. ε_{pl}^{ut} and ε_{pl}^{uc} are the plastic strains when unloading occurs at points (7) and (5), respectively. Superscript *t* and *c* in these notations denote the unloading on the tension side and that on the compression side, respectively. σ^{min} is the minimum value of the compressive stress as the result of the softening behavior from point (4) to point (5), and σ^{min} becomes a yield point (point (8)) in the next reloading on the compression side.

The softening stress-plastic strain relation on the compression side is defined by a curve oriented to the ultimate point $(\xi\sigma_{yc}, \varepsilon_{pl}^{cr})$ $(\xi \leq 1.0)$ such as the curve from point (4) to point (5) or that from point (9) to point (10) in Fig. 4-5(b). In the unloading process from point (5) on the compression side, the re-yielding point on the tension side (point (6)) is given by $\kappa\sigma_{yt}$ $(\kappa \leq 1.0)$. ε_{pl}^{x} is the tensile plastic strain when the tensile stress reaches the limiting stress σ_{yt} in the reloading process. Herein, ε_{pl}^{x} is defined by

$$\varepsilon_{pl}^{x} = (1-r)\varepsilon_{pl}^{uc} + r\varepsilon_{pl}^{max} \tag{4-5}$$

where r is a constant.

According to the hysteretic rule explained above, the functions f_t and f_c that define the tensile and compressive stresses under cyclic loading are mathematically expressed as

$$f_t = \begin{cases} E_{st}\left(\varepsilon_{pl} - \varepsilon_{pl}^{uc}\right) + \kappa\sigma_{yt} & \left(\varepsilon_{pl} \leq \varepsilon_{pl}^{x}\right) \\ \sigma_{yt} & \left(\varepsilon_{pl}^{x} < \varepsilon_{pl}\right) \end{cases} \tag{4-6a}$$

$$f_c = \begin{cases} \xi\sigma_{yc} & \left(\varepsilon_{pl} \le \varepsilon_{pl}^{cr}\right) \\ a'\left(\varepsilon_{pl} - \varepsilon_{pl}^{cr}\right)^m + \xi\sigma_{yc} & \left(\varepsilon_{pl}^{cr} < \varepsilon_{pl} \le \varepsilon_{pl}^{ut} + \varepsilon_{pl}^{U}\right) \\ \dfrac{\chi - 1}{\varepsilon_{pl}^{U}}\sigma^{min}\varepsilon_{pl} + \sigma^{min} & \left(\varepsilon_{pl}^{ut} + \varepsilon_{pl}^{U} < \varepsilon_{pl}\right) \end{cases} \tag{4-6b}$$

where

$$E_{st} = \sigma_{yt}\left(1-\kappa\right) / \left(\varepsilon_{pl}^{x} - \varepsilon_{pl}^{uc}\right) \tag{4-7}$$

$$a' = \left(\chi\sigma^{min} - \xi\sigma_{yc}\right) / \left(\varepsilon_{pl}^{U} + \varepsilon_{pl}^{ut} - \varepsilon_{pl}^{cr}\right)^m \tag{4-8}$$

In Fig. 4-5(b), the unloading and reverse-loading path from point (5) to point (7), passing through point (6), denotes the behavior how the locally buckled part of the steel tube is stretched under tensile stresses. The tensile re-yielding point (6) is reduced from the initial value σ_{yt} to $\kappa\sigma_{yt}$, considering the additional bending stress caused by the tensile stress at the locally buckled part. In addition, the reduction of the tensile stiffness due to the bending deformation at the locally buckled part is considered to be E_{st}, as given by Eq. (4-7).

The elastic modulus $E_{el}^{'}$ in the range $(f_c < \sigma < f_t)$ is given as follows, considering the reduction due to the residual bending deformation of the buckled part.

$$E_{el}^{'} = \left(1 - \eta\varepsilon_{pl}\right)E_{el} \tag{4-9}$$

where E_{el} is the initial elastic modulus and η ($0 \le \eta < 1/\varepsilon_{pl}$) is a constant parameter that describes the reduction in the elastic modulus.

4.3.4 Constitutive relation of infilled-concrete in failure segment

In many existing fiber-based models for CFT columns (Hatzigeorgiou 2008; Hatzigeorgiou 2008; Liang and Fragomeni 2009; Tort and Hajjar 2010), the stress-strain curves of the in-filled concrete on the compression side are usually composed of three parts: an ascending part up to a confined strength (Mander et al. (1988); Shams and Saadeghvaziri 1999), a descending part and a horizontal part with a constant strength.

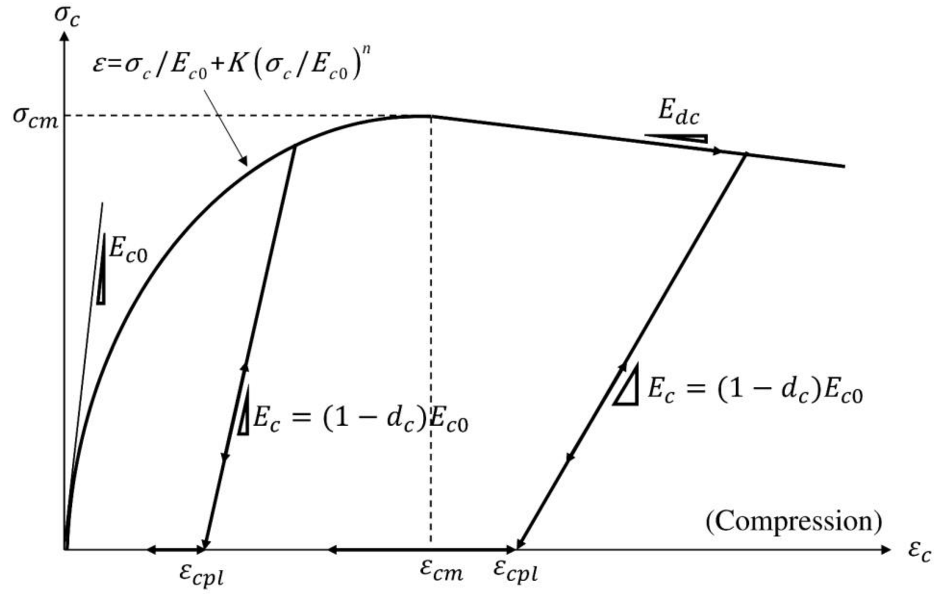

Fig. 4-6. Uniaxial constitutive model for in-filled concrete in failure segment

In the proposed model, the stress-strain relation illustrated in Fig. 4-6 is used. The ascending part up to the compression strength σ_{cm} is expressed by the Ramberg-Osgood 3-parameter model (Ramberg and Osgood 1943) as

$$\varepsilon_c = \sigma_c / E_{c0} + K\left(\sigma_c / E_c\right)^n \tag{4-10}$$

where E_{c0} denotes the initial elastic modulus. n is a constant parameter. K is expressed by σ_{cm} and ε_{cm} as

$$K = \left(\varepsilon_{cm} - \sigma_{cm} / E_{c0}\right) / \left(\sigma_c / E_c\right)^n \tag{4-11}$$

The descending part starting from the compressive strength σ_{cm} is approximated by a straight line with the softening stiffness of E_{dc}. When this descending straight line reaches the abscissa of $\sigma_c = 0$, the stress σ_c remains zero with the increase of the strain ε_c .

The unloading elastic modulus E_c is given by

$$E_c = \left(1 - d_c\right) E_{c0} \tag{4-12}$$

where d_c is a damage parameter defined by Goto et al. (2010) as

$$d_c = \omega_d k_{cl} \varepsilon_c / \left[1 + \left(\varepsilon_c / \varepsilon_0\right)^{n'}\right]^{1/n'} \tag{4-13}$$

where ω_d = reduction factor, k_{cl} = 155, ε_0 = 0.0035 and n' = 2.0.

The tensile strength is assumed to be zero. Therefore, E_c becomes zero when total strain ε_c decreases to be less than plastic strain ε_{cpl}. This is to simulate the opening behavior of the horizontal cracks under tensile stresses.

4.3.5 Calibration of parameter values used for failure segment

All the parameter values for the failure segment applied to the analysis of the thin-walled PCFT columns under multi-directional seismic accelerations are directly calibrated by an optimization technique, referring to the in-plane hysteretic curves of the respective single thin-walled PCFT column models calculated by the shell-solid element model analysis. The total number of the parameters that have to be identified simultaneously amounts to 18, which are classified into 3 groups. The first group includes one geometrical parameter: effective buckling length of the steel tube L_{se}. The second group consists of 11 material parameters to define the stress-strain curve for the locally buckled part of the steel tube in the failure segment: initial elastic modulus E_{el}, yield stresses (σ_{yt}, σ_{yc}) on the tension and compression sides, parameters (ε_{pl}^{U}, χ, m) to define the strain hardening curve on the compression side, parameters (ε_{pl}^{cr}, ξ) to define the ultimate point on the compression side, a parameter κ to define the tensile yield point in the reloading process, a parameter r to determine the plastic strain ε_{pl}^{x} when tensile stress reaches σ_{yt} and a reduction factor η of the initial elastic stiffness E_{el}. The third group consists of 6 material parameters used to define the stress-strain curve for the in-filled concrete in the failure segment: initial elastic modulus E_{c0}, parameter n in the 3-parameter model used to express the ascending part of the constitutive relation, peak point (σ_{cm}, ε_{cm}) of the stress-strain curve, softening stiffness E_{dc} of the stress-strain curve and reduction factor ω_d of the damage function d_c.

18 unknown parameter values for the failure segment are calibrated simultaneously by an optimization technique such that the reference in-plane hysteretic curve for each single thin-walled PCFT column under a constant compressive load P is best fitted by the curve calculated by the fiber-based model with the failure segment. As an optimization method, the downhill simplex method is employed herein to identify the

values of the unknown parameters. The objective function to be minimized by the optimization technique is given by

$$\Delta = \sum_{i}^{n_\sigma} \left| H_i^{FE} - H_i^{SE} \right| / n_\sigma H_0 \rightarrow min \tag{4-14}$$

where H_i^{FE} and H_i^{SE} are the *i*-th column top horizontal forces on the in-plane hysteretic horizontal force- horizontal displacement curves calculated by the shell-solid element model and the proposed fiber-based model with the failure segment, respectively. H_0 is the initial yield horizontal force defined by Eq. (4-16). n_σ is the total number of the calibration points on the in-plane hysteretic curve of each column. These calibration points have to be determined from accuracy and efficiency. In the examples shown in this paper, the calibration points were selected at every displacement increment of δ_0.

As the loading protocol adopted herein to obtain the in-plane hysteretic curves of the PCFT columns, a fully reversed displacement-controlled unidirectional alternate load is applied to the top of the columns under a constant compressive load *P*. The amplitude of the alternate load is assumed to increase by δ_0 in a stepwise manner after one cycle of loading, as shown in Fig. 4-7. δ_0 is the initial yield displacement given by

$$\delta_0 = H_0 h^3 / \left(3 E_s I_s\right) \tag{4-15}$$

where H_0 is the initial yield horizontal force calculated by

$$H_0 = \left(\sigma_y - {}^{P}\!/_{A_s} \right) Z_s / h_p \tag{4-16}$$

In Eqs. (4-15) and (4-16), h_p, E_sI_s, A_s and Z_s denote the height, bending rigidity, cross-sectional area and section modulus, respectively, of the hollow steel tube with fixed base.

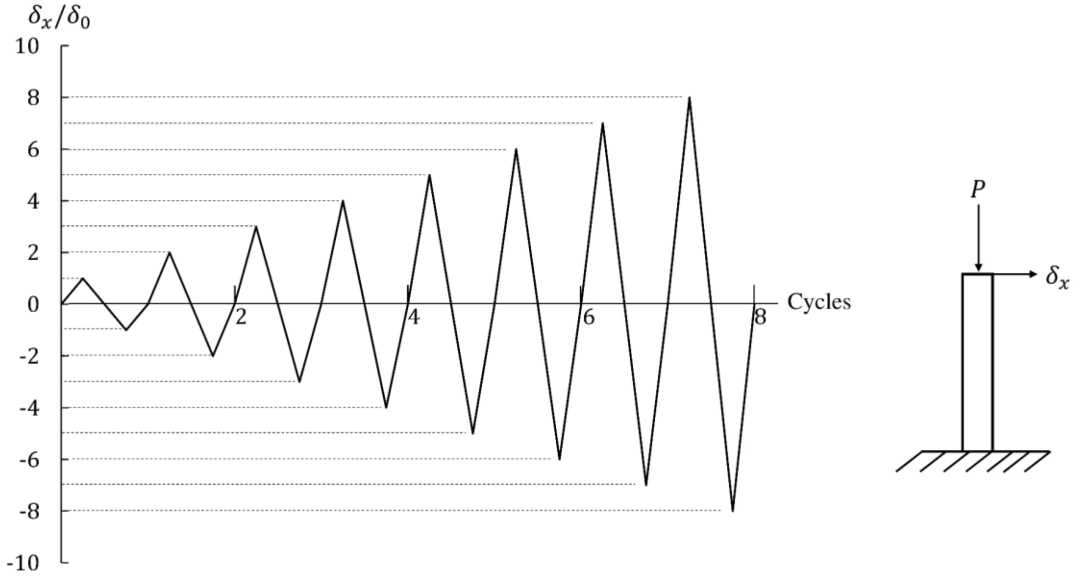

Fig. 4-7. Unidirectional displacement-controlled alternate load

It should be noted that the in-plane hysteretic curves of the PCFT columns obtained by cyclic loading tests can also be used instead of those calculated by the shell-solid element model analysis as reference data for the parameter calibration of the failure segments.

The flow chart of how to apply the proposed fiber-based model to the analysis of a bridge system with multiple thin-walled PCFT piers is illustrated in Fig. 4-8. This flow chart will be explained later, referring to the application examples.

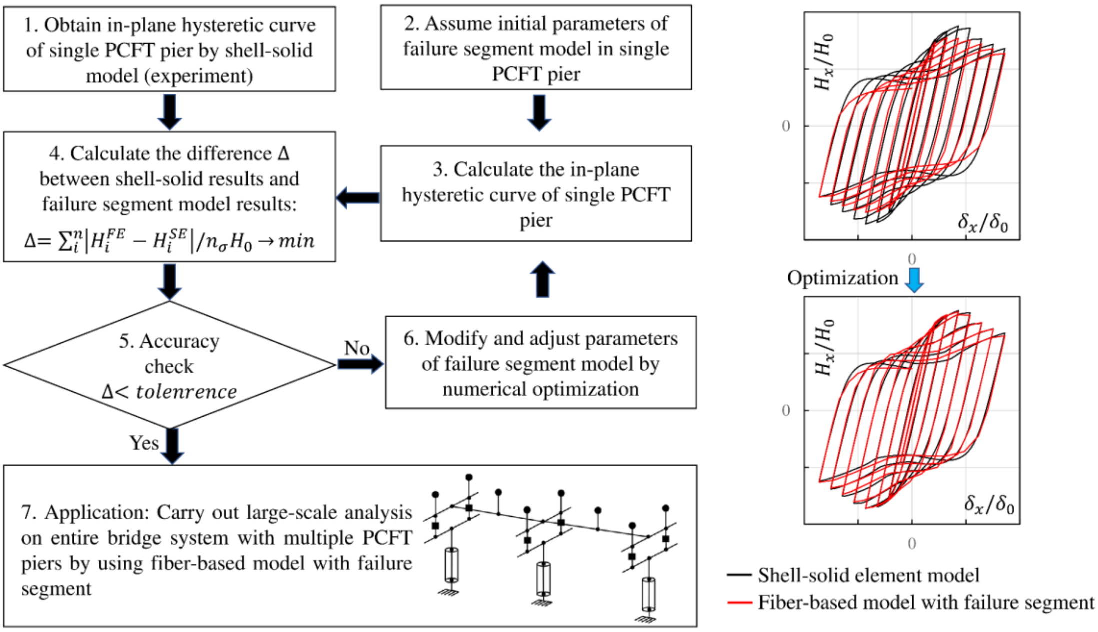

Fig. 4-8. Flow chart of analysis of PCFT columns by fiber-based model with failure segment

Chapter 5. Verification of proposed analytical model

5.1 General

The validity and accuracy of the proposed fiber-based model with the failure segment were examined by comparing its numerical results to the experimental results or to the accurate numerical results obtained by the shell-solid element model analysis. The experiments used for this comparison consist of three types conducted by authors in the past to examine the seismic performance of the PCFT piers: cyclic loading tests on thin-walled hollow and PCFT piers (Goto et al. (2006, 2014)), shake table tests on single PCFT piers (Goto et al. (2014)) and a shake table test on a two-span elevated-girder bridge system with multiple PCFT piers (Goto et al. (2017)). Herein, due to page limitations, the validity and accuracy of the proposed model are discussed when this model is applied to the simulations of the first and the third experiments.

5.2 Cyclic loading tests on single thin-walled hollow and PCFT piers

Cyclic loading tests were performed on 1/8-scale PCFT column specimens under a constant vertical compressive load P, as illustrated in Fig. 5-1 (Goto et al. (2014)). In these test, two types of displacement-controlled loading protocols were used. One is a fully reversed displacement-controlled unidirectional alternate horizontal load shown in Fig. 4-7. The other is a bidirectional horizontal load with a displacement-controlled spiral load pattern shown in Fig. 5-2. This spiral load pattern is defined by the equation

$r_p = \delta_0\theta/(2\pi)$ in polar coordinates, where r_p and θ denote the radial and angular coordinates, respectively. In polar coordinates, the directions of $\theta = 0$ and $\pi/2$ are assumed to coincide with the positive directions of the x- and y- axes, respectively. The above loading tests were conducted by the 3D loading system at Nagoya Institute of Technology in Japan (Goto et al. (2006); Obata and Goto 2007).

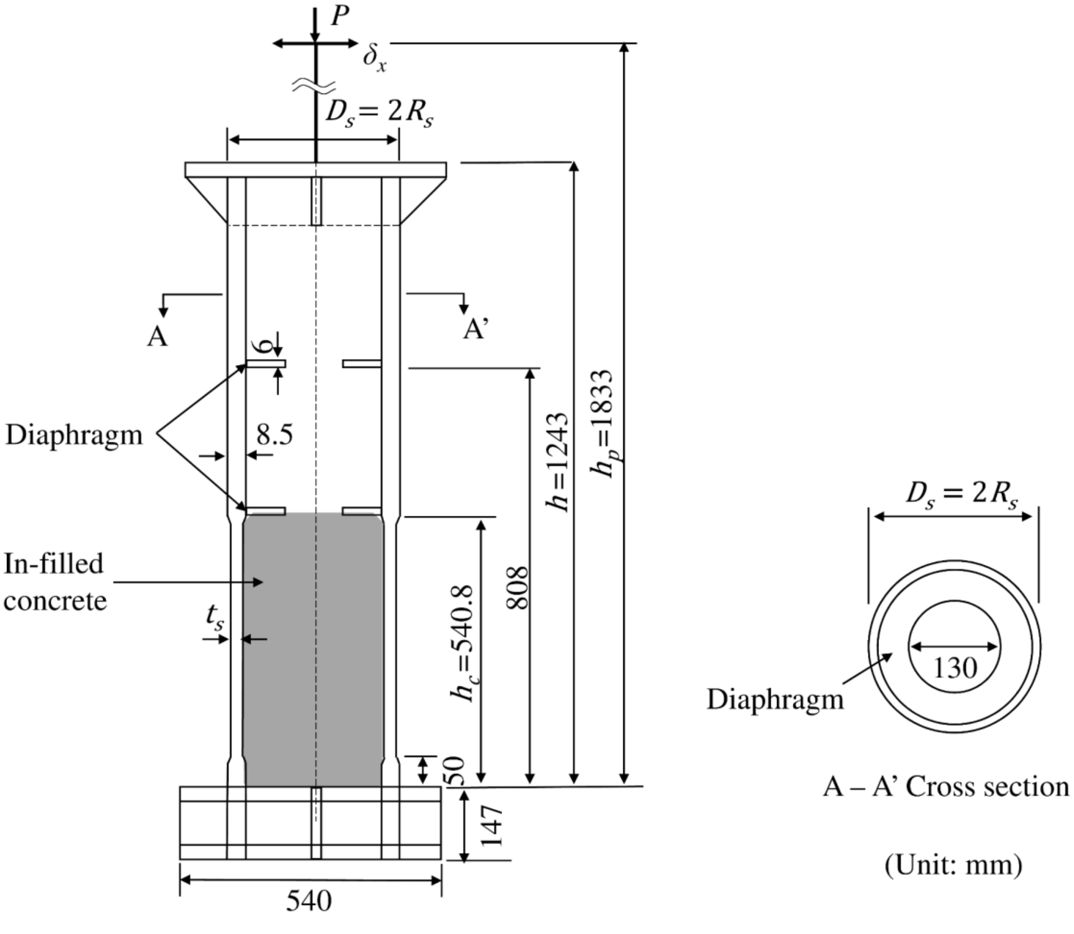

Fig. 5-1. Single PCFT column specimen used in cyclic loading test

Regarding the PCFT column models (Fig. 5-1) used in the experiment, two diaphragms were installed inside the outer-steel tube. The steel tubes were filled with concrete up to the height of $h_c = 0.295h_p \approx 2D_s$, which coincides with the height of the location of the lower diaphragm. This height was determined such that the local buckling will not occur at the hollow section above the concrete-filled section. In addition to the PCFT column models, one hollow column model denoted as HT column model was also tested for comparison under the loading protocols similar to those used for the PCFT column models. The geometrical and material properties of the column specimens along with the loading protocols used in the tests are summarized in Table 5-1. The outer-steel tubes of the PCFT column models have two kinds of target wall thicknesses t_s: 4mm and 5.5mm. The steel tube of the HT column model has a single target wall thickness of t_s : 4mm. For each column model, two specimens were manufactured. One was tested under the unidirectional alternate horizontal load and the other was tested under the bi-directional spiral load.

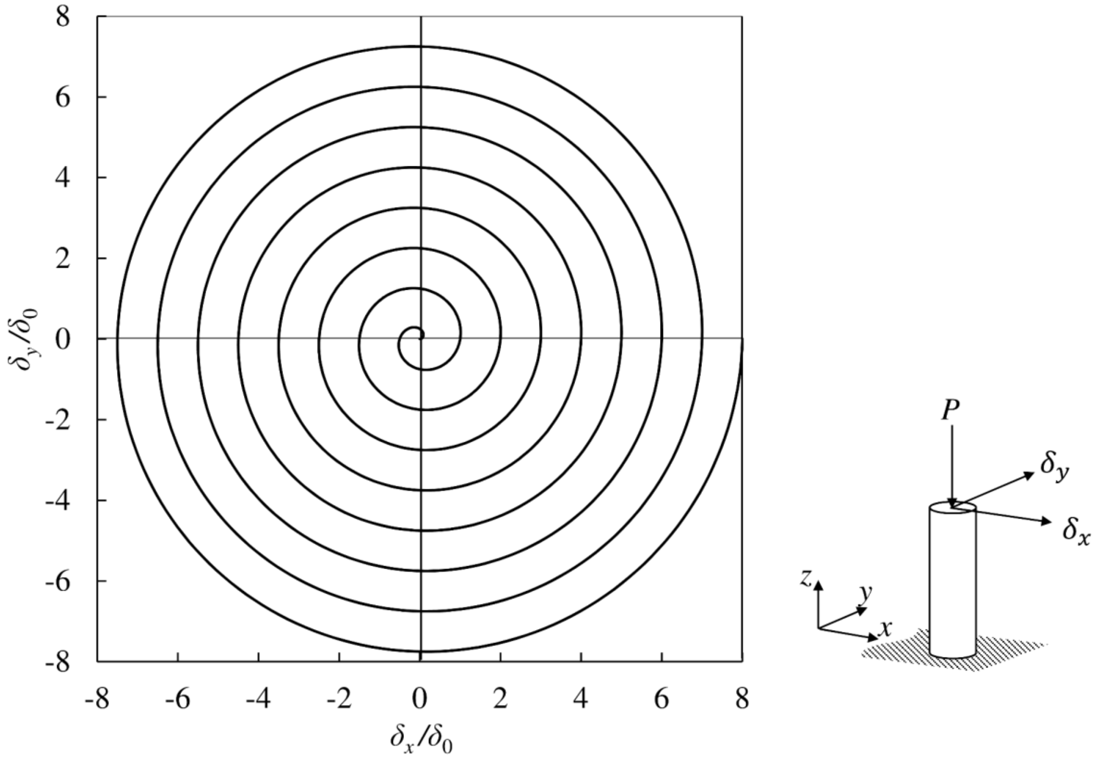

Fig. 5-2. Displacement-controlled spiral load

The analysis of the PCFT columns by using the fiber-based model with the failure segment were performed, following the procedure schematically shown in Fig. 8. In this fiber-based model, the length of the failure segment located at the lower part of the column is taken as $L_f = h_c$. First, the in-plane hysteretic curve used as a fitting target was calculated for each PCFT column specimen by the accurate shell-solid element model analysis under the loading protocol shown in Fig. 4-7. The details of this analysis are explained elsewhere (Goto et al. (2014)).

Table 5-1. Geometric and material properties of PCFT and HT column specimens used for cyclic loading test on single PCFT and HT columns

Specimen <pipe material>	D_s (mm)	t_s (mm)	h_c (mm)	R_t	$\overline{\lambda}$	H_0 (kN)	δ_0 (mm)	Loading protocol
CCFT4.0-1(CFT) <STK400>	262.00	3.97	540.8	0.094	0.529	38.96	9.89	Unidirectional alternate load
CCFT4.0-2(CFT) <STK400>	261.90	3.96	540.8	0.094	0.530	38.87	9.88	Bidirectional Spiral load
CCFT5.5-1(CFT) <STK400>	264.22	5.49	540.8	0.071	0.538	55.96	11.29	Unidirectional alternate load
CCFT5.5-2(CFT) <STK400>	264.15	5.48	540.8	0.071	0.539	55.59	11.25	Bidirectional Spiral load
HT4.0-1(Hollow) <STK400>	263.00	4.09	0	0.091	0.527	40.45	9.96	Unidirectional alternate load
HT4.0-2(Hollow) <STK400>	263.00	3.99	0	0.093	0.528	39.60	9.92	Bidirectional Spiral load

Note: D_s, t_s, h_p, h_c =see Fig. 9; $R_t = \frac{1}{2}\left(\frac{D_s}{t_s}\right)\left(\frac{\sigma_y}{E_s}\right)\sqrt{3\left(1-\nu_s^2\right)}$; $\overline{\lambda} = \frac{1}{\pi}\sqrt{\frac{\sigma_y}{E_s}}\cdot\frac{2h_p}{r_s}$, $r_s = \sqrt{\frac{I_s}{A_s}}$; H_0, δ_0 = see Eqs. 16 and 15; $\frac{P}{\sigma_y A_s} = 0.15$; h_p = 1833mm; <Steel pipes of CCFT4.0 and HT4.0> Young's modulus $E_s = 233.0$ (GPa), Poisson's ratio ν_s = 0.3, yield stress σ_y = 399.9(MPa), tensile strength σ_u = 498.2(MPa); <Steel pipes of CCFT5.5 and HT5.5 > Young's modulus $E_s = 232.0$ (GPa), Poisson's ratio ν_s = 0.3, yield stress σ_y = 414.3(MPa), tensile strength σ_u = 502.9(MPa); <In-filled concrete of CCFT4.0 and CCFT5.5> Young's modulus E_{c00} = 25.32~28.01(GPa), compression strength σ_{cc} = 28.43~34.3 (MPa), tensile strength σ_{ct} = 1.85~2.50(MPa).

Then, the down-hill simplex method was employed repeatedly to search for the optimum parameter values of the failure segment such that the in-plane hysteretic curve calculated by the fiber-based model with the failure segment best fits the target curve.

The concept of how to assume the initial parameter values in the optimization process is summarized in Table 5-2. For 8 parameters, formulas are shown to calculate their initial values. For the rest of the 18 parameters, that is, 10 parameters, numerical values are shown. The formulas as well as the numerical values in Table 5-2 were determined empirically for the PCFT bridge piers in the range defined by Eqs. (4-1*a*) ~ (4-1*c*).

Table 5-2. Assumed initial values of 18 parameters for failure segment

Parameters to be identified		Assumed initial values
Geometrical parameter of locally buckled part	L_{se} / D_s	$L_{se} = 3\sqrt{(D_s / 2)t_s}$: length of elephant foot bulge (Matsuura et al. (1995))
Stress-strain curve for locally buckled part of steel tube	E_{el} / E_s	$E_{el} = E_s$: Young's modulus determined by tensile coupon test
	σ_{yt} / σ_y	$\sigma_{yt} = \sigma_u$: tensile strength determined by tensile coupon test on steel tube
	$-\sigma_{yc} / \sigma_y$	$\sigma_{yc} = -0.75\sigma_y$: 75% of yield stress or design value of steel tube determined by tensile coupon test
	$-\varepsilon_{pl}^{U} / \varepsilon_y$	$\varepsilon_{pl}^{U} = -2\varepsilon_y$: twice the yield strain determined by tensile coupon test on steel tube
	χ	$\chi = \left(-\sigma_{yc} / \sigma_y\right)^{-1} = 1.33$
	$-\varepsilon_{pl}^{cr}$	$-\varepsilon_{pl}^{cr} = 0.3$
	ξ	$\xi = 0.05$
	m	$m = 2.4$
	κ	$\kappa = 0.3$
	r	$r = 1.4$
	η	$\eta = 2.5$
Stress-strain curve for in-filled concrete	E_{c0} / E_{c00}	$E_{c0} = 0.3E_{c00}$: 30% of Young's modus; E_{c00} is determined by concrete cylinder compression test
	$-E_{dc} / E_{c00}$	$E_{dc} = -E_{c00} / 1000$
	$\varepsilon_{cm} / 0.002$	$\varepsilon_{cm} = 0.008$
	$\sigma_{cm} / \sigma_{cc}$	$\sigma_{cm} = \sigma_{cc}$: strength determined by concrete cylinder compression test
	n	$n = 1.7$
	ω_d	$\omega_d = 1.0$

In the optimization, the search for the optimum parameter values was continued until the value of the object function Δ defined by Eq. (4-14) becomes less than 0.04. The number of calibration points taken on each hysteretic curve at every horizontal displacement increment of δ_0 amounted to around n_σ =150. The error of the horizontal force $\left|H_i^{FE} - H_i^{SE}\right|$ averaged over all the calibration points n_σ becomes less than 4% of the initial yield horizontal force H_0 defined by Eq. (4-16). Fig. 5-3 shows how the value of the objective function Δ for the column specimen CCFT4.0-1 is reduced to 0.04 with the increase in the number of iterations by the downhill-simplex method. The convergences are also illustrated in Fig. 5-4 for some of the parameters in the failure segment such as L_{se} / D_s, E_{el} / E_s and E_{c0} / E_{c00}. As can be seen from Fig. 5-3, the decreasing rate of Δ with respect to the number of iterations becomes very slow when Δ approaches 0.04. Therefore, the downhill-simplex method requires considerably large number of iterations to achieve the tolerance less than 0.04.

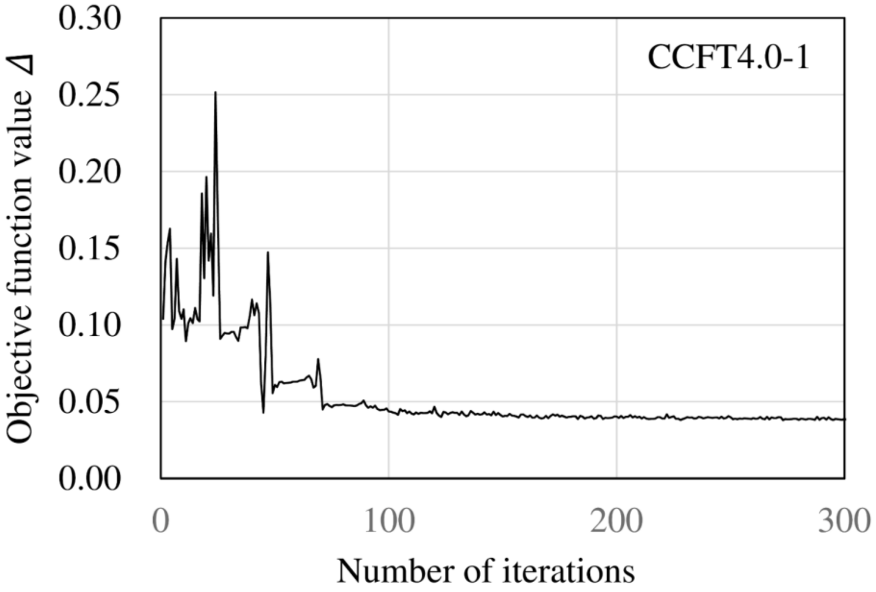

Fig. 5-3. Objective function value Δ vs. number of iterations

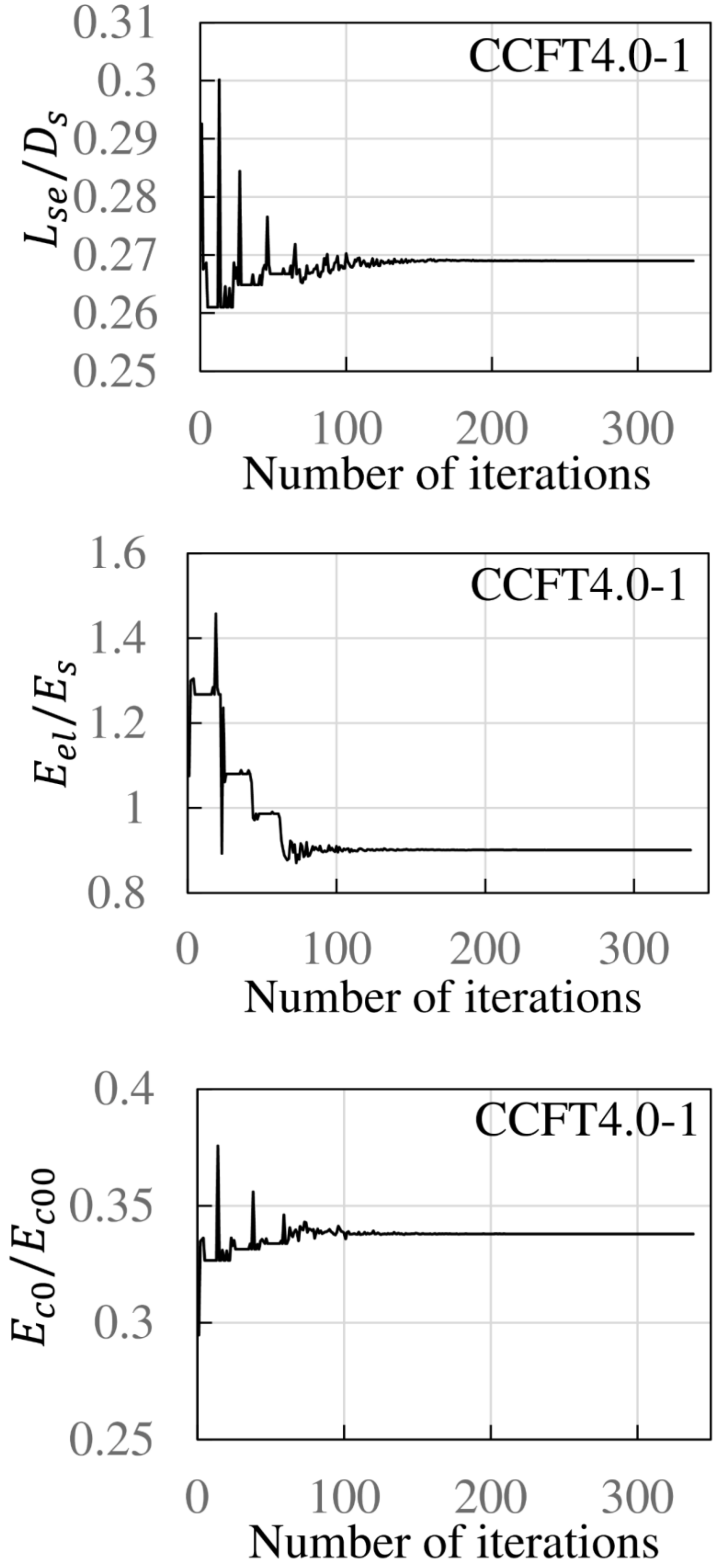

Fig. 5-4. Convergence of parameter values

The optimum parameter values of the failure segment obtained for the three types of the column models are summarized in Table. 5-3. The proposed fiber-based model with the failure segment has the nature of a curve-fitting model as well as that of a physical model. This implies that some parameters for the failure segment can be justified from physical consideration while the other parameters cannot be. Herein, appropriateness is discussed for some of the physical parameters identified by the optimization process. The effective local buckling length ratio L_{se} / D_s determined as 0.27 ~ 0.29 is approximately coincident with the length of the local buckling bulge of the steel tube that occurred at the lower part of the columns in the cyclic loading test. The initial elastic modulus ratio E_{c0} / E_{c00} of the in-filled concrete was determined as relatively smaller values around 0.3. This is due to an unavoidable initial gap existent between the steel tube and the in-filled concrete. This initial gap tends to reduce the stiffness of the PCFT columns. However, the effect of the initial gap cannot be simulated directly by the fiber-based model, being different from the shell-solid element model. Therefore, the initial elastic stiffness of the in-filled concrete E_{c0} was reduced in the optimization process to take into account the effect of the initial gap. The initial elastic stiffness ratio E_{el} / E_s of the steel tube identified as 0.7 for the hollow column model is somewhat smaller than those identified as $E_{el} / E_s = 0.9 \sim 1.0$ for the PCFT column models. This is because the axial stiffness of the steel tube for the hollow column is reduced by its local bending deformation while those for the PCFT columns are not reduced so much due to the restraint of the in-filled concrete.

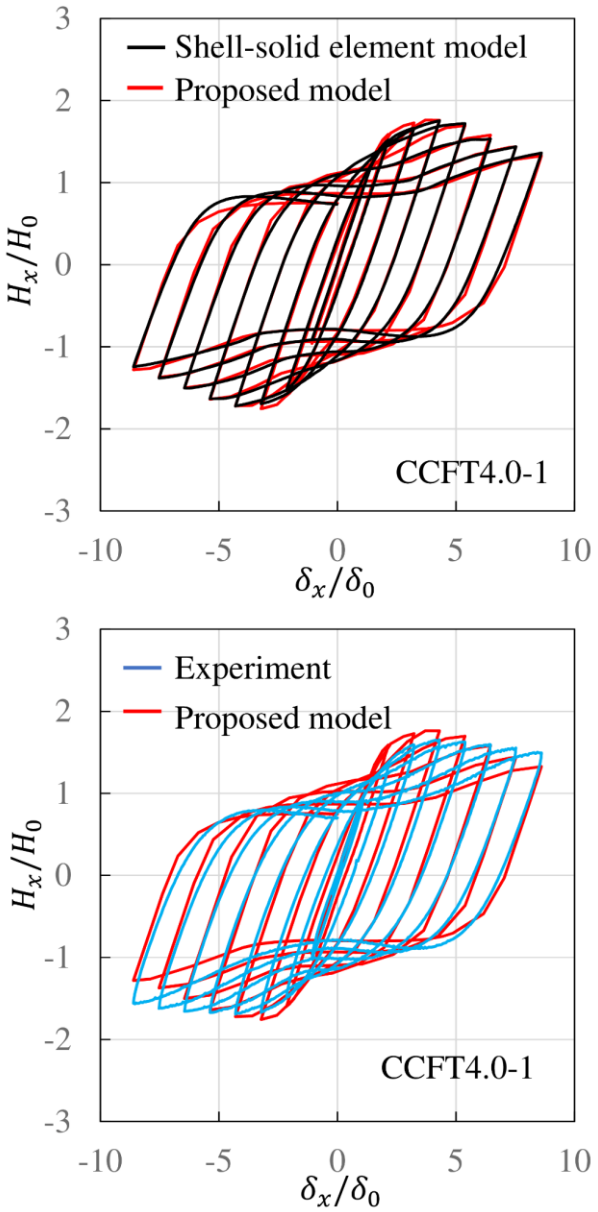
Shell-solid element model
Proposed model
CCFT4.0-1
H_x/H_0
δ_x/δ_0
3
2
1
0
-1
-2
-3
-10
-5
0
5
10
Experiment
Proposed model
CCFT4.0-1
H_x/H_0
δ_x/δ_0

(a) CCFT 4.0-1

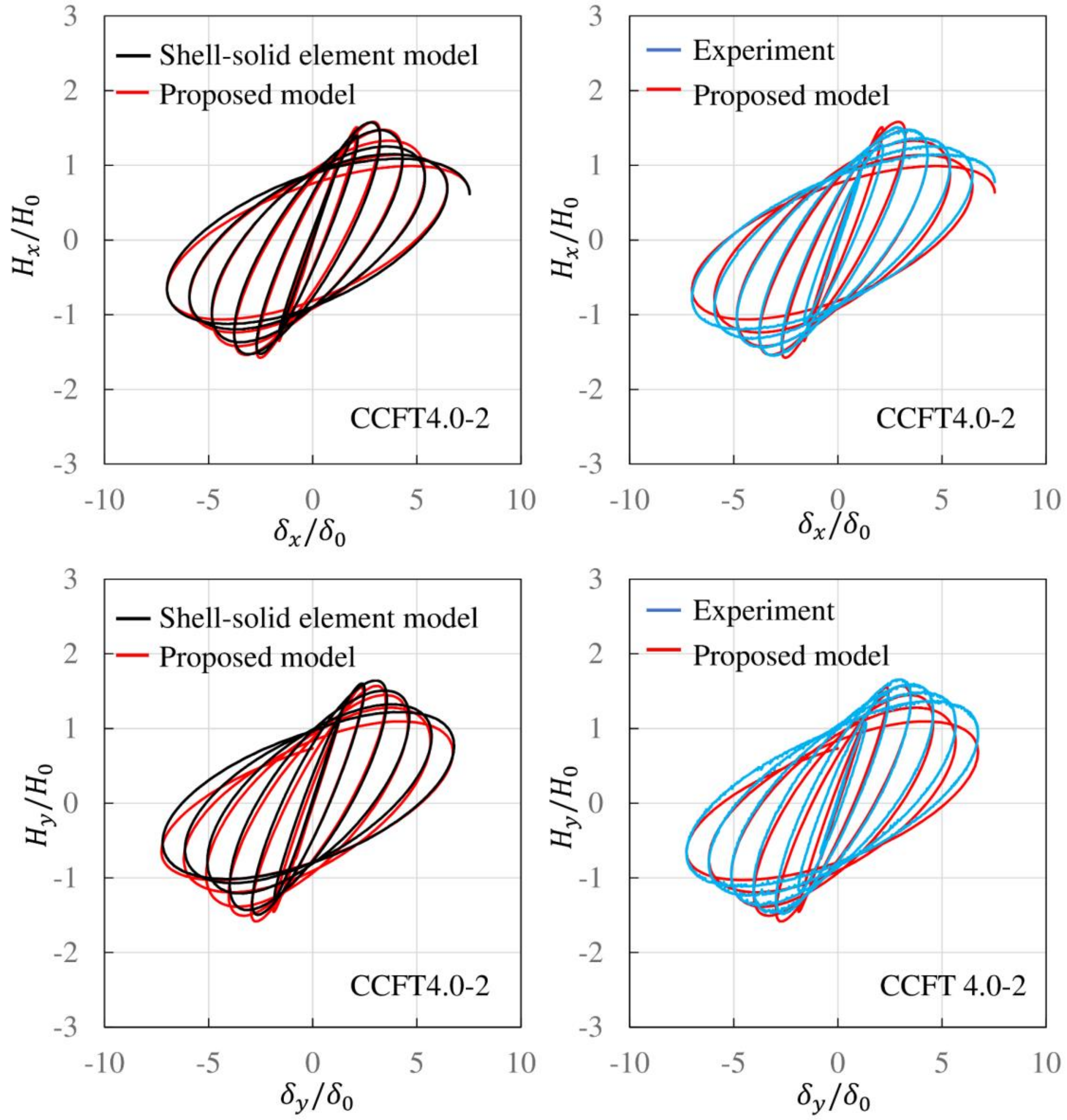
Shell-solid element model
Proposed model
Experiment
CCFT4.0-2
CCFT 4.0-2
H_x/H_0
H_y/H_0
δ_x/δ_0
δ_y/δ_0
3
2
1
0
-1
-2
-3
-10
-5
0
5
10

(b) CCFT 4.0-2

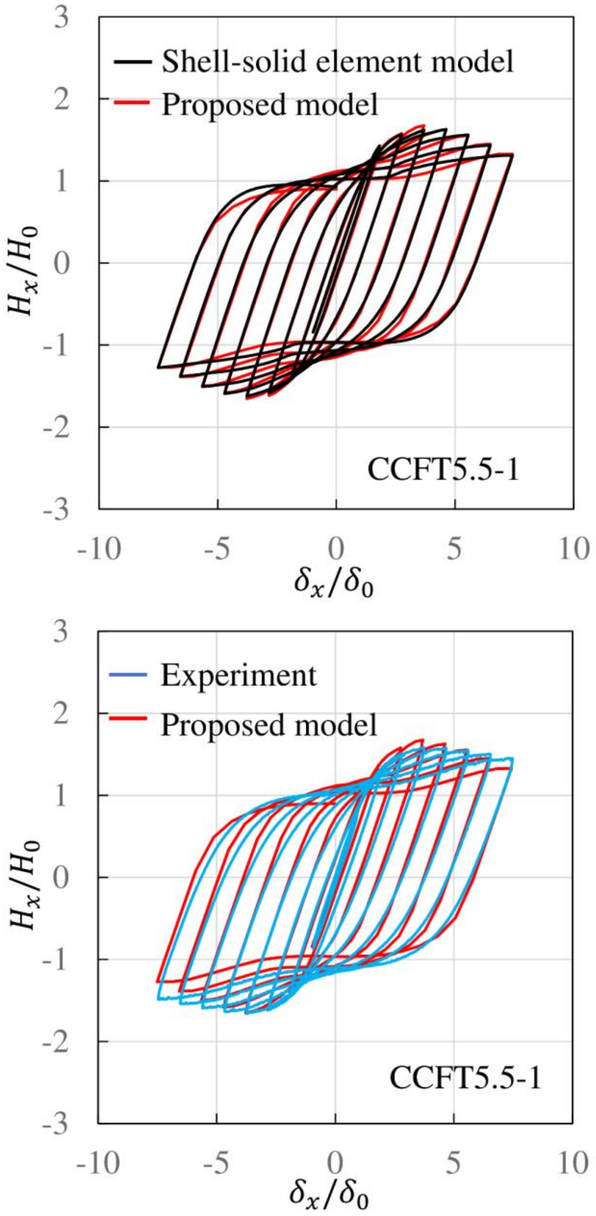
Shell-solid element model
Proposed model
CCFT5.5-1
H_x/H_0
δ_x/δ_0
3
2
1
0
-1
-2
-3
-10
-5
0
5
10
Experiment
Proposed model
CCFT5.5-1
H_x/H_0
δ_x/δ_0

(c) CCFT 5.5-1

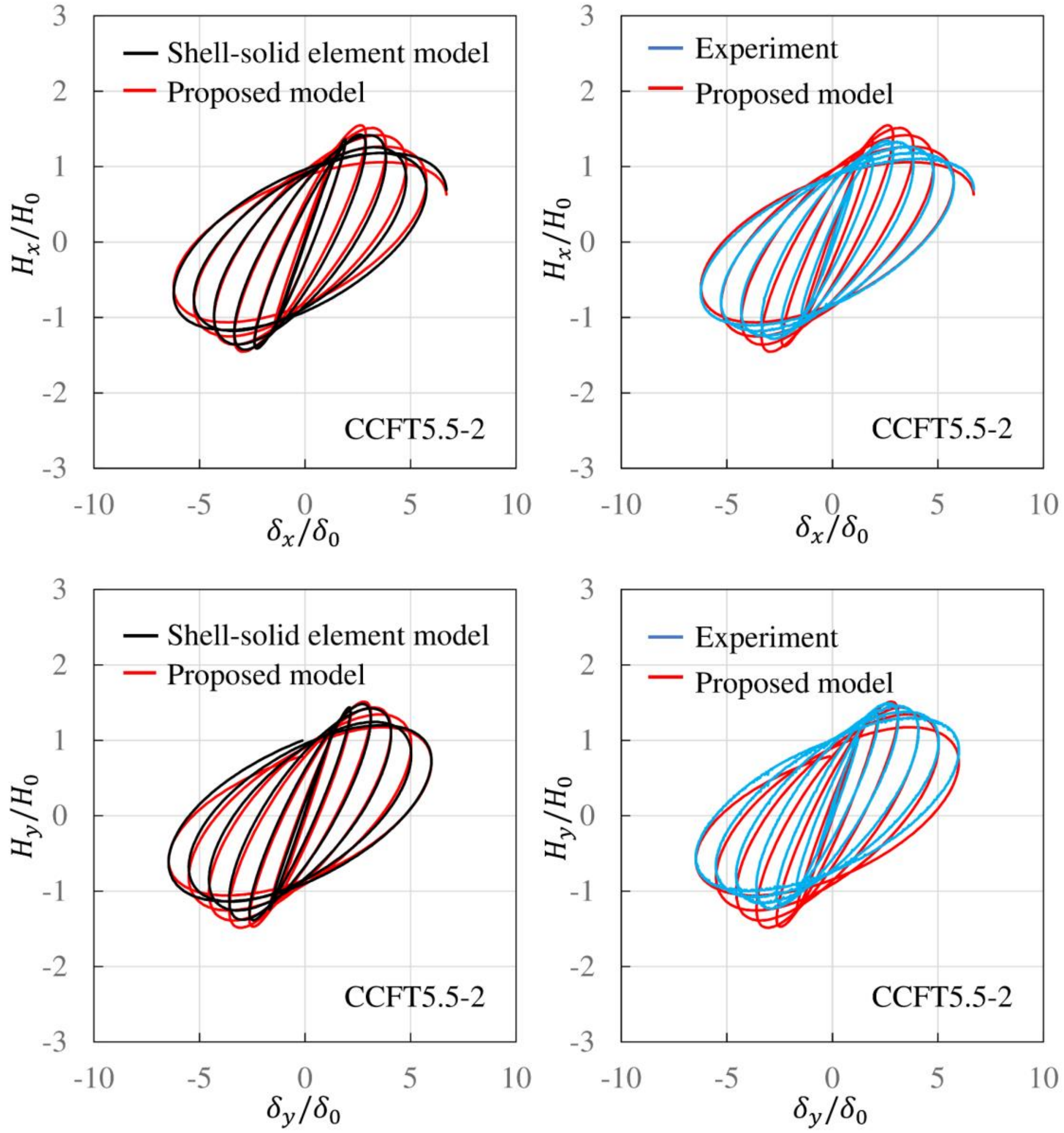
Shell-solid element model
Proposed model
Experiment
Proposed model
H_x/H_0
H_y/H_0
δ_x/δ_0
δ_y/δ_0
CCFT5.5-2
3
2
1
0
-1
-2
-3
-10
-5
0
5
10

(d) CCFT 5.5-2

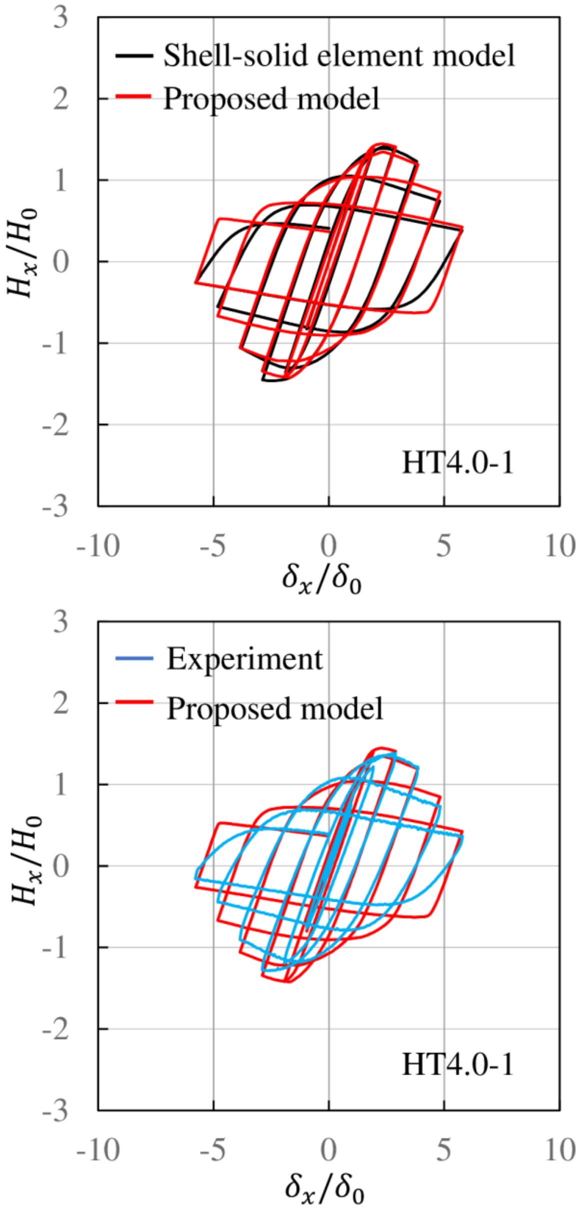
Shell-solid element model
Proposed model
HT4.0-1
H_x/H_0
δ_x/δ_0
3
2
1
0
-1
-2
-3
-10
-5
0
5
10
Experiment
Proposed model
HT4.0-1
H_x/H_0
δ_x/δ_0

(e) HT 4.0-1

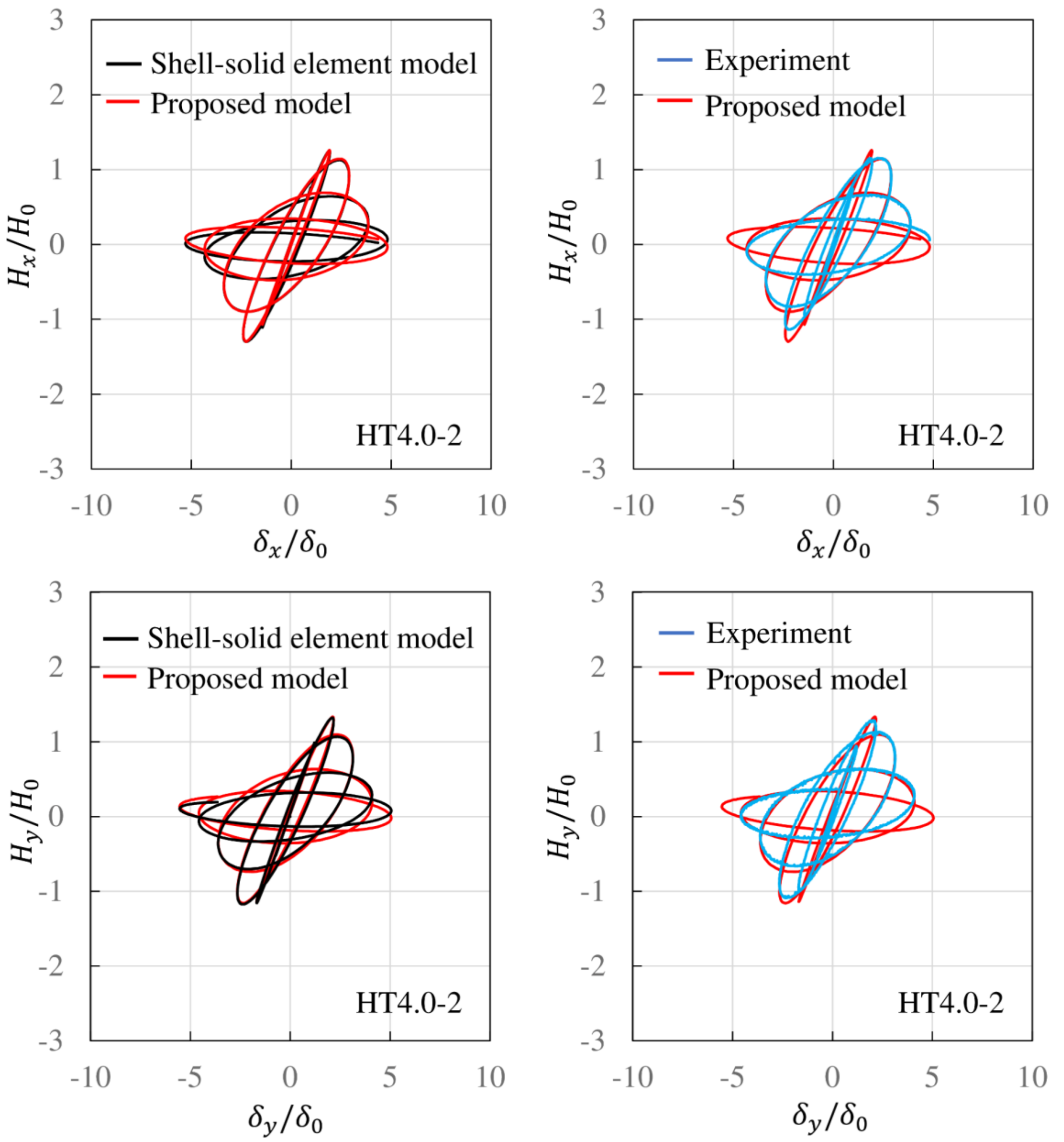

Note: Proposed model = Fiber-based model with failure segment

(f) HT 4.0-2

Fig. 5-5. Horizontal force-horizontal displacement relations of PCFT columns obtained by fiber-based model with failure segment, shell-solid element model and experiment

Finally, the fiber-based models with the optimum failure segment parameters shown in Table. 5-3 were employed to calculate the behavior of the PCFT column and HT column models subjected to the bidirectional spiral load illustrated in Fig. 5-2.

The results calculated by the fiber-based model with the failure segment are shown in Fig. 5-5, comparing to those obtained either by the experiment or by the shell-solid element model analysis in terms of the unidirectional and bidirectional cyclic horizontal force- horizontal displacement relations.

From the in-plane hysteretic curves of the specimens CCFT4.0-1 and CCFT5.5-1 shown in Figs. 5-5(a) and (c), it can be seen that the typical pinching hysteretic loop pattern observed in the experiment on the PCFT columns (Goto et al. (2010, 2014)) is precisely reproduced by the fiber-based model with the failure segment. In addition, their in-plane hysteretic curves calculated by the fiber-based model are coincident well with those obtained by the experiment. Regarding the HT column model, the comparison in terms of the in-plane hysteretic curve of the specimen HT4.0-1 illustrated in Fig. 5-5(e) shows that the fiber-based model with the failure segment can also be used for the analysis of the hollow steel columns where the post-peak deterioration due to the local buckling deformation is significant. It should be noted in the analysis of the HT column model that the fiber-based model with the failure segment does not include the truss elements (Fig. 4-3) representing the in-filled concrete.

The fiber-based model with the failure segment adopts the parameter values determined by the target in-plane hysteretic curves of the columns calculated by the shell-solid element model analysis. Applicability of these parameter values to the analysis under the bi-directional horizontal spiral loads is examined based on the hysteretic curves of the specimens CCFT4.0-2, CCFT5.5-2 and HT4.0-2 shown in Figs.

5-5(b), (d) and (f). From these figures, the hysteretic curves of the fiber-based model analysis are observed to coincide well with those of the shell-solid element model analysis and the experiments. Therefore, it may be summarized that the fiber-based model with the parameters determined from the in-plane hysteretic curves of the PCFT and HT columns can be used to analyze their multidirectional behavior with the accuracy comparable to that of the shell-solid element model analysis.

Table 5-3. Identified parameter values for failure segment used in the analysis of cyclic loading tests on single PCFT and HT columns

Parameters		CCFT4.0(CFT)	CCFT5.5(CFT)	HT4.0(Hollow)
Geometrical parameter of locally buckled part	L_{se} / D_s	0.269	0.291	0.274
Stress-strain curve for locally buckled part of steel tube	E_{el} / E_s	0.901	1.065	0.698
	σ_{yt} / σ_y	1.291	1.335	0.815
	$-\sigma_{yc} / \sigma_y$	0.737	0.714	1.095
	$-\varepsilon_{pl}^{U} / \varepsilon_y$	1.739	1.650	4.438
	χ	1.357	1.370	0.983
	$-\varepsilon_{pl}^{cr}$	0.300	0.300	0.300
	ξ	0.050	0.059	0.267
	m	1.958	1.701	3.725
	κ	0.281	0.319	0.201
	r	1.265	1.131	0.797
	η	1.958	2.649	2.046
Stress-strain curve for in-filled concrete	E_{c0} / E_{c00}	0.338	0.285	—
	$-E_{dc} / E_{c00}$	0.001	0.001	
	$\varepsilon_{cm} / 0.002$	4.419	4.104	
	$\sigma_{cm} / \sigma_{cc}$	0.909	1.029	
	n	1.973	1.848	
	ω_d	0.981	0.853	

5.3 Shake table test on single CFT columns

Uni-directional and bi-directional shake table tests were conducted on the PCFT column specimens, respectively, denoted as CCFT3.5-1 and CCFT3.5-2. Detailed test setup and material properties of specimens can be found elsewhere (Goto et al. (2014)).

The longitudinal (LG) and transverse (TR) acceleration components of the Tsugaru wave observed at the Tsugaru bridge during the 1983 Nihonkai-chubu earthquake were selected as original earthquake wave components for the input acceleration wave. Bi-directional input acceleration components for the shake table tests were prepared by modifying these original wave components. Firstly, their time axis was shortened to $1/\sqrt{s}$ such that the PCFT column specimens with the scale factor($1/s=1/8$) exhibits the response of the real-sized columns. Secondly, the amplitudes of the input wave components were equally increased to 300% of their original amplitudes. These increased amplitudes of the input acceleration components are strong enough to cause the PCFT column specimens to exceed their ultimate states. In the test, the LG and TR directions of the observed acceleration waves were assumed to coincide with the x- and y- axes, respectively. In the case of the unidirectional shake table test, the y- component of the prepared acceleration wave was used. The parameter values of the fiber-based model with the failure segment employed in the analysis of the shake table test were calibrated by the procedure shown in Fig. 4-8, referring to the in-plane hysteretic curve of each specimen obtained by the shell-solid element analysis. In this calibration, the optimization of the parameter values was continued until the value of Δ evaluated by

Eq. (4-14) became less than 0.04. The applicability of the fiber-based model with the failure segment to the dynamic analysis of the PCFT columns under seismic accelerations was examined by the comparison of its numerical results to the results obtained either by the shake table tests on the specimens CCFT3.5-1 and CCFT3.5-2. As an example, the numerical results of the fiber-based model are herein compared to the bidirectional shake table test results on the column specimen CCFT3.5-2 in Figs.5-6 and 5-7 in terms of the time-history responses of the bidirectional sway displacement components (δ_x, δ_y) and the bi-directional equivalent horizontal force-sway displacement relations $(H_x^{eq} - \delta_x,\ H_y^{eq} - \delta_y)$, respectively. All the physical quantities shown in these figures are those at the top of the columns. The definition of the equivalent horizontal force components (H_x^{eq}, H_y^{eq}) is shown elsewhere Goto et al (2010,2014). From Figs.5-6 and 5-7, it can be said that the fiber-based model with the failure segment can be applied to assess the 3D ultimate seismic behavior of the PCFT columns with an accuracy comparable to that of the shell-solid element model.

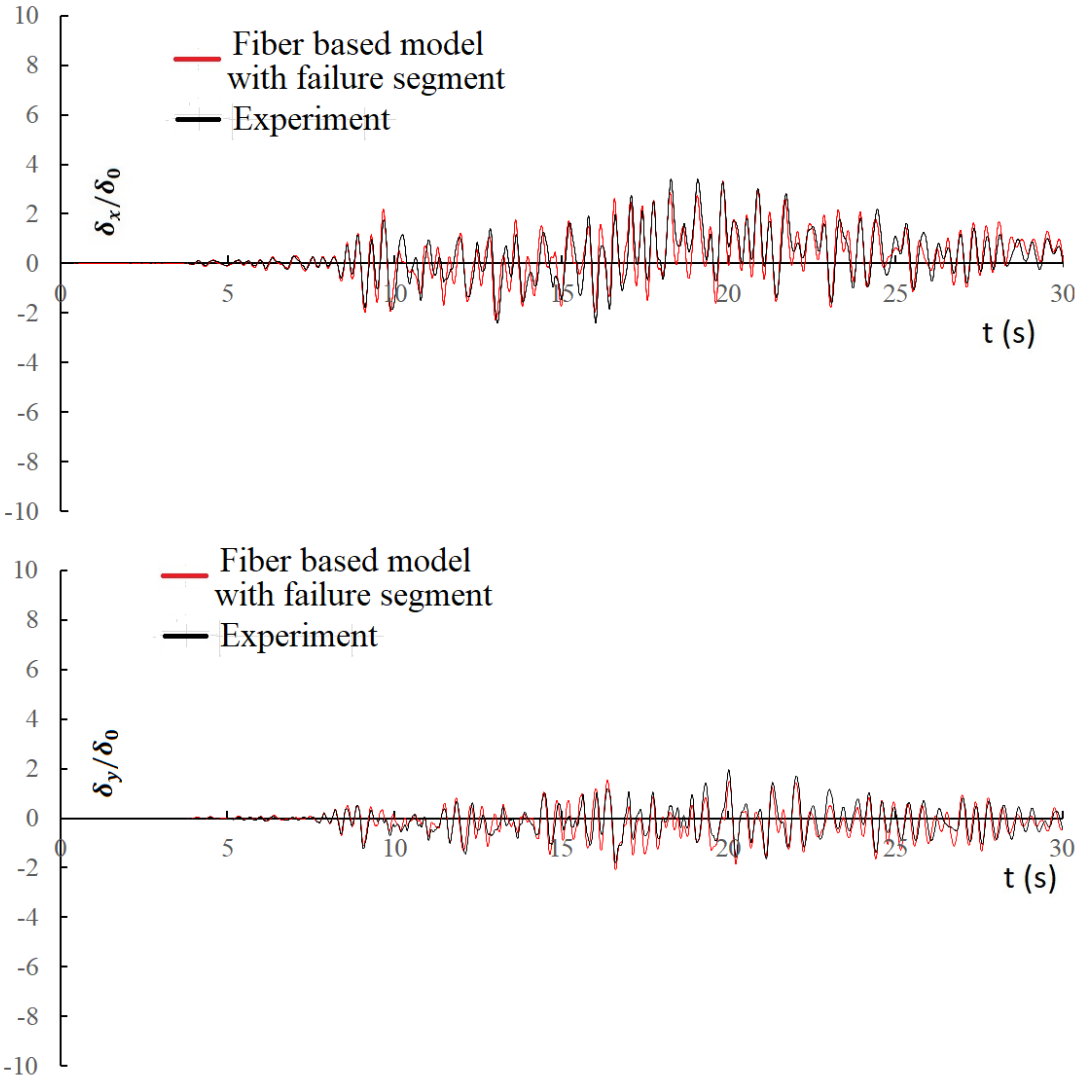

Fig. 5-6. Time history curves of displacement of top of column in bi-directional shaking table test and comparison of analysis employing fiber-based model with failure segment

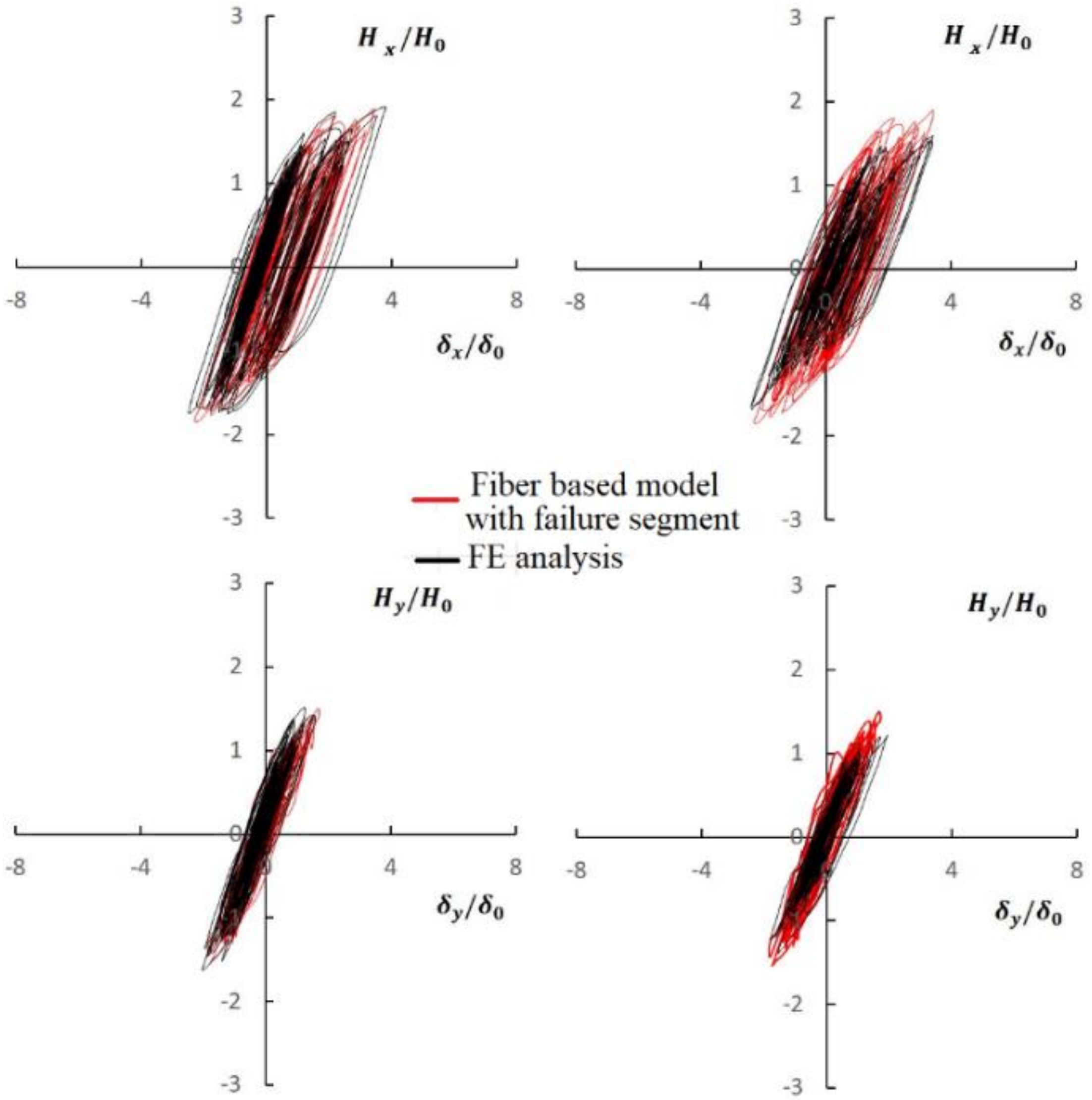

Fig. 5-7. Hysteretic curves of PCFT column in bi-directional shaking table test and comparison of analysis employing fiber-based model with failure segment

5.4 Shake table test on the two-span elevated-girder bridge model with multiple PCFT piers

The accuracy and numerical efficiency of the fiber-based model with the failure segment were examined for a realistic case when applied to the seismic analysis of entire elevated-girder bridge systems with multiple PCFT piers. For this purpose, the results of a relatively large-scale shake table test on a 2-span continuous elevated-girder bridge model supported by three PCFT piers were used as a reference data. The details of this shake table test shown in Fig. 5-8(a) is explained elsewhere (Goto et al. (2017)). The test model was determined by scaling down a prototype existing bridge model by a factor of $1/s = 1/6.7$. The superstructure of the test model had three cross girders with equal distance. Each of these cross girders was supported by two rubber bearings located on the cross beam of each pier. The superstructure as well as the rubber bearings were designed not to be damaged before the PCFT piers reach their ultimate states. This design concept conforms to the current Japanese seismic design code for highway bridges (Japan Road Association 2012). Eleven sets of weights made of steel slabs were installed on the upper surface of the superstructure such that the initial axial force ratio of the center pier P2 and that of the end piers, P1 and P3, might become $P/(\sigma_y A_s) =$ 0.12 and 0.08, respectively. These initial axial force ratios were determined, following the assumed test scenario that the damage might first occur in the column of the center pier and, then, propagate to the columns of the end piers. Geometrical and material properties of the PCFT piers (Fig. 5-8(b)) are summarized in Table 5-4.

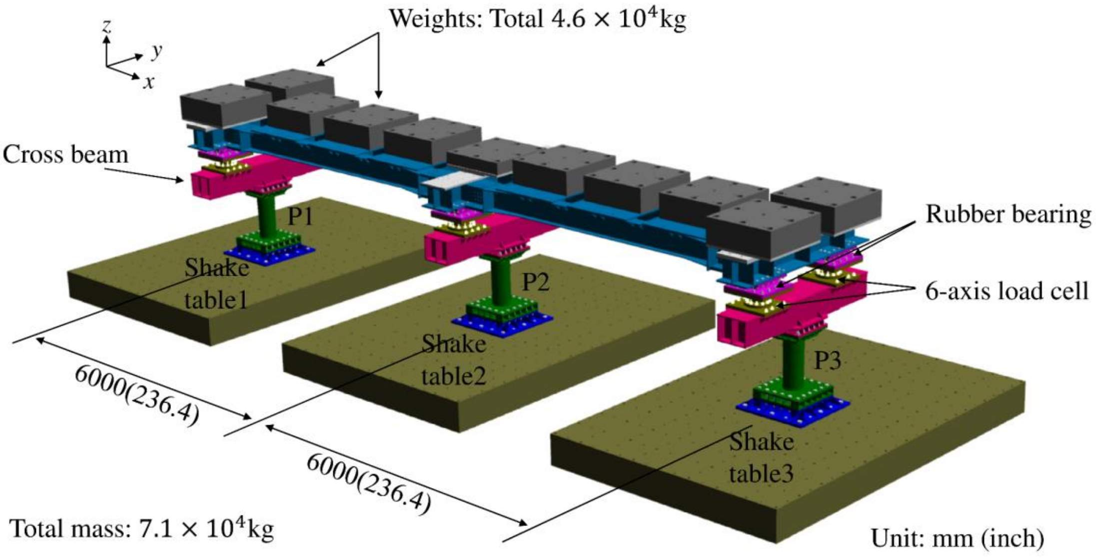

(a) Test setup

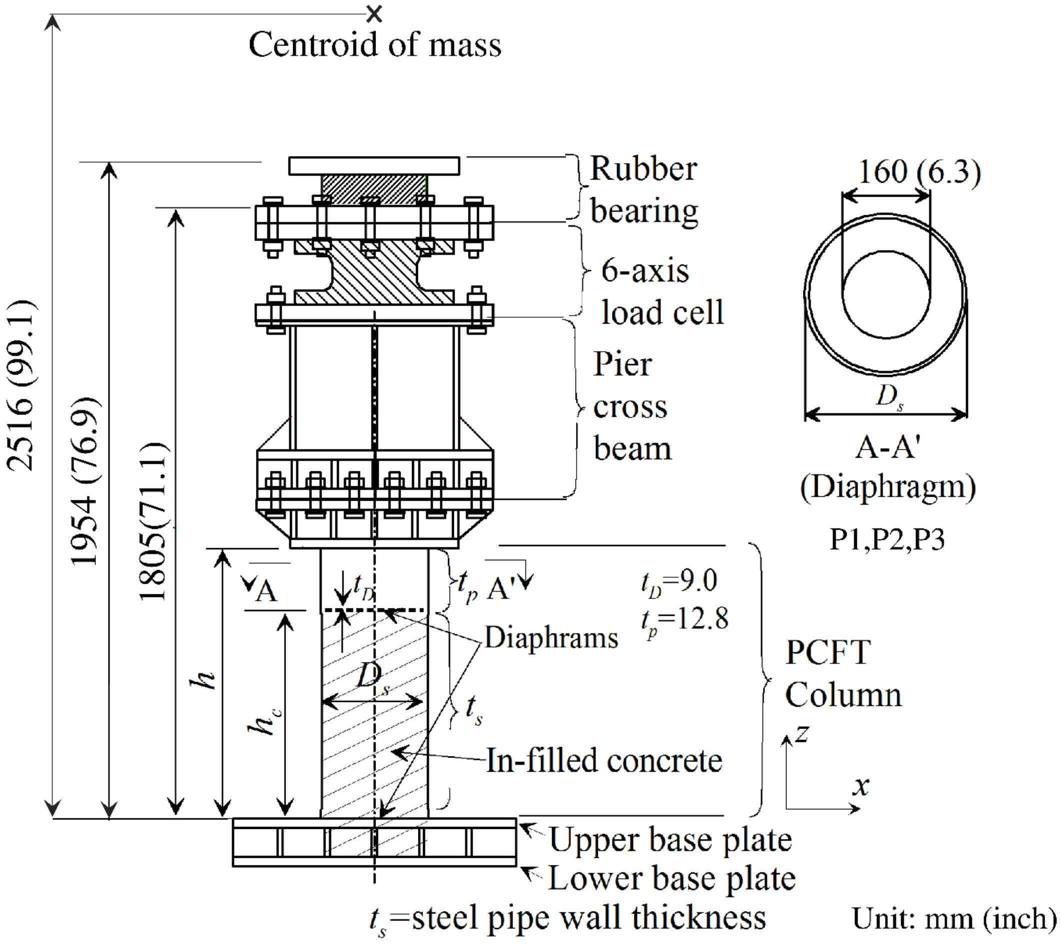

(b) PCFT pier (P1, P2, P3)

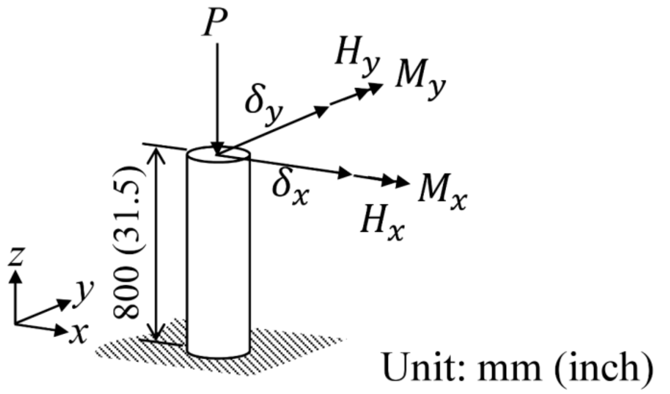

(c) Definition of force, moment and displacement components of piers

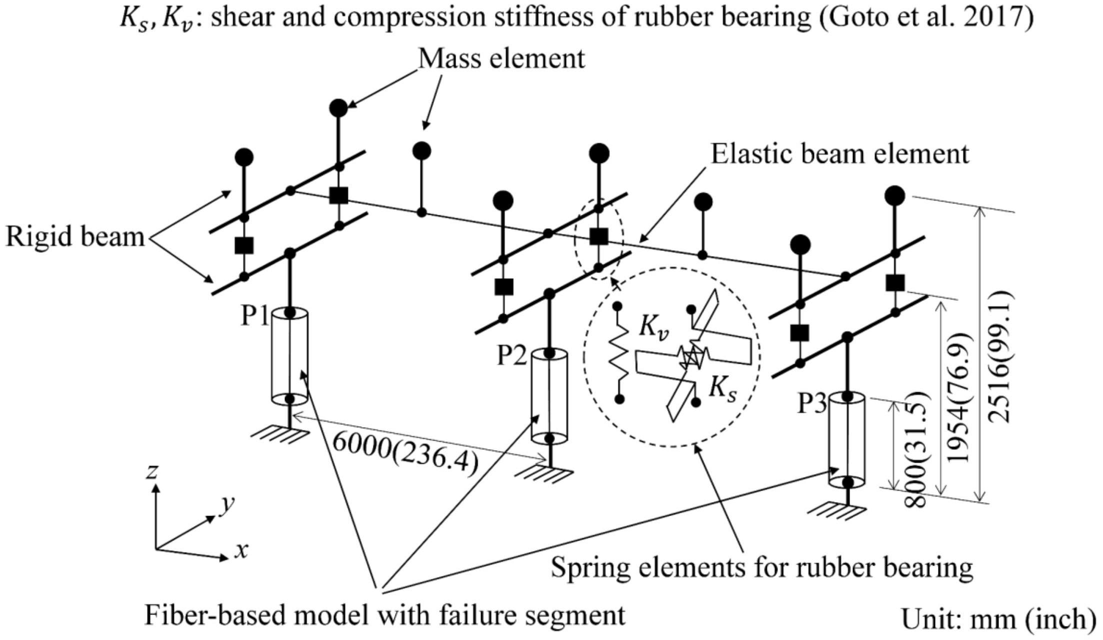

(d) Modelling of entire bridge system by fiber-based model with failure segment

Fig. 5-8. Test setup and modeling of shake table test on two-span continuous elevated-girder bridge model supported by three thin-walled PCFT piers

The longitudinal (LG) and transverse (TR) acceleration components of the Tsugaru wave observed at the Tsugaru bridge during the 1983 Nihonkai-chubu earthquake were selected as original earthquake wave components used for the input acceleration wave. Bi-directional input acceleration components for the shake table tests were prepared by modifying these original wave components. First, their time axis was shortened to $1/\sqrt{s}$ such that the PCFT piers with the scale factor of $1/s = 1/6.7$ exhibit the response of the real-sized columns. Second, the amplitudes of the input wave components were equally increased to 400% of their original amplitudes. These increased amplitudes of the input acceleration components are strong enough to cause the PCFT piers to exceed their ultimate states. The LG and TR components of the modified Tsugaru wave were simultaneously applied to the three pier bases without phase difference in the directions of the *x*- and *y*- axis (Fig. 5-8(a)), respectively.

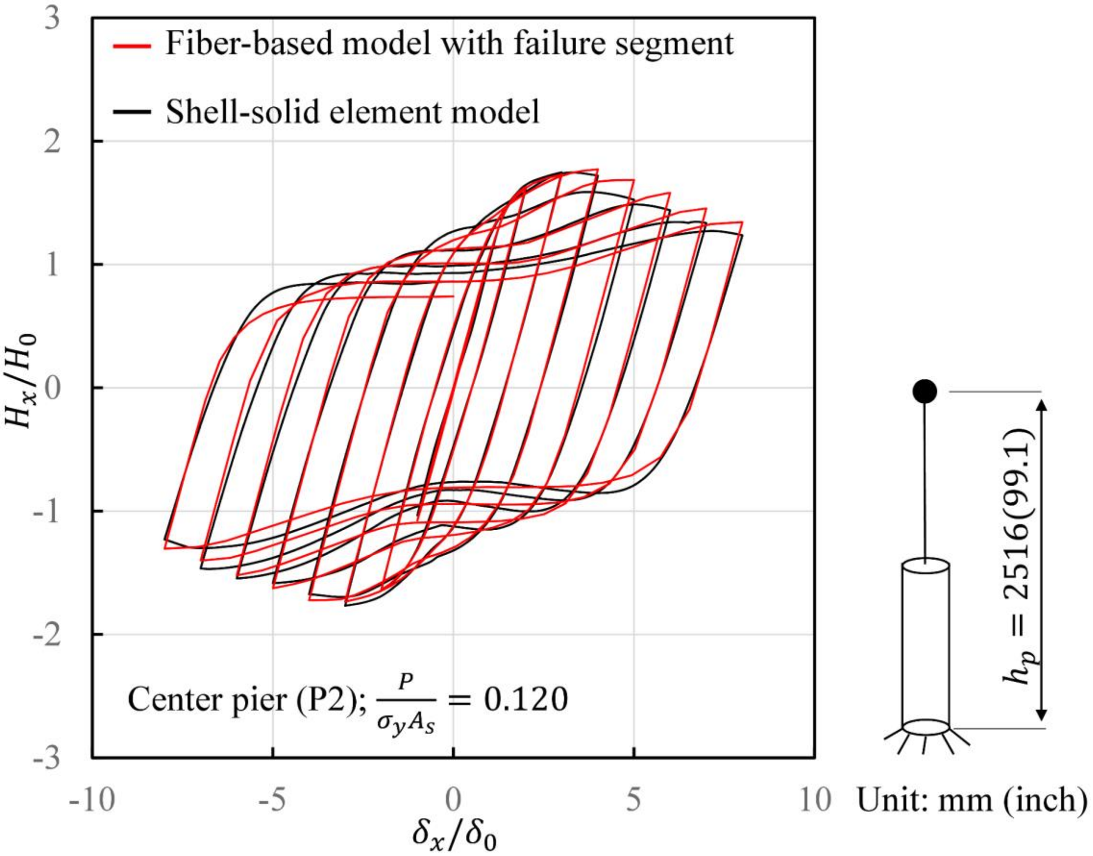

(a) Center pier

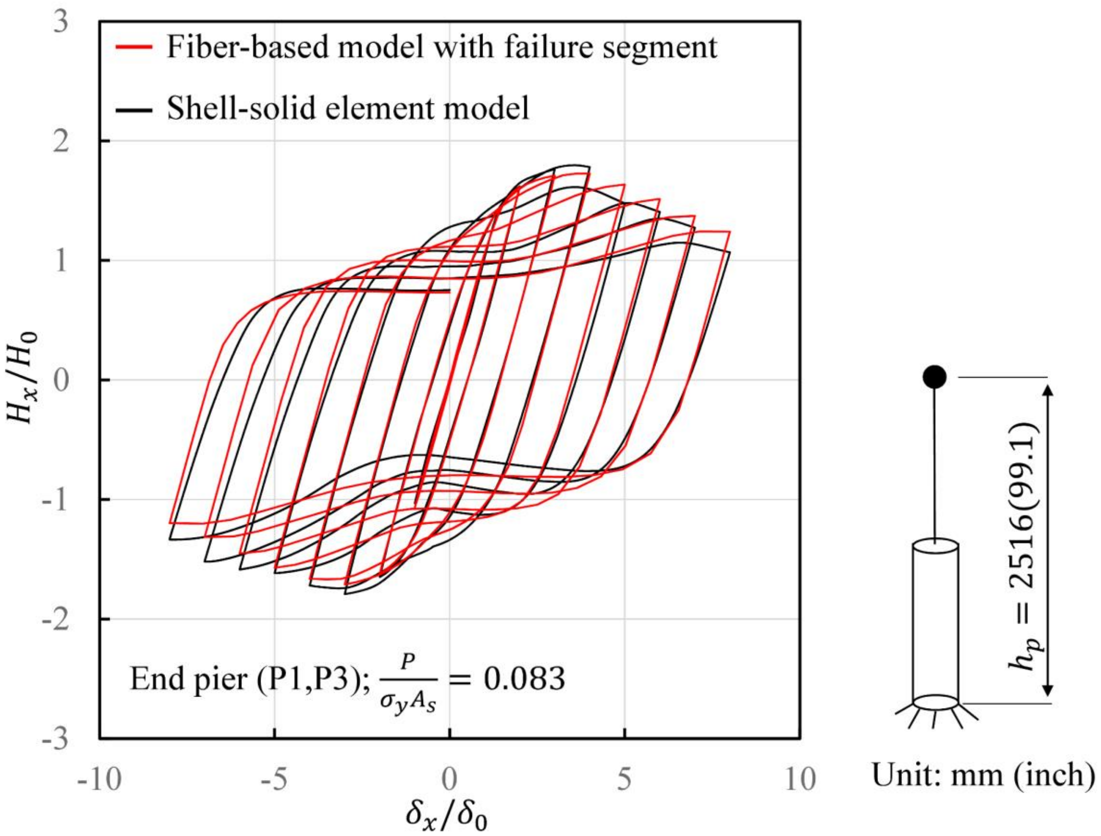

(b) End pier

Fig. 5-9. In-plane horizontal force-horizontal displacement relations of single PCFT piers obtained by fiber-based model with failure segment and shell-solid element model

In the analysis of the elevated-girder bridge model supported by the multiple PCFT piers, the failure segment was used to represent the concrete-filled parts of the piers. In an exact sense, the parameter values of the failure segment at the center pier are different from those of the end piers because the axial force ratio of the center pier ($P/(\sigma_y A_s) = 0.12$) is larger than those of the end piers ($P/(\sigma_y A_s) = 0.08$). This implies that the parameter values of the failure segments have to be identified for the center and end piers independently in an exact sense, based on their respective in-plane hysteretic curves calculated by the shell-solid element model analysis. In the present case, however, the center and end piers had the same column size and their axial force ratios were not so much different. Therefore, for simplicity, the parameter values of the failure segments identified for the center pier were herein assumed to be applicable to those of the end piers. The parameter identification procedure follows the flow chart shown in Fig. 4-8. The height of the center pier model used for this parameter identification was assumed to be $h_p = 2516$ mm. The top of this pier model corresponds to the location of the center of the masses installed to the superstructure (Fig. 5-8(a)). For parameter identification, the down-hill simplex method was employed as optimization method with the initial parameter values shown in Table 2. The search for the optimum parameter values was continued until the value of Δ evaluated by Eq. (4-14) became less than 0.04. The optimum parameter values so identified are shown in Table 5-5. To demonstrate the validity of the failure segment with the identified parameter values, the in-plane hysteretic curves of the end and center piers computed by the fiber-based model with the failure segment are compared in Fig. 5-9 to those obtained by the shell-solid element model. It can be confirmed from this figure that the parameter values of the failure segment identified by the hysteretic curve of the center pier are also applicable to those of the end piers.

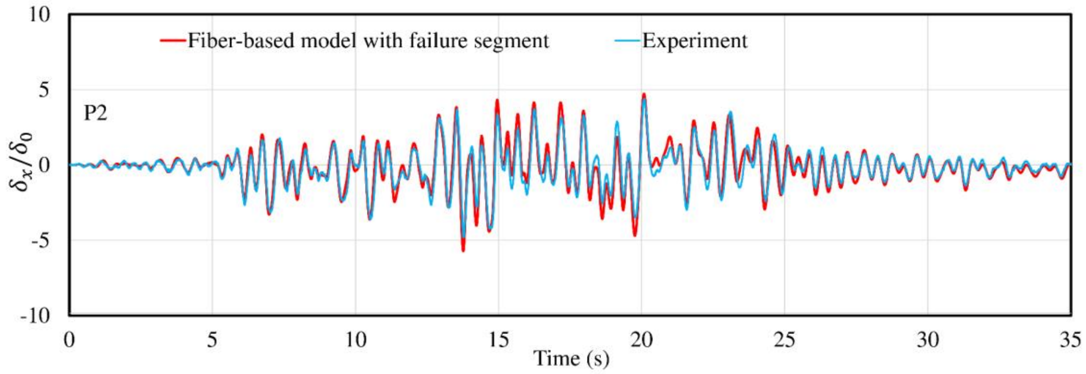

(a) Longitudinal component

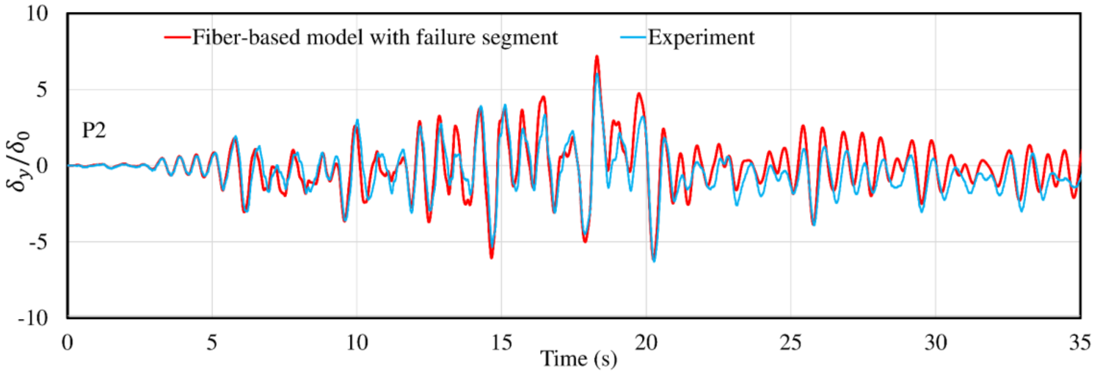

(b) Transverse component

Fig. 5-10. Time history responses of sway displacement components of PCFT piers at the height of *h*=800(mm) of PCFT piers

The modeling of the entire bridge system by the use of the fiber-based model is briefly illustrated in Fig. 5-8(d). The modeling of the PCFT piers is the same as that shown in Fig. 3. That is, the lower part of the piers with the in-filled concrete was represented by the failure segments, while the hollow part was expressed by the conventional 3D Timoshenko beam elements. The superstructure was expressed by 3D elastic Timoshenko beam elements. Each rubber bearing installed on the cross beams of the piers was represented by bidirectional horizontal shear springs and one vertical spring. The constants of these springs were determined by static loading tests on the rubber bearings. The details of the loading tests including the spring constants are shown elsewhere (Goto et al. (2017)).

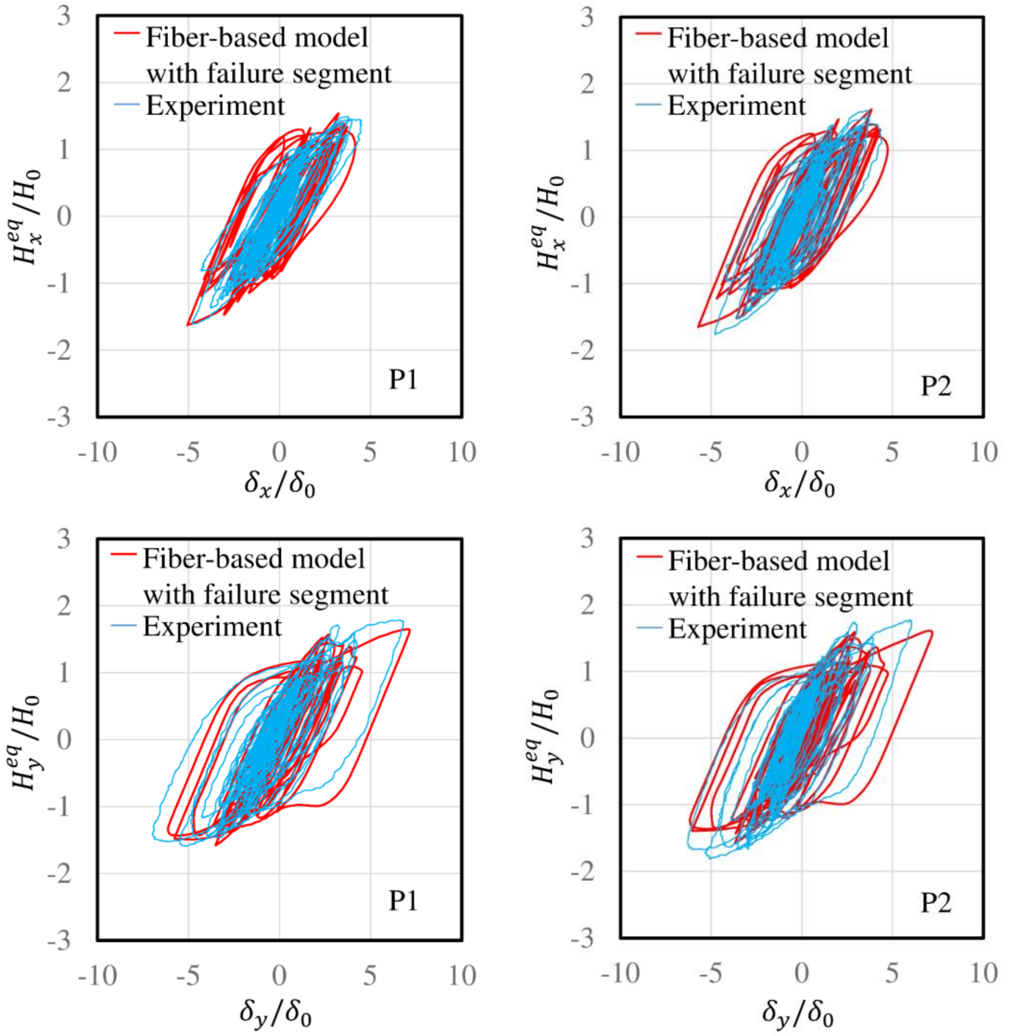

(a) P1 (b) P2

Fig. 5-11. Equivalent horizontal force-horizontal displacement component relations at the height of *h*=800(mm) of piers

The results obtained numerically by the proposed fiber-based model and those of the shake table test are schematically shown in Figs. 5-10 and 5-11 in terms of the response physical quantities of the respective piers at the height of $h = 800\,\mathrm{mm}$ (Fig. 14(c)): histories of the bidirectional sway displacement components and the bi-directional equivalent horizontal force-sway displacement component relations (Goto et al. (2017)). In these figures, the numerical results of the shell-solid element model analysis are not shown for comparison because this analysis failed due to its extremely poor convergence, when applied to calculate the nonlinear response of the entire bridge system.

Table 5-4. Geometric and material properties of PCFT column specimens used for shake table test on 2-span elevated-girder bridge model supported by PCFT piers

Specimen <pipe material>	D_s (mm)	h (mm)	t_s (mm)	h_c (mm)	R_t	$\bar{\lambda}$	$\frac{P}{\sigma_y A_s}$	H_0 (kN)	δ_0 (mm)	Load pattern
P1 (CFT) <STK490>	310.00	795	4.89	624	0.129	0.235	0.083	207	3.05	400% Tsugaru (LG+TR)
P2 (CFT) <STK490>	311.00	801	5.02	627	0.126	0.236	0.120	204	3.01	
P3 (CFT) <STK490>	310.00	797	4.87	626	0.130	0.236	0.081	207	3.05	

From Figs. 5-10 and 5-11, it can be seen that the fiber-based model with the failure segment has enough accuracy to simulate the ultimate behavior of the multiple PCFT piers in the elevated-girder bridge systems subjected to multi-directional seismic accelerations. Furthermore, under the computing environment using the parallel computing with four cores of Intel Xeons E5-2697 v2 processor, the fiber-based model with the failure segment analysis took no more than 10 minutes to simulate the ultimate behavior of the entire 2-span continuous elevated-girder bridge model from the beginning to the end of the shake table test. In contrast, the shell-solid element model analysis failed to obtain convergent solutions at a very early stage and its computation time could not be directly compared with that of the proposed fiber-based model.

Therefore, the numerical simulation of the shake table test on single PCFT columns (Goto et al. (2014)) was used to examine the computation time of the shell-solid model element analysis. From this simulation, it was revealed that the shell-solid element model analysis took an extraordinary long computation time of no less than 10 days due to the poor convergence of its iteration process. Although the fiber-based model with the failure segment may need somewhat long time such as 4 hours to optimize all the parameters of the failure segment, this time may be drastically reduced by using appropriate initial values in the optimization process. The existing available parameter values for the PCFT columns with approximately the same structural parameter values may be used as these initial values.

As discussed above, the fiber-based model with the failure segment has an excellent computational efficiency as well as accuracy. In view of these excellent features of the fiber-based model with the failure segment, it will be possible to employ this model in a practical and advanced seismic design to assess directly the ultimate behavior of the entire bridge systems supported by multiple PCFT piers.

5.4 Summary and concluding remarks

The thin-walled partially concrete-filled tubular steel columns referred to as thin-walled PCFT columns have an excellent seismic performance. To reflect this excellent seismic performance in design, it is essential to provide some analysis method to assess their ultimate behavior accurately by considering the cyclic local buckling of the outer steel tube, the behavior of the confined in-filled concrete and the interface action between the steel tube and the in-filled concrete. Up to the present, the shell-solid element model has been the only numerical model that can be used to consider these characteristic behaviors of the thin-walled PCFT columns in a direct manner. However, the use of the shell-solid element model requires unrealistically long computation time and often encounters numerical difficulty to obtain convergent solutions, when applied to large structural systems with multiple thin-walled PCFT piers.

The objective of the present research is to propose a practical 3D fiber-based model with the failure segment that is computationally efficient, yet accurate enough to assess the ultimate behavior of the PCFT columns. This model is characterized by the point that the failure segment calibrated by the in-plane hysteretic behavior of the PCFT columns are applicable to assess the ultimate 3D behavior of the PCFT columns under arbitrary multi-directional seismic accelerations. The accuracy and numerical efficiency of the fiber-based model with the failure segment were investigated extensively by comparing its numerical results to those obtained either by the shell-solid element model analysis or by tests, such as the cyclic loading tests and shake table tests on single PCFT columns, and the multi-shake table test on a two-span elevated-girder bridge system with multiple PCFT piers. From the above investigation, it was demonstrated that the proposed fiber-based model with the parameters determined from the in-plane hysteretic curves of the PCFT columns can be used to analyze their multidirectional behavior with the accuracy comparable to that of the shell-solid element model analysis. In addition, the use of the fiber-based model with the failure segment dramatically improves the numerical efficiency in the analysis of the PCFT columns. In view of these excellent features of the proposed fiber-based model, it will be possible to employ this model in a practical seismic design to assess directly the ultimate behavior of the entire bridge system supported by multiple PCFT piers.

Last but not least, the proposed fiber-based model with the failure segment has less restrictions in its modeling and parameter calibration. Therefore, this model is considered to be applicable to wider range of CFT structures, so far as accurate in-plane hysteretic curves are available for the corresponding CFT members. However, the failure segment formulated in this paper is primarily intended for the analysis of the members where bending behavior is dominant. Therefore, some further improvement in its modeling is necessary to apply the proposed model to CFT members where the effect of shear behavior cannot be ignored.

Table 5-5. Identified parameter values for failure segment used in the analysis of shake table test on elevated girder bridge model supported by PCFT piers

Parameters		P1, P2, P3
Geometrical parameter of locally buckled part	L_{se} / D_s	0.293
Stress-strain curve for locally buckled part of steel tub	E_{el} / E_s	1.075
	σ_{yt} / σ_y	1.269
	$-\sigma_{yc} / \sigma_y$	0.707
	$-\varepsilon_{pl}^{U} / \varepsilon_y$	1.586
	χ	1.371
	$-\varepsilon_{pl}^{cr}$	0.300
	ξ	0.056
	m	1.844
	κ	0.847
	r	1.245
	η	2.517
Stress-strain curve for in-filled concrete	E_{c0} / E_{c00}	0.295
	$-E_{dc} / E_{c00}$	0.001
	$\varepsilon_{cm} / 0.002$	4.360
	$\sigma_{cm} / \sigma_{cc}$	0.910
	n	1.721
	ω_d	0.847

Appendix. A

Database of experiments for CFT columns subjected to axial force and lateral cyclic load available in the literature

Ref.	section type	specimen ID	h (mm)	h_c (mm)	D (mm)	t (mm)	σ_y (MPa)	σ_c (MPa)	P (kN)	M_u (kN•m)
Fujii (2000)	circular	case-A	1800	1800	216.3	4.5	400	31	267	49.26
		case-B	1800	1800	216.3	4.5	400	31	267	45.75
		case-C	1800	1800	216.3	4.5	400	31	267	49.53
		case-D	1800	1800	216.3	4.5	400	31	267	45.92
		case-E	1800	1800	216.3	4.5	400	31	534	53.07
Liu et al. (2008)	rectangular	CCFT1	1100	1100	150	2.65	328	35.2	662	88.00
		CCFT2	1100	1100	150	2.65	328	35.2	452	82.17
		CCFT3	1100	1100	150	4.82	340	35.2	592	134.75
		CCFT4	845	845	150	2.65	328	35.2	452	92.36
		CCFT5	1100	1100	150	2.65	328	35.2	452	86.35
		HCFT1	1100	1100	150	4.78	317	81.4	1300	180.51
		HCFT2	1100	1100	150	2.89	319	81.4	1300	138.38
		HCFT3	1100	1100	150	2.89	319	81.4	1000	143.44

Ref.	section type	specimen ID	h (mm)	h_c (mm)	D (mm)	t (mm)	σ_y (MPa)	σ_c (MPa)	P (kN)	M_u (kN•m)
		HCFT4	800	800	150	2.89	319	81.4	1000	128.32
Varma et al. (2004)	rectangular	CBC-32-80-10	1500	1500	305.181	8.9	600	110	1523	926.00
		CBC-32-80-20	1500	1500	305.181	8.9	600	110	3050	954.00
		CBC-48-80-10	1500	1500	305	6.1	660	110	1355	645.00
		CBC-48-80-20	1500	1500	305	6.1	660	110	2715	712.00
		CBC-32-46-10	1500	1500	303.494	8.6	269	110	1255	553.00
		CBC-32-46-20	1500	1500	303.494	8.6	269	110	2515	606.00
		CBC-48-46-10	1500	1500	302.586	5.8	471	110	1178	512.00
		CBC-48-46-20	1500	1500	302.586	5.8	471	110	2270	549.00
Chung et al. (2007)	rectangular	R22C20C	500	500	99.88	4.4	407	35.2	189.4	30.60
		R22C30C	500	500	99.88	4.4	407	35.2	284.1	30.60
		R22C40C	500	500	99.88	4.4	407	35.2	378.8	24.70
		R22C50C	500	500	99.88	4.4	407	35.2	473.5	22.50
		R22C60C	500	500	99.88	4.4	407	35.2	568.2	18.40
		R31C20C	500	500	100.152	3.21	449	35.2	172.2	25.50
		R31C30C	500	500	100.152	3.21	449	35.2	258.3	24.80

Ref.	section type	specimen ID	h (mm)	h_c (mm)	D (mm)	t (mm)	σ_y (MPa)	σ_c (MPa)	P (kN)	M_u (kN•m)
		R31C40C	500	500	100.152	3.21	449	35.2	344.4	23.20
		R31C50C	500	500	100.152	3.21	449	35.2	430.5	20.30
		R31C60C	500	500	100.152	3.21	449	35.2	516.6	17.20
		R43C20C	500	500	99.904	2.24	415	35.2	137.4	16.20
		R43C30C	500	500	99.904	2.24	415	35.2	206.1	16.40
		R43C40C	500	500	99.904	2.24	415	35.2	274.8	14.80
		R43C50C	500	500	99.904	2.24	415	35.2	343.5	12.70
		R43C60C	500	500	99.904	2.24	415	35.2	412.2	10.60
Chung (2010)	circular	C21C20	700	700	139.92	6.6	295	36.8	284	54.70
		C21C30	700	700	139.92	6.6	295	36.8	426	56.70
		C21C40	700	700	139.92	6.6	295	36.8	568	54.40
		C31C20	700	700	139.95	4.5	327	36.8	242.4	45.80
		C31C30	700	700	139.95	4.5	327	36.8	363.6	48.50
		C31C40	700	700	139.95	4.5	327	36.8	484.8	47.10
		C44C20	700	700	139.84	3.2	358	36.8	212.2	37.10
		C44C30	700	700	139.84	3.2	358	36.8	318.3	40.50

Ref.	section type	specimen ID	h (mm)	h_c (mm)	D (mm)	t (mm)	σ_y (MPa)	σ_c (MPa)	P (kN)	M_u (kN•m)
		C44C40	700	700	139.84	3.2	358	36.8	424.4	42.20
Goto et al. (2014)	circular	CCFT4.0-1	1833	540	262	3.97	399.9	30.54	193.0	-
		CCFT4.0-2	1833	540	261.9	3.96	399.9	33.68	192.5	-
		CCFTND4.0-2	1833	540	262.8	4.11	399.9	30.08	200.4	-
		CCFT5.5-1	1833	540	264.22	5.49	414.3	28.43	277.3	-
		CCFT5.5-2	1833	540	264.15	5.48	414.3	34.53	276.7	-
Nakai et al. (1995)	rectangular	R-L/4	750	127.5	135.5*105.5	4.5	373.1	34.21	116.9	-
		R-L/3	750	170	135.5*105.6	4.5	373.1	33.9	116.95	-
		R-L/2	750	255	135.5*105.7	4.5	373.1	33.48	117.0	-
Wang et al. (2019)	circular	CFST-1-1-1	525	525	140	2	722.6	43.5	104.68	44.95
		CFST-1-2-2	525	525	140	2	722.6	49.1	221.8	54.55
		CFST-1-3-3	525	525	140	2	722.6	78.6	431	74.71
		CFST-1-4-4	525	525	140	2	722.6	97.6	659.09	79.18
		CFST-2-1-2	525	525	180	2	722.6	43.5	307.24	77.19
		CFST-2-2-1	525	525	180	2	722.6	49.1	164.04	74.89
		CFST-2-3-4	525	525	180	2	722.6	78.6	875.65	121.81

Ref.	section type	specimen ID	h (mm)	h_c (mm)	D (mm)	t (mm)	σ_y (MPa)	σ_c (MPa)	P (kN)	M_u (kN•m)
		CFST-2-4-3	525	525	180	2	722.6	97.6	762.77	112.72
		CFST-3-1-3	525	525	220	2	722.6	43.5	632.75	117.83
		CFST-3-2-4	525	525	220	2	722.6	49.1	906.43	142.66
		CFST-3-3-1	525	525	220	2	722.6	78.6	309.26	111.83
		CFST-3-4-2	525	525	220	2	722.6	97.6	725	145.64
		CFST-4-1-4	525	525	260	2	722.6	43.5	1106.3	185.00
		CFST-4-2-3	525	525	260	2	722.6	49.1	895.84	201.40
		CFST-4-3-2	525	525	260	2	722.6	78.6	829.43	201.57
		CFST-4-4-1	525	525	260	2	722.6	97.6	489.49	169.36
Yuan et al. (2013)	rectangular	S-20	2400	450	450	6	391	23.5	625.0	1081.61
		S-40	2400	900	450	6	391	23.5	625.0	1158.17
Zhang et al. (2007)	rectangular	C4N3	1200	1200	200	1.48	202	32	490	126.48
		C4N4-1	1200	1200	200	1.48	202	32	656	124.20
		C4N4-2	1200	1200	200	1.48	202	32	656	130.80
		C4N5-1	1200	1200	200	1.48	202	32	820	126.72
		C4N5-2	1200	1200	200	1.48	202	32	820	135.24

Ref.	section type	specimen ID	h (mm)	h_c (mm)	D (mm)	t (mm)	σ_y (MPa)	σ_c (MPa)	P (kN)	M_u (kN•m)
		C4N6	1200	1200	200	1.48	202	32	980	133.44
		C2N3	1200	1200	200	1.48	202	32	475	127.80
		C2N4	1200	1200	200	1.48	202	32	630	134.40
		C2N5	1200	1200	200	1.48	202	32	790	137.64
Skalomenos et al. (2016)	circular	C-25C-2	1100	1100	150	6	387	79	559	87.00
		H-OC-2	1100	1100	150	6	788	42.4	0	114.00
		H-25C-2	1100	1100	150	6	788	82.3	831	133.00
	rectangular	C-25R-2	1100	1100	150	6	387	79.3	694	98.00
		C-25R-20	1100	1100	150	6	436	44.3	569	88.00
		H-25R-2	1100	1100	150	6	788	79.3	1025	173.00
		H-25R-20	1100	1100	150	6	788	47.6	886	130.00
Chen et al. (2019)	octagonal	S1	870	870	128.73*120.62	3.01	431.6	30	0	24.61
		S2	870	870	129.10*121.08	3	431.6	32.1	240	20.72
		S3	870	870	128.67*120.73	3	431.6	32.3	400	18.58
		S4	870	870	129.02*121.25	3	431.6	50.5	0	25.27
		S5	870	870	128.87*120.89	3	431.6	50.9	150	24.42

Ref.	section type	specimen ID	h (mm)	h_c (mm)	D (mm)	t (mm)	σ_y (MPa)	σ_c (MPa)	P (kN)	M_u (kN•m)
		S6	870	870	129.01*121.14	3	431.6	51.7	305	20.98
		S7	870	870	129.13*120.96	3	431.6	102.5	0	26.86
		S8	870	870	128.67*120.84	2.99	431.6	104.6	235	24.05
		S9	870	870	128.31*120.57	3	431.6	105.1	400	21.08
Usami and Ge (1994)	rectangular	UU2	854	229	170*111	4.51	235	42.1	115.3	49.26
		UU3	854	381	170*112	4.51	235	42.2	115.7	48.43
		UU4	854	381	170*113	4.51	235	42.5	116.2	50.09
		UU5	1354	365	170*114	4.51	235	40.8	116.6	46.77
		UU7	1354	311	214*145	4.51	235	41	148.4	83.74
		SS8	1671	501	311*192	4.51	235	39.8	209.4	166.48
		SS9	1671	836	311*193	4.51	235	40	209.8	166.96
Zhang et al. (2018)	L-shape	L-CFST1	980	980	200*200*100	3	352.67	36.75	600	0.00
		L-CFST2	980	980	200*200*101	4	360.67	36.75	600	0.00
		L-CFST3	980	980	200*200*102	5	360	36.75	600	0.00
Ge and Usami (1996)	rectangular	UC70-40-3[0]	1354	365	235*156	5.87	308	32.4	274.3	125.74
		UC70-25-3[0]	953	236	235*157	5.87	308	38	275.0	126.40

Ref.	section type	specimen ID	h (mm)	h_c (mm)	D (mm)	t (mm)	σ_y (MPa)	σ_c (MPa)	P (kN)	M_u (kN•m)
		UC70-25-3[3]	952	236	235*157	5.87	308	38.2	275.0	128.12
		UC70-25-5[3]	954	394	235*157	5.87	308	38.7	275.0	132.26
		UC70-25-5[3] ND	952	236	235*156	5.87	308	38.5	274.3	106.54
		UC70-25-5[3] ND (2)	952	394	235*157	5.87	308	39.4	275.0	108.29
		UC90-40-5[3]	1753	789	296*202	5.87	308	33.8	351.7	191.36
		SC45-25-3[0]	952	251	317*196	5.87	308	36.9	362.5	198.79
		SC45-25-3[3]	953	251	318*196	5.87	308	37.1	363.2	202.05
		SC45-25-5[3]	952	419	317*196	5.87	308	37.4	362.5	233.78
		SC60-35-3[3]	1854	501	418*264	5.87	308	35.6	484.7	339.60
		SC60-35-5[3]	1853	836	418*264	5.87	308	36.5	484.78	381.33
Marson and Bruneau (2004)	circular	CFST 51	2200	2200	323.9	5.5	405	35	1600	446.60
		CFST 34	2200	2200	323.9	7.5	415	40	1920	544.72
		CFST 64	2200	2200	406.4	5.5	449	37	1000	426.80
		CFST 42	2200	2200	406.4	9.5	505	35	1920	1006.72
Yuan et al. (2014)	circular	S-25	2250	536	480	6	307	22	548.6	423.74
		S-50	2250	1125	480	6	307	22	548.6	515.69

Ref.	section type	specimen ID	h (mm)	h_c (mm)	D (mm)	t (mm)	σ_y (MPa)	σ_c (MPa)	P (kN)	M_u (kN•m)
Inai et al. (2004)	circular	SC4-A-4-C	1446	1446	241	4.7	284	39.2	1034	173.00
		SC4-A-9-C	1428	1428	238	4.7	284	88.2	1784	202.00
		SC6-A-4-C	1446	1446	241	9	482	35.5	1809	371.00
		SC6-A-9-C	1446	1446	241	9	482	84.4	2567	422.00
		SC6-A-9-V	1446	1446	241	9	482	91.7	4682	274.00
		SC6-C-4-C	1428	1428	238	4.52	504	35.5	1462	220.00
		SC6-C-9-C	1440	1440	240	4.52	504	84.4	2086	254.00
		SC6-C-9-V	1446	1446	241	4.52	504	91.7	3874	153.00
		SC8-A-4-C	966	966	161	9.12	820	35.5	1612	245.00
		SC8-A-9-C	966	966	161	9.12	820	93.9	1988	261.00
		SC8-A-9-V	966	966	161	9.12	820	93.9	3457	173.00
		SC8-C-9-C	960	960	160	4.76	771	93.9	1347	151.00
		SC8-C-9-V	954	954	159	4.76	771	93.9	2359	110.00
	rectangular	SR4-A-4-C	1260	1260	210	5.8	295	39.2	1162	187.00
		SR4-A-9-C	1260	1260	210	5.8	295	88.2	1895	225.00
		SR4-C-4-C	1260	1260	210	4.5	504	39.2	1021	151.00

Ref.	section type	specimen ID	h (mm)	h_c (mm)	D (mm)	t (mm)	σ_y (MPa)	σ_c (MPa)	P (kN)	M_u (kN•m)
		SR4-C-9-C	1254	1254	209	4.5	504	88.2	1791	202.00
		SR6-A-4-C	1266	1266	211	8.83	537	39.3	1959	373.00
		SR6-A-9-C	1266	1266	211	8.83	537	88.3	2649	402.00
		SR6-A-9-V	1260	1260	210	8.83	537	91.7	4880	259.00
		SR6-C-4-C	1266	1266	211	5.95	540	39.3	1545	263.00
		SR6-C-9-C	1260	1260	210	5.95	540	93.7	2368	295.00
		SR6-C-9-V	1272	1272	212	5.95	540	91.7	4326	163.00
		SR8-A-4-C	1068	1068	178	9.45	825	42.3	2576	345.00
		SR8-A-9-C	1074	1074	179	9.45	825	94.5	3077	377.00
		SR8-A-9-V	1068	1068	178	9.45	825	94.5	5294	217.00
		SR8-C-4-C	1080	1080	180	6.66	824	42.3	2003	240.00
		SR8-C-9-C	1080	1080	180	6.66	824	94.5	2540	264.00
		SR8-C-9-V	1080	1080	180	6.66	824	94.5	4437	146.00
		SR6-A-9-C-45	1260	1260	210	8.83	537	88.3	2644	374.00
		SR6-C-9-C-45	1266	1266	211	5.95	540	88.3	2358	270.00
		SR8-A-9-C-45	1086	1086	181	9.45	825	91.7	2965	371.00

Ref.	section type	specimen ID	h (mm)	h_c (mm)	D (mm)	t (mm)	σ_y (MPa)	σ_c (MPa)	P (kN)	M_u (kN•m)
		SR8-A-9-C-22.5	1080	1080	180	9.45	825	84.4	2782	390.00
Ishizawa and Iura (2006)	circular	No.1	1750	298	502	5.76	287	23.4	386	-
		No.2	1750	490	502	5.76	287	24.4	386	-
		No.3	1750	840	502	5.76	287	25.4	386	-
		No.4	1750	998	502	5.94	270	36.3	375	-
		No.5	1750	600	400	5.77	312	22.6	419	-
		No.6	1750	998	500	5.76	313	37.1	335	-
		No.7	1750	600	400	5.73	280	35.4	375	-
Gajalakshmi and Helena (2012)	circular	CFT57-V	850	850	114	2	293	32.44	105.9	-
		CFT57-C2	850	850	114	2	293	32.44	105.9	-
		CFT57-C4	850	850	114	2	292	32.44	105.9	-
		CFT57-C6	850	850	114	2	292	32.44	105.9	-
		CFT38-V	850	850	114	3	293	32.44	182	-
		CFT38-C2	850	850	114	3	293	32.44	182	-
		CFT38-C4	850	850	114	3	293	32.44	182	-
		CFT38-C6	850	850	114	3	293	32.44	182	-

Ref.	section type	specimen ID	h (mm)	h_c (mm)	D (mm)	t (mm)	σ_y (MPa)	σ_c (MPa)	P (kN)	M_u (kN•m)
Wu et al. (2012)	rectangular	S-T2N2M0	1200	1200	300	1.78	255.8	48.2	731	186.84
		S-T2N2M2	1200	1200	300	1.78	255.8	45.55	684	182.52
		S-T2N2M4	1200	1200	300	1.78	255.8	43.96	659	207.48
		S-T2N4M0	1200	1200	300	1.78	255.8	48.2	1433	232.68
		S-T2N4M2	1200	1200	300	1.78	255.8	45.55	1360	225.60
		S-T2N4M4	1200	1200	300	1.78	350	43.96	1317	-!
		S-T3N2M0	1200	1200	300	2.76	350	48.2	840	243.24
		S-T3N2M2	1200	1200	300	2.76	350	45.55	793	248.04
		S-T3N2M4	1200	1200	300	2.76	350	43.96	756	204.48
		S-T3N4M0	1200	1200	300	2.76	350	48.2	1659	314.28
		S-T3N4M2	1200	1200	300	2.76	269.8	45.55	1587	289.44
		S-T3N4M4	1200	1200	300	2.76	269.8	43.96	1543	304.68
		S-T6N4M0	1200	1200	300	5.5	269.8	48.2	1800	393.60
		S-T6N4M2	1200	1200	300	5.5	269.8	45.55	1780	381.48
		S-T6N4M4	1200	1200	300	5.5	269.8	43.96	1745	366.24

Ref.	section type	specimen ID	h (mm)	h_c (mm)	D (mm)	t (mm)	σ_y (MPa)	σ_c (MPa)	P (kN)	M_u （kN•m）
Silva et al. (2016)	circular	CR-RuC15%-219-3-0%-C	1350	1350	219	3	308	20	0	63.05
		CR-RuC15%-219-3-15%-C	1350	1350	219	3	308	20	222	90.05
		CR-RuC15%-219-5-0%-C	1350	1350	219	5	393	20	0	115.02
		CR-RuC15%-219-5-15%-C	1350	1350	219	5	393	20	290	142.16
		CR-RuC5%-219-5-0%-C	1350	1350	219	5	393	39	0	121.10
		CR-RuC5%-219-5-15%-C	1350	1350	219	5	393	39	359	138.65
		CR-StdC-219-5-0%-C	1350	1350	219	5	393	53	0	130.01
		CR-StdC-219-5-15%-C	1350	1350	219	5	393	53	380	148.77
Shen et al. (2016)	L-shape	LRAZ-1	1125	1125	300*150*5	5	325	39.5	820	-
		LRAZ-2	1125	1125	300*150*5	5	325	39.5	2055	-
		LRBZ-1	1125	1125	300*150*6	6	295	39.5	850	-
		LRBZ-2	1125	1125	300*150*6	6	295	39.5	2200	-
		LRCZ-1	1125	1125	300*100*6	6	295	39.5	750	-
		LRCZ-2	1125	1125	300*100*6	6	295	39.5	1920	-

Reference

Al-Bermani, F. G. A., Li, B., Zhu, K., and Kitipornchai, S. (1994). "Cyclic and seismic response of flexibly jointed frames." *Engineering Structures*, 16(4), 249-255.

Association, J. R. (2012). "Specification for road bridges and commentaries, V." *Seismic Design* Tokyo, Japan.

Aval, S. B. B., Saadeghvaziri, M. A., and Golafshani, A. A. (2002). "Comprehensive Composite Inelastic Fiber Element for Cyclic Analysis of Concrete-Filled Steel Tube Columns." *Journal of Engineering Mechanics*, 128(4), 428-437.

Bruneau, M., and Marson, J. (2004). "Seismic Design of Concrete-Filled Circular Steel Bridge Piers." *Journal of Bridge Engineering*, 9(1), 24-34.

Bruneau, M., Wilson, J. C., and Tremblay, R. (1996). "Performance of steel bridges during the 1995 Hyogo-ken Nanbu (Kobe, Japan) earthquake." *Canadian Journal of Civil Engineering*, 23(3), 678-713.

Chen, J., Chan, T.-M., Su, R. K. L., and Castro, J. M. (2019). "Experimental assessment of the cyclic behaviour of concrete-filled steel tubular beam-columns with octagonal sections." *Engineering Structures*, 180, 544-560.

Chen, W. F. (1982). *Plasticity in reinforced concrete*, McGraw-Hill, New York.

Chung, K. (2010). "Prediction of pre- and post-peak behavior of concrete-filled circular steel tube columns under cyclic loads using fiber element method." *Thin-Walled Structures*, 48(2), 169-178.

Chung, K., Chung, J., and Choi, S. (2007). "Prediction of pre- and post-peak behavior of concrete-filled square steel tube columns under cyclic loads using fiber element method." *Thin-Walled Structures*, 45(9), 747-758.

Constantinou, M. C., and Tadjbakhsh, I. G. (1985). "Hysteretic Dampers in Base Isolation: Random Approach." Journal of Structural Engineering, 111(4), 705-721.

Denavit, M. D., and Hajjar, J. F. (2012). "Nonlinear Seismic Analysis of Circular Concrete-Filled Steel Tube Members and Frames." *Journal of Structural Engineering*, 138(9), 1089-1098.

Engineers, J. S. o. C. (2018). "Standard specifications for steel and composite structures-2018." *IV Seismic design,edited by Goto, Y.*

Fam, A., Qie, F. S., and Rizkalla, S. (2004). "Concrete-Filled Steel Tubes Subjected to Axial Compression and Lateral Cyclic Loads." *Journal of Structural Engineering*, 130(4), 631-640.

Fujii, K. (2000). "Ultimate Behavior of Concrete Filled Steel Tubular Columns under Horizontal Cyclic Loads." *Composite Construction in Steel and Concrete IV*, 620-631.

Fujikura, S., and Bruneau, M. (2012). "Dynamic Analysis of Multihazard-Resistant Bridge Piers Having Concrete-Filled Steel Tube under Blast Loading." *Journal of Bridge Engineering*, 17(2), 249-258.

Fujikura, S., Bruneau, M., and Lopez-Garcia, D. (2008). "Experimental Investigation of Multihazard Resistant Bridge Piers Having Concrete-Filled Steel Tube under Blast Loading." *Journal of Bridge Engineering*, 13(6), 586-594.

Gajalakshmi, P., and Helena, H. J. (2012). "Behaviour of concrete-filled steel columns subjected to lateral cyclic loading." *Journal of Constructional Steel Research*, 75, 55-63.

Gayathri, V., Shanmugam, N. E., and Choo, Y. S. (2004). "Concrete-Filled Tubular Columns: Part 1 — Cross-Section Analysis." *International Journal of Structural Stability and Dynamics*, 04(04), 459-478.

Gayathri, V., Shanmugam, N. E., and Choo, Y. S. (2004). "Concrete-Filled Tubular Columns: Part 2 — Column Analysis." *International Journal of Structural Stability and Dynamics*, 04(04), 479-495.

Ge, H., and Usami, T. (1992). "Strength of Concrete-Filled Thin-Walled Steel Box Columns: Experiment." *Journal of Structural Engineering*, 118(11), 3036-3054.

Ge, H., and Usami, T. (1996). "Cyclic Tests of Concrete-Filled Steel Box Columns." *Journal of Structural Engineering*, 122(10), 1169-1177.

Ge, H. B., Susantha, K. A. S., Satake, Y., and Usami, T. (2003). "Seismic demand predictions of concrete-filled steel box columns." *Engineering Structures*, 25(3), 337-345.

Goto, Y. "Seismic design of thin-walled steel and CFT piers, seismic design." *Bridge engineering handbook,2nd* W. F. C. a. L. Duan, ed., CRC/Taylor & Francis Group, Boca Raton, FL, 337–379.

Goto, Y., Ebisawa, T., and Lu, X. (2014). "Local Buckling Restraining Behavior of Thin-Walled Circular CFT Columns under Seismic Loads." *Journal of Structural Engineering*, 140(5).

Goto, Y., Ebisawa, T., Lu, X., and Lu, W. (2015). "Ultimate State of Thin-Walled Circular Steel Columns Subjected to Biaxial Horizontal Forces and Biaxial Bending Moments Caused by Bidirectional Seismic Accelerations." *Journal of Structural Engineering*, 141(4).

Goto, Y., Ebisawa, T., Obata, M., Li, J., and Xu, Y. (2017). "Ultimate Behavior of Steel and CFT Piers in Two-Span Continuous Elevated-Girder Bridge Models Tested by Shake-Table Excitations." *Journal of Bridge Engineering*, 22(5).

Goto, Y., Jiang, K., and Obata, M. (2006). "Stability and Ductility of Thin-Walled Circular Steel Columns under Cyclic Bidirectional Loading." *Journal of Structural Engineering*, 132(10), 1621-1631.

Goto, Y., Kumar, G. P., and Kawanishi, N. (2009). "Fem Analysis for Hysteretic Behavior of Cft Bridge Piers Considering Interaction Between Steel Tube and Infilled Concrete." *Doboku Gakkai Ronbunshuu A*, 65(2), 487-504.

Goto, Y., Kumar, G. P., and Kawanishi, N. (2010). "Nonlinear Finite-Element Analysis for Hysteretic Behavior of Thin-Walled Circular Steel Columns with In-Filled Concrete." *Journal of Structural Engineering*, 136(11), 1413-1422.

Goto, Y., Mizuno, K., and Prosenjit Kumar, G. (2012). "Nonlinear Finite Element Analysis for Cyclic Behavior of Thin-Walled Stiffened Rectangular Steel Columns with In-Filled Concrete." *Journal of Structural Engineering*, 138(5), 571-584.

Goto, Y., Muraki, M., and Obata, M. (2009). "Ultimate State of Thin-Walled Circular Steel Columns under Bidirectional Seismic Accelerations." *Journal of Structural Engineering*, 135(12), 1481-1490.

Goto, Y., Wang, Q., and Obata, M. (1998). "FEM Analysis for Hysteretic Behavior of Thin-Walled Columns." *Journal of Structural Engineering*, 124(11), 1290-1301.

Han, L.-H., Li, W., and Bjorhovde, R. (2014). "Developments and advanced applications of concrete-filled steel tubular (CFST) structures: Members." *Journal of Constructional Steel Research*, 100, 211-228.

Han, L.-H., Xu, C.-Y., and Tao, Z. (2019). "Performance of concrete filled stainless steel tubular (CFSST) columns and joints: Summary of recent research." *Journal of Constructional Steel Research*, 152, 117-131.

Han, L. H., Yang, Y. F., and Tao, Z. (2003). "Concrete-filled thin-walled steel SHS and RHS beam-columns subjected to cyclic loading." *Thin-Walled Structures*, 41(9), 801-833.

Hatzigeorgiou, G. D. (2008). "Numerical model for the behavior and capacity of circular CFT columns, Part I: Theory." *Engineering Structures*, 30(6), 1573-1578.

Hatzigeorgiou, G. D. (2008). "Numerical model for the behavior and capacity of circular CFT columns, Part II: Verification and extension." *Engineering Structures*, 30(6), 1579-1589.

Hu, J. W., Park, J., and Leon, R. T. (2010). "Advanced Analysis and Performance Based Evaluation of Concrte Filled Tube (Cft) Columns." *Advanced Steel Construction*, 1019-1033.

Huang, Z. (2018). "Experimental study on the seismic performance of concrete filled steel tubular laced columns." *Steel and Composite Structures*.

Huxley, R. (1984). *The rise and fall of the Severn Bridge Railway: 1872–1970*, Alan Sutton & Gloucester County Library.

Inai, E., Mukai, A., Kai, M., Tokinoya, H., Fukumoto, T., and Mori, K. (2004). "Behavior of Concrete-Filled Steel Tube Beam Columns." *Journal of Structural Engineering*, 130(2), 189-202.

Kitada, T. (1998). "Ultimate strength and ductility of state-of-the-art concrete-filled steel bridge piers in Japan." *Engineering Structures*, 20(4-6), 347-354.

Kostic, S. M., and Filippou, F. C. (2012). "Section Discretization of Fiber Beam-Column Elements for Cyclic Inelastic Response." *Journal of Structural Engineering*, 138(5), 592-601.

Kulkarni, N. G., Kasai, A., and Tsuboi, H. (2009). "Displacement based seismic verification method for thin-walled circular steel columns subjected to bi-directional cyclic loading." *Engineering Structures*, 31(11), 2779-2786.

Lee, J., and Fenves, G. L. (1998). "Plastic-Damage Model for Cyclic Loading of Concrete Structures." *Journal of Engineering Mechanics*, 124(8), 892-900.

Lee, K. C., and Yoo, C. H. (2012). "Longitudinal Stiffeners in Concrete-Filled Tubes." *Journal of Structural Engineering*, 138(6), 753-758.

Lehman, D. E., Kuder, K. G., Gunnarrson, A. K., Roeder, C. W., and Berman, J. W. (2015). "Circular Concrete-Filled Tubes for Improved Sustainability and Seismic Resilience." *Journal of Structural Engineering*, 141(3).

Lehman, D. E., and Roeder, C. W. (2012). "An Initial Study into the use of Concrete Filled Steel Tubes for Bridge Piers and Foundation Connections." *Final Report No. CA12-1972*, Department of Civil Engineer, University of Washington, Seattle, WA 98195.

Li, X., Zhou, T., Li, J., Kuang, X.-B., and Zhao, Y.-W. (2019). "Seismic behavior of encased CFT column base connections." *Engineering Structures*, 182, 363-378.

Liu, J., Zhou, X., and Zhang, S. (2008). "Seismic behaviour of square CFT beam–columns under biaxial bending moment." *Journal of Constructional Steel Research*, 64(12), 1473-1482.

Liang, Q. Q., and Fragomeni, S. (2009). "Nonlinear analysis of circular concrete-filled steel tubular short columns under axial loading." *Journal of Constructional Steel Research*, 65(12), 2186-2196.

Mander, J. B., Priestley, M. J. N., and Park, R. (1988). "Theoretical Stress-Strain Model for Confined Concrete." *Journal of Structural Engineering*, 114(8), 1804-1826.

Mark D. Denavit, J. F. H., Roberto T. Leon and Tiziano Perea (2015). "Advanced Analysis and Seismic Design of Concrete-Filled Steel Tube Structures." *Structures Congress 2015*, 972-983.

Marson, J., and Bruneau, M. (2004). "Cyclic Testing of Concrete-Filled Circular Steel Bridge Piers having Encased Fixed-Based Detail." *Journal of Bridge Engineering*, 9(1), 14-23.

Menengotto, M. (1973). "Method of Analysis for Cyclically Loaded Reinforced Concrete Plane Frames Including Changes in Geometry and Nonelastic Behavior of Elements under Combined Normal Force and Bending." *IABSE Symposium on Resistance and Ultimate Deformability of Structures Acted on by Well-Defined Repeated Loads, Lisbon, 1973*.

Nakahara, H., Ninakawa, T., and Sakino, K. (2003). "Cyclic Bending Behavior of Concrete Filled Steel Tubular Columns under Constant Gravity Load." *Journal of Structural and Construction Engineering (Transactions of AIJ)*, 68(568), 139-146.

Nakai, H., Kitada, T., and Nakanishi, K. (1995). "Experimental Study on Ultimate Strength and Ductility of Steel and Composite Bridge Piers Under Gradually Increasing and Cyclic Load." *Doboku Gakkai Ronbunshu*(513), 89-100.

Nakai, H., Kitada, T., Yoshikawa, O., Murakami, S., and Sakuramoto, Y. (1999). "Experimental Study of Concrete-filled Steel Members with Circular Cross Section Subjected to Bending and Torsion." *Doboku Gakkai Ronbunshu*(612), 85-97.

Nakanishi, K., Kitada, T., and Nakai, H. (1999). "Experimental study on ultimate strength and ductility of concrete filled steel columns under strong earthquake." *Journal of Constructional Steel Research*, 51(3), 297-319.

Obata, M., and Goto, Y. (2007). "Development of Multidirectional Structural Testing System Applicable to Pseudodynamic Test." *Journal of Structural Engineering*, 133(5), 638-645.

OpenSees. (2006). Open system for earthquake engineering simulation (OpenSees), Berkeley, CA, Pacific Earthquake Engineering Research (PEER) Center.

Ou, Z. J. (2013). "The Practice of Concrete Filled Steel Tube Piers to Bridges: A Review." *Applied Mechanics and Materials*, 405-408, 1602-1605.

Patel, V. I., Liang, Q. Q., and Hadi, M. N. S. (2014). "Numerical analysis of high-strength concrete-filled steel tubular slender beam-columns under cyclic loading." *Journal of Constructional Steel Research*, 92, 183-194.

Qiang, Z., Yaozhuang, L., and Kolozvari, K. (2018). "Numerical modeling of steel–concrete composite structures." *Structural Concrete*, 19(6), 1727-1739.

Ramberg, W., and Osgood, W. R. (1943). "Description of stress-strain curves by three parameters." National Advisory Committee for Aeronautics, Washington, D. C.

Roeder, C. W., Lehman, D. E., and Bishop, E. (2010). "Strength and Stiffness of Circular Concrete-Filled Tubes." *Journal of Structural Engineering*, 136(12), 1545-1553.

Roeder, C. W., Stephens, M. T., and Lehman, D. E. (2018). "Concrete Filled Steel Tubes for Bridge Pier and Foundation Construction." *International Journal of Steel Structures*, 18(1), 39-49.

Samarakkody, D. I., Thambiratnam, D. P., Chan, T. H. T., and Moragaspitiya, P. H. N. (2017). "Differential axial shortening and its effects in high rise buildings with composite concrete filled tube columns." *Construction and Building Materials*, 143, 659-672.

Serras, D. N., Skalomenos, K. A., Hatzigeorgiou, G. D., and Beskos, D. E. (2016). "Modeling of circular concrete-filled steel tubes subjected to cyclic lateral loading." *Structures*, 8, 75-93.

Serras, D. N., Skalomenos, K. A., Hatzigeorgiou, G. D., and Beskos, D. E. (2017). "Inelastic behavior of circular concrete-filled steel tubes: monotonic versus cyclic response." *Bulletin of Earthquake Engineering*, 15(12), 5413-5434.

Shams, M., and Saadeghvaziri, M. A. (1999). "Nonlinear Response of Concrete-Filled Steel Tubular Columns under Axial Loading." *ACI Structural Journal*, 96(6).

Shen, Z.-Y., Lei, M., Li, Y.-Q., Lin, Z.-Y., and Luo, J.-H. (2016). "Experimental Study on Seismic Behavior of Concrete-Filled L-Shaped Steel Tube Columns." *Advances in Structural Engineering*, 16(7), 1235-1247.

Shen, C., Tanaka, Y., Mizuno, E., and Usami, T. (1992). "A Two-Surface Model for Steels with Yield Plateau." *Doboku Gakkai Ronbunshu(441)*, 11-20.

Silva, A., Jiang, Y., Castro, J. M., Silvestre, N., and Monteiro, R. (2016). "Experimental assessment of the flexural behaviour of circular rubberized concrete-filled steel tubes." *Journal of Constructional Steel Research*, 122, 557-570.

Simulia (2014). *ABAQUS/Standard User's Manual*, Dassault Systémes, Providence, USA.

Skalomenos, K. A., Hatzigeorgiou, G. D., and Beskos, D. E. (2014). "Parameter identification of three hysteretic models for the simulation of the response of CFT columns to cyclic loading." *Engineering Structures*, 61, 44-60.

Skalomenos, K. A., Hayashi, K., Nishi, R., Inamasu, H., and Nakashima, M. (2016). "Experimental Behavior of Concrete-Filled Steel Tube Columns Using Ultrahigh-Strength Steel." *Journal of Structural Engineering*, 142(9).

Stephens, M. T., Berg, L. M., Lehman, D. E., and Roeder, C. W. (2016a). "Seismic CFST Column-to-Precast Cap Beam Connections for Accelerated Bridge Construction." *Journal of Structural Engineering*, 142(9).

Stephens, M. T., Lehman, D. E., and Roeder, C. W. (2016b). "Design of CFST column-to-foundation/cap beam connections for moderate and high seismic regions." *Engineering Structures*, 122, 323-337.

Stephens, M. T., Lehman, D. E., and Roeder, C. W. (2018). "Seismic performance modeling of concrete-filled steel tube bridges: Tools and case study." *Engineering Structures*, 165, 88-105.

Susantha, K. A. S., Ge, H., and Usami, T. (2001). "Uniaxial stress–strain relationship of concrete confined by various shaped steel tubes." *Engineering Structures*, 23(10), 1331-1347.

Susantha, K. A. S., Ge, H., and Usami, T. (2002). "Cyclic analysis and capacity prediction of concrete-filled steel box columns." *Earthquake Engineering & Structural Dynamics*, 31(2), 195-216.

T, I., and M, I. (2006). "Analysis of Partially Concrete-Filled Steel Tubular Columns subjected to Cyclic

Loadings." *Computer Modeling in Engineering & Sciences*, 11(3), 121-130.

Tomii, M., and Sakino, K. (1979). "Elasto-Plastic Behavior of Concrete Filled Square Steel Tubular Beam-Columns." *Transactions of the Architectural Institute of Japan*, 280(0), 111-122.

Tort, C., and Hajjar, J. F. (2010). "Mixed Finite-Element Modeling of Rectangular Concrete-Filled Steel Tube Members and Frames under Static and Dynamic Loads." *Journal of Structural Engineering*, 136(6), 654-664.

Tort, C., and Hajjar, J. F. (2010). "Mixed Finite Element for Three-Dimensional Nonlinear Dynamic Analysis of Rectangular Concrete-Filled Steel Tube Beam-Columns." *Journal of Engineering Mechanics*, 136(11), 1329-1339.

Usami, T., and Ge, H. (1994). "Ductility of Concrete-Filled Steel Box Columns under Cyclic Loading." *Journal of Structural Engineering*, 120(7), 2021-2040.

Usami, T., and Ge, H. B. (1998). "Cyclic behavior of thin-walled steel structures—numerical analysis." *Thin-Walled Structures*, 32(1-3), 41-80.

Usami, T., Ge, H. B., and Saizuka, K. (1997). "Behaviour of partially concrete-filled steel bridge piers under cyclic and dynamic loading." *Journal of Constructional Steel Research*, 41(2-3), 121-136.

Valipour, H. R., and Foster, S. J. (2010). "Nonlinear static and cyclic analysis of concrete-filled steel columns." *Journal of Constructional Steel Research*, 66(6), 793-802.

Varma, A., Sause, R., M Ricles, J., and Li, Q. (2005). "Development and validation of fiber model for high-strength square concrete-filled steel tube beam-columns." *ACI structural journal*, 102.

Varma, A. H., Ricles, J. M., Sause, R., and Lu, L.-W. (2002). "Seismic behavior and modeling of high-strength composite concrete-filled steel tube (CFT) beam–columns." *Journal of Constructional Steel Research*, 58(5-8), 725-758.

Varma, A. H., Ricles, J. M., Sause, R., and Lu, L.-W. (2004). "Seismic Behavior and Design of High-Strength Square Concrete-Filled Steel Tube Beam Columns." *Journal of Structural Engineering*, 130(2), 169-179.

Wang, J., Sun, Q., Wu, X., and Wu, Y. (2019). "Experimental and analytical investigation on seismic behavior of Q690 circular high-strength concrete-filled thin-walled steel tubular columns." *The Structural Design of Tall and Special Buildings*.

Wang, Y.-h., Nie, J.-g., and Fan, J.-s. (2014). "Fiber beam-column element for circular concrete filled steel tube under axial–flexure–torsion combined load." *Journal of Constructional Steel Research*, 95, 10-21.

Watanabe, E., Sugiura, K., and Oyawa, W. O. (2000). "Effects of multi-directional displacement paths on the cyclic behaviour of rectangular hollow steel columns." *Doboku Gakkai Ronbunshu*(647), 79-95.

Wu, B., Zhao, X.-Y., and Zhang, J.-S. (2012). "Cyclic behavior of thin-walled square steel tubular columns filled with demolished concrete lumps and fresh concrete." *Journal of Constructional Steel Research*, 77, 69-81.

Yadav, R., Chen, B., Yuan, H., and Lian, Z. (2017). "Analytical Behavior of CFST Bridge Piers under Cyclic Loading." *Procedia Engineering*, 173, 1731-1738.

Yamada, S., Akiyama, H., and Kuwamura, H. (1993). "Post-Buckling and Deteriorating Behavior of Box-Section Steel Members." *Journal of Structural and Construction Engineering (Transactions of AIJ)*, 444(0), 135-143.

Yamamoto, T., Kawaguchi, J., and Morino, S. (2002). "Experimental Study of the Size Effect on the Behavior of Concrete Filled Circular Steel Tube Columns under

Axial Compression." *Journal of Structural and Construction Engineering (Transactions of AIJ)*, 67(561), 237-244.

Yang, Y.-F., Hou, C., and Liu, M. (2018). "Experimental Study and Numerical Analysis of CFSST Columns Subjected to Lateral Cyclic Loading." *Journal of Structural Engineering*, 144(12).

Yasui, N. (2001). "Elasto-Plastic Analysis for Local Buckling Behavior of Circular Tubes under Axially Cyclic Loading." *Journal of Structural and Construction Engineering (Transactions of AIJ)*, 66(543), 161-168.

Yuan, H., Dang, J., and Aoki, T. (2013). "Experimental study of the seismic behavior of partially concrete-filled steel bridge piers under bidirectional dynamic loading." *Earthquake Engineering & Structural Dynamics*, 42(15), 2197-2216.

Yuan, H., Dang, J., and Aoki, T. (2014). "Behavior of partially concrete-filled steel tube bridge piers under bi-directional seismic excitations." *Journal of Constructional Steel Research*, 93, 44-54.

Zenzai, S., Shimizu, S., and Chikahiro, Y. (2018). "Behavior of a concrete filled steel box column with considering detachment under seismic load." *Thin-Walled Structures*, 124, 98-106.

Zubydan, A. H., and ElSabbagh, A. I. (2011). "Monotonic and cyclic behavior of concrete-filled steel-tube beam-columns considering local buckling effect." *Thin-Walled Structures*, 49(4), 465-481.

Zhang, Y., Xu, C., and Lu, X. (2007). "Experimental study of hysteretic behaviour for concrete-filled square thin-walled steel tubular columns." *Journal of Constructional Steel Research*, 63(3), 317-325.

Zhang, J., Li, Y., Du, G., and Song, G. (2018). "Damage Detection of L-Shaped Concrete Filled Steel Tube (L-CFST) Columns under Cyclic Loading Using Embedded Piezoceramic Transducers." *Sensors (Basel)*, 18(7).

Acknowledgement

This thesis presented an analytical method of large structural system with CFT columns to improve the computational efficiency of current finite shell-solid element model. This work is based on a series of comprehensive researches on CFT columns carried out by the Nagoya Institute of Technology under the leadership of Prof. Goto Yoshiaki. The experimental studies and the advanced analytical model of Prof. Goto Yoshiaki laid the foundation of the analytical method.

I wish to thank Prof. Goto Yoshiaki for his careful guidance in the past four years. His rigorous academic attitude will last and benefits me a lot on my future academic career. I want to thank Prof. Makoto Obata for his patient help on my life and study. His kindness eased my nervousness in a foreign country. I would like to thank Prof. Kawanishi Naoki for his fruitful discussions and supports on this study. His insights inspired me a lot. My special thanks to Assoc. Prof. Ebisawa Takesama and other student members from Structural Laboratory for their help and instructions in Japan and Shanghai, that got me involved into the research life.

I also express my sincere gratitude to the member of thesis examining committee, Prof. Makoto Obata, Prof. Toshikatsu Ichinose, Prof. Maeda Kenichi and Prof. Nonaka Tetsuya for their valuable comments and suggestions on the revision of this thesis.

In particular, I would like to thank the Chinese Scholarship Council and Japanese Ministry of Education, Science and Culture for the financial support through the Monbukagakusho scholarship.

Finally, I want to express my thanks to my beloved parents and wife. Without your mental support and encouragement, I can never grow into a doctor.